RAFAEL MAGALHÃES COELHO

Implementation and Validation of the Thickened Flame Model Framework for Large Eddy Simulation of Reactive Flows

Implementação e Validação da Estrutura do Modelo de Chama Espessada para Simulação de Grandes Estruturas de Escoamentos Reativos

UNIVERSIDADE FEDERAL DE UBERLÂNDIA
FACULDADE DE ENGENHARIA MECÂNICA
2026

RAFAEL MAGALHÃES COELHO

Implementation and Validation of the Thickened Flame Model Framework for Large Eddy Simulation of Reactive Flows

Implementação e Validação da Estrutura do Modelo de Chama Espessada para Simulação de Grandes Estruturas de Escoamentos Reativos

Dissertação apresentada ao Programa de Pós-Graduação em Engenharia Mecânica da Universidade Federal de Uberlândia, como parte dos requisitos para a obtenção do título de **Mestre em Engenharia Mecânica**.

Área de concentração: Transferência de Calor e Mecânica dos Fluidos.

Orientador: Prof. Dr. João Marcelo Vedovotto

UBERLÂNDIA - MG
2026

Ficha Catalográfica Online do Sistema de Bibliotecas da UFU
com dados informados pelo(a) próprio(a) autor(a).

C672 Coelho, Rafael Magalhães, 2001-
2026 Implementation and Validation of the Thickened Flame Model Framework for Large Eddy Simulation of Reactive Flows [recurso eletrônico] / Rafael Magalhães Coelho. - 2026.

Orientador: João Marcelo Vedovotto.
Dissertação (Mestrado) - Universidade Federal de Uberlândia, Pós-graduação em Engenharia Mecânica.
Modo de acesso: Internet.
DOI http://doi.org/10.14393/ufu.di.2026.178
Inclui bibliografia.

1. Engenharia mecânica. I. Vedovotto, João Marcelo,1981-, (Orient.). II. Universidade Federal de Uberlândia. Pós-graduação em Engenharia Mecânica. III. Título.

CDU: 621

Bibliotecários responsáveis pela estrutura de acordo com o AACR2:
Gizele Cristine Nunes do Couto - CRB6/2091
Nelson Marcos Ferreira - CRB6/3074

UNIVERSIDADE FEDERAL DE UBERLÂNDIA
Coordenação do Programa de Pós-Graduação em Engenharia Mecânica
Av. João Naves de Ávila, nº 2121, Bloco 1M, Sala 212 - Bairro Santa Mônica, Uberlândia-MG, CEP 38400-902
Telefone: (34) 3239-4282 - www.posmecanicaufu.com.br - secposmec@mecanica.ufu.br

ATA DE DEFESA - PÓS-GRADUAÇÃO

ATA DE DEFESA - PÓS-GRADUAÇÃO

Programa de Pós-Graduação em:	Engenharia Mecânica				
Defesa de:	Dissertação de Mestrado Acadêmico, nº 672, PPGEM				
Data:	23/02/2026	Hora de início:	09:00	Hora de encerramento:	11h30
Matrícula:	12422EMC014				
Nome do Discente:	Rafael Magalhães Coelho				
Título do Trabalho:	Implementation and Validation of the Thickened Flame Model Framework for Large Eddy Simulation of Reactive Flows				
Área de concentração:	Transferência de Calor e Mecânica dos Fluidos				
Linha de pesquisa:	Dinâmica dos Fluidos e Transferência de Calor				
Projeto de Pesquisa de vinculação:	Modelagem matemática e computacional de processos de corrosão e erosão em superfícies metálicas em tubulações das Unidades de Refino – MFLAB-PETROBRAS				

Reuniu-se por videoconferência a Banca Examinadora, designada pelo Colegiado do Programa de Pós-graduação em Engenharia Mecânica, assim composta: Prof. Dr. José dos Reis Vieira de Moura Junior - UFU; Prof. Dr. Andrés Armando Mendiburu Zevallos - UFRGS; Dra. Millena Martins Villar Vale - UFU (convidada) e Prof. Dr. João Marcelo Vedovotto - UFU; orientador do candidato.

Iniciando os trabalhos, o presidente da mesa, Prof. Dr. João Marcelo Vedovotto, apresentou a Comissão Examinadora e o candidato, agradeceu a presença do público, e concedeu ao Discente a palavra para a exposição do seu trabalho. A duração da apresentação do Discente e o tempo de arguição e resposta foram conforme as normas do Programa.

A seguir, o senhor presidente concedeu a palavra, pela ordem sucessivamente, aos examinadores, que passaram a arguir o candidato. Ultimada a arguição, que se desenvolveu dentro dos termos regimentais, a Banca, em sessão secreta, atribuiu o resultado final, considerando o candidato:

Aprovado.

Esta defesa faz parte dos requisitos necessários à obtenção do título de Mestre.

O competente diploma será expedido após cumprimento dos demais requisitos, conforme as normas do Programa, a legislação pertinente e a regulamentação

interna da UFU.

Nada mais havendo a tratar, foram encerrados os trabalhos. Foi lavrada a presente ata que após lida e achada conforme foi assinada pela Banca Examinadora.

Documento assinado eletronicamente por **João Marcelo Vedovotto**, **Professor(a) do Magistério Superior**, em 23/02/2026, às 11:33, conforme horário oficial de Brasília, com fundamento no art. 6º, § 1º, do Decreto nº 8.539, de 8 de outubro de 2015.

Documento assinado eletronicamente por **Millena Martins Villar Vale**, **Usuário Externo**, em 23/02/2026, às 11:33, conforme horário oficial de Brasília, com fundamento no art. 6º, § 1º, do Decreto nº 8.539, de 8 de outubro de 2015.

Documento assinado eletronicamente por **José dos Reis Vieira de Moura Júnior**, **Professor(a) do Magistério Superior**, em 23/02/2026, às 11:35, conforme horário oficial de Brasília, com fundamento no art. 6º, § 1º, do Decreto nº 8.539, de 8 de outubro de 2015.

Documento assinado eletronicamente por **Andrés Armando Mendiburu Zevallos**, **Usuário Externo**, em 24/02/2026, às 07:39, conforme horário oficial de Brasília, com fundamento no art. 6º, § 1º, do Decreto nº 8.539, de 8 de outubro de 2015.

A autenticidade deste documento pode ser conferida no site https://www.sei.ufu.br/sei/controlador_externo.php?acao=documento_conferir&id_orgao_acesso_externo=0, informando o código verificador **6829846** e o código CRC **32E0C299**.

Referência: Processo nº 23117.079033/2025-37 SEI nº 6829846

"Não desanimais, animais."
(Silvio Coelho)

ACKNOWLEDGMENTS

First and foremost, I thank God for the health and strength to carry out this research.

To my family, for working tirelessly so that I could devote myself to my studies, for their example of effort and honesty, and for their unconditional support and love. In particular, to Maria de Fátima and Maria Conceição, my beloved grandmothers, and to the dearly missed Silvio Coelho and Francisco Oliveira, whose memory continues to guide me.

To my friends, for always believing in me, even when I doubted myself. A special thanks to Gabriel and Muriel for welcoming me and providing a home in Uberlândia.

To Professor João Marcelo Vedovotto, for the opportunity to grow, for his guidance and encouragement in the most varied aspects, and for his patience.

To Professors Aristeu Silveira Neto and Francisco de Souza, for welcoming me into MFLab and providing essential foundations for my academic formation.

To Johnnatas and Millena, for their support and ever-available "help desk" that guided me through the intricacies of MFSim.

To the irreducible hearts and transposed minds with whom I share my daily life at MFLab.

To the members of the examination committee, for sharing their time and knowledge in helping me through this important milestone, and for their contributions to the quality of this research.

To Petróleo Brasileiro S.A. (Petrobras) for proposing the challenge that inspired this research and providing the funding necessary to carry it out.

To FAPEMIG, CAPES, and CNPq, as well as to the Pos Graduation Program in Mechanical Engineering at the Federal University of Uberlândia (UFU), for their financial and infrastructural support.

ABSTRACT

This work presents the implementation, verification, and validation of the Thickened Flame Model (TFM) framework within the in-house MFSim computational platform for Large Eddy Simulation (LES) of turbulent premixed reactive flows. The TFM addresses the fundamental flame resolution problem in LES—where the laminar flame thickness is far smaller than affordable grid spacing—by artificially thickening the flame through simultaneous enhancement of molecular diffusivities by a factor F and reduction of reaction rates by the same factor, thereby preserving the laminar flame speed while rendering the flame structure resolvable on practical meshes. The implementation, developed in Fortran 90/95 consistent with the MFSim codebase, encompasses the core TFM formulation including the dynamic thickening transformation, the Wang-modified Charlette efficiency function with power-law exponent $\beta = 0.5$ to compensate for lost subgrid flame wrinkling, and two flame sensor options: the Durand and Polifke parabolic sensor based on progress variable and a modified Han sensor based on fuel reaction rate. The module integrates with MFSim's existing infrastructure for implicit-explicit time integration, Strang operator splitting for chemistry via the Cantera library, the dynamic Smagorinsky subgrid-scale model, and block-structured adaptive mesh refinement (AMR). Validation is conducted on the turbulent Bunsen Flame F3 from the experimental campaign of Chen et al., a well-documented configuration operating in the flamelet regime at $\mathrm{Re}_D \approx 24{,}000$ with stoichiometric methane-air, using the Yang and Pope 16-species mechanism. Two mesh configurations are investigated: a production mesh ($\Delta x = 0.34$ mm, $F_{\max} = 6.5$, $\delta_L^F \approx 2.7$ mm) and a coarse mesh ($\Delta x = 0.68$ mm, $F_{\max} = 13.0$, $\delta_L^F \approx 5.5$ mm), both on a two-dimensional domain. The production mesh reproduces mean velocity, temperature, and major species profiles with reasonable agreement against experimental data, confirming that the E/F scaling of source terms preserves the integral effect of heat release on flow acceleration. The coarse mesh, where the thickened flame thickness exceeds the integral turbulent length scale ($\delta_L^F > l_0$), exhibits degraded predictions characterised by broader species distributions, incomplete combustion, and non-physical kinetic energy accumulation, establishing the practical criterion $\delta_L^F < l_0$ as essential for maintaining physically meaningful turbulence-flame coupling. The dominant source of discrepancy with respect to experimental measurements is attributed to the two-dimensional domain assumption, which suppresses three-dimensional turbulent transport mechanisms. The TFM introduces negligible computational overhead (less than 5% of wall-clock time), with its primary benefit residing in the enabling of significantly coarser grids compared to direct flame resolution. This work contributes to the systematic development of reactive flow simulation capabilities in MFSim, complementing existing LES/PDF, AMR with detailed chemistry, virtual kinetic mechanism, and compressible reactive flow methodologies.

Keywords: Thickened Flame Model, Large Eddy Simulation, turbulent premixed combustion, MFSim, Bunsen flame, efficiency function, dynamic thickening.

RESUMO

Este trabalho apresenta a implementação, verificação e validação da estrutura do Modelo de Chama Espessada (*Thickened Flame Model* – TFM) na plataforma computacional MFSim para Simulação de Grandes Estruturas (LES) de escoamentos reativos turbulentos pré-misturados. O TFM aborda o problema fundamental de resolução da chama em LES por meio do espessamento artificial da chama, aumentando simultaneamente as difusividades moleculares por um fator F e reduzindo as taxas de reação pelo mesmo fator, preservando assim a velocidade de chama laminar e tornando a estrutura da chama resolvível em malhas práticas. A implementação, desenvolvida em Fortran 90/95 de forma consistente com a base de código do MFSim, abrange a formulação completa do TFM, incluindo a transformação de espessamento dinâmico, a função de eficiência de Charlette modificada por Wang com expoente da lei de potência $\beta = 0{,}5$ para compensar o enrugamento sub-malha perdido, e duas opções de sensor de chama: o sensor parabólico de Durand e Polifke baseado na variável de progresso e um sensor modificado de Han baseado na taxa de reação do combustível. O módulo integra-se à infraestrutura existente do MFSim para integração temporal implícita-explícita, separação de operadores de Strang para a química via biblioteca Cantera, o modelo de submalha dinâmico de Smagorinsky e o refinamento adaptativo de malha (AMR) bloco-estruturado. A validação é conduzida na chama Bunsen turbulenta F3 da campanha experimental de Chen et al., uma configuração bem documentada operando no regime de *flamelet* com $\mathrm{Re}_D \approx 24.000$ e mistura estequiométrica de metano-ar, utilizando o mecanismo de 16 espécies de Yang e Pope. Duas configurações de malha são investigadas: uma malha de produção ($\Delta x = 0{,}34$ mm, $F_{\max} = 6{,}5$, $\delta_L^F \approx 2{,}7$ mm) e uma malha grosseira ($\Delta x = 0{,}68$ mm, $F_{\max} = 13{,}0$, $\delta_L^F \approx 5{,}5$ mm), ambas em domínio bidimensional. A malha de produção reproduz os perfis médios de velocidade, temperatura e espécies majoritárias com concordância razoável em relação aos dados experimentais, confirmando que o escalonamento E/F dos termos fonte preserva o efeito integral da liberação de calor sobre a aceleração do escoamento. A malha grosseira, na qual a espessura da chama espessada excede a escala integral de turbulência ($\delta_L^F > l_0$), apresenta previsões degradadas, caracterizadas por perfis subestimados das espécies principais, combustão incompleta e acúmulo não físico de energia cinética, estabelecendo o critério prático $\delta_L^F < l_0$ como essencial para manter um acoplamento fisicamente significativo entre turbulência e chama. A principal fonte de discrepância em relação às medições experimentais é atribuída ao domínio bidimensional, que suprime os mecanismos de transporte turbulento tridimensional. O TFM introduz sobrecarga computacional desprezível (inferior a 5% do tempo de execução), sendo seu principal benefício a viabilização de malhas significativamente mais grosseiras em comparação com a resolução direta da chama. Este trabalho contribui para o desenvolvimento sistemático das capacidades de simulação de escoamentos reativos no MFSim, complementando as metodologias existentes de LES/PDF híbrido, AMR com química detalhada, mecanismos cinéticos virtuais e escoamentos reativos compressíveis.

Palavras-chave: Modelo de Chama Espessada, Simulação de Grandes Estruturas, combustão turbulenta pré-misturada, MFSim, chama Bunsen, função de eficiência, espessamento dinâmico.

List of Figures

List of Tables

List of Symbols

Table 1: Latin symbols.

Symbol	Description
A	Pre-exponential factor in Arrhenius rate expression.
a	Strain rate.
c	Progress variable, defined as $c = (T - T_u)/(T_b - T_u)$.
c_p	Specific heat capacity at constant pressure [J/(kg·K)].
c_{ms}	Model constant in Colin efficiency function ($c_{ms} = 0.28$).
C_s	Smagorinsky constant.
D	Mass diffusivity [m^2/s].
D_k	Mass diffusivity of species k into the mixture [m^2/s].
D_{th}	Thermal diffusivity [m^2/s].
Da	Damköhler number, ratio of turbulent to chemical time scales.
E	Efficiency function, compensates for lost subgrid flame wrinkling.
E_a	Activation energy [J/mol].
F	Thickening factor.
$F_{\max}$	Maximum thickening factor.
G	Level-set function for G-equation flame tracking.
GFI	Generalised flame index (Takeno index).
g_i	Gravitational acceleration component [m/s^2].
h_k	Specific enthalpy of species k [J/kg].
$\mathbf{J}$	Chemical Jacobian matrix.
$J_{k,j}$	Diffusive flux of species k in direction j [kg/(m^2·s)].
k	Reaction rate constant [units vary with reaction order].
k_f	Forward reaction rate constant.
k_b	Backward reaction rate constant.
k_{sgs}	Subgrid-scale turbulent kinetic energy [m^2/s^2].
Ka	Karlovitz number, ratio of chemical to Kolmogorov time scales.
K_c	Equilibrium constant in concentration units.
l_G	Gibson length scale [m].
l_t	Integral turbulent length scale [m].
L_{ij}	Resolved turbulent stress tensor (Germano identity) [Pa].
Le	Lewis number, ratio of thermal to mass diffusivity.
M	Subgrid kinetic energy fraction (LES quality indicator).
M_{ij}	Tensor in dynamic Smagorinsky procedure.

Continued on next page

Table 1 – *Continued from previous page*

Symbol	Description
n	Temperature exponent in modified Arrhenius expression.
n_c	Number of grid points across the thickened flame.
N_r	Total number of reactions in the chemical mechanism.
N_s	Total number of species in the mixture.
p	Thermodynamic pressure [Pa].
Pr_t	Turbulent Prandtl number.
Q	Heat of reaction per unit mass of fuel [J/kg].
$\dot{Q}$	Volumetric heat release rate [W/m^3].
$\mathcal{Q}_r$	Rate of progress of reaction r [mol/(m^3·s)].
R_u	Universal gas constant, $R_u = 8.314$ J/(mol·K).
Re_t	Turbulent Reynolds number, $\mathrm{Re}_t = u' l_t / \nu$.
s_c	Consumption-based flame speed [m/s].
S_L	Laminar flame speed [m/s].
S_L^0	Unstretched laminar flame speed [m/s].
S_T	Turbulent flame speed [m/s].
$\tilde{S}_{ij}$	Favre-filtered strain rate tensor [1/s].
Sc_t	Turbulent Schmidt number.
t	Time [s].
T	Temperature [K].
T_{ad}	Adiabatic flame temperature [K].
T_b	Burnt gas temperature [K].
T_u	Unburnt gas temperature [K].
u_i	Velocity component in direction i [m/s].
u'	Root-mean-square turbulent velocity fluctuation [m/s].
u'_Δ	Subgrid-scale velocity fluctuation [m/s].
u_η	Kolmogorov velocity scale [m/s].
V_j^c	Correction velocity for mass conservation [m/s].
W	Mean molecular weight of the mixture [kg/mol].
W_k	Molecular weight of species k [kg/mol].
x_i	Spatial coordinate in direction i [m].
X_k	Mole fraction of species k.
Y_k	Mass fraction of species k.
Y_F	Fuel mass fraction.
Y_O	Oxidiser mass fraction.
Z	Mixture fraction.
Z_{st}	Stoichiometric mixture fraction.

Table 2: Greek symbols.

Symbol	Description
α	Thermal diffusivity, $\alpha = \lambda/(\rho c_p)$ [m^2/s].
β	Power-law exponent in Charlette efficiency function ($\beta \approx 0.5$).
Γ	Efficiency function parameter in Colin/Charlette models.
Γ_Δ	Scale-dependent efficiency function parameter.
δ_{ij}	Kronecker delta.
δ_L	Laminar flame thickness [m].
δ_L^0	Unstretched laminar flame thickness [m].
δ_L^F	Thickened flame thickness, $\delta_L^F = F\delta_L^0$ [m].
Δ	LES filter width [m].
Δ_e	Effective filter width for efficiency function [m].
Δx	Grid spacing in x-direction [m].
Δt	Time step [s].
ε	Turbulent kinetic energy dissipation rate [m^2/s^3].
η	Kolmogorov length scale [m].
κ	Flame stretch rate [1/s].
κ_{ridge}	Ridge curvature from Hessian analysis [1/m^2].
λ	Thermal conductivity [W/(m·K)].
λ	Taylor microscale [m] (context-dependent).
λ_{exp}	Maximum real eigenvalue of chemical Jacobian (CEMA) [1/s].
μ	Dynamic viscosity [Pa·s].
μ_{sgs}	Subgrid-scale dynamic viscosity [Pa·s].
μ_t	Turbulent (eddy) viscosity [Pa·s].
ν	Kinematic viscosity [m^2/s].
ν_{sgs}	Subgrid-scale kinematic viscosity [m^2/s].
$\nu'_{k,r}$	Stoichiometric coefficient of species k as reactant in reaction r.
$\nu''_{k,r}$	Stoichiometric coefficient of species k as product in reaction r.
Ξ	Flame wrinkling factor, ratio of wrinkled to projected flame area.
ρ	Mixture density [kg/m^3].
ρ_k	Partial density of species k [kg/m^3].
Σ	Flame surface density [1/m].
σ_c	Width parameter for Gaussian flame sensor.
σ_Z	Width parameter for mixture fraction sensor.
τ_c	Chemical time scale [s].
τ_η	Kolmogorov time scale [s].
τ_{ij}	Viscous stress tensor [Pa].
τ_{ij}^{sgs}	Subgrid-scale stress tensor [Pa].

Continued on next page

Table 2 – *Continued from previous page*

Symbol	Description
τ_t	Integral turbulent time scale [s].
τ_ψ	Relaxation time for transported sensor [s].
ϕ	Equivalence ratio.
ϕ	Arbitrary scalar variable (context-dependent).
ϕ_{st}	Stoichiometric oxygen-to-fuel mass ratio.
$\bar{\phi}$	Reynolds (spatially) filtered variable.
$\tilde{\phi}$	Favre (density-weighted) filtered variable.
$\Phi_{k,j}$	Interaction parameter in Wilke mixture rule.
χ	Scalar dissipation rate [1/s].
χ_q	Extinction scalar dissipation rate [1/s].
ψ	Fictitious species for relaxation flame sensor.
$\dot{\omega}_k$	Chemical production rate of species k [kg/(m^3·s)].
Ω	Flame sensor function.
Ω_0	Flame sensor threshold value.

Table 3: Subscripts and superscripts.

Symbol	Description
$(\cdot)_{ad}$	Adiabatic conditions.
$(\cdot)_b$	Burnt gas state.
$(\cdot)_{\text{eff}}$	Effective (modified) quantity.
$(\cdot)_f$	Forward reaction direction.
$(\cdot)_i, (\cdot)_j$	Tensor/vector component indices.
$(\cdot)_k$	Species index.
$(\cdot)_{\max}$	Maximum value.
$(\cdot)_r$	Reaction index.
$(\cdot)_{sgs}$	Subgrid-scale quantity.
$(\cdot)_{st}$	Stoichiometric conditions.
$(\cdot)_t$	Turbulent quantity.
$(\cdot)_u$	Unburnt gas state.
$(\cdot)^0$	Unstretched or reference state.
$(\cdot)^F$	Thickened flame quantity.
$\bar{(\cdot)}$	Reynolds or spatial filtering operation.
$\tilde{(\cdot)}$	Favre (density-weighted) filtering operation.
$\widehat{(\cdot)}$	Test filter operation (dynamic procedure).

Table 4: List of abbreviations.

Abbrev.	**Description**
ABCN	Adams-Bashforth Crank-Nicolson (time integration scheme).
AMR	Adaptive Mesh Refinement.
ATF	Artificially Thickened Flame (alternative name for TFM).
CEMA	Chemical Explosive Mode Analysis.
CFD	Computational Fluid Dynamics.
CNLF	Crank-Nicolson Leap-Frog (time integration scheme).
DNS	Direct Numerical Simulation.
DTF	Dynamically Thickened Flame.
EDC	Eddy Dissipation Concept.
FDF	Filtered Density Function.
FGM	Flamelet-Generated Manifolds.
FPDF	Filtered Probability Density Function.
FPV	Flamelet/Progress Variable.
FSD	Flame Surface Density.
HRR	Heat Release Rate.
IBM	Immersed Boundary Method.
IMEX	Implicit-Explicit (time integration schemes).
ITNFS	Intermittent Turbulence Net Flame Stretch.
LDA	Laser Doppler Anemometry.
LES	Large Eddy Simulation.
LIPF	Laser-Induced Predissociation Fluorescence.
MCNAB	Modified Crank-Nicolson Adams-Bashforth (time integration scheme).
MFLab	Multiphase Flow Laboratory (Laboratório de Mecânica dos Fluidos).
MFSim	Multiphase Flow Simulator.
MMS	Method of Manufactured Solutions.
MPI	Message Passing Interface.
MTFM	Modified Thickened Flame Model.
ODE	Ordinary Differential Equation.
PDF	Probability Density Function.
PID	Proportional-Integral-Derivative (controller).
PISO	Pressure-Implicit with Splitting of Operators.
RANS	Reynolds-Averaged Navier-Stokes.
RFG	Random Flow Generation.
RMS	Root Mean Square.
SBDF	Semi-implicit Backward Differencing Formula.
SGS	Subgrid-Scale.

Continued on next page

Table 4 – *Continued from previous page*

Abbrev.	**Description**
S-TF	Stretched-Thickened Flame.
TFM	Thickened Flame Model.
TKE	Turbulent Kinetic Energy.
TVD	Total Variation Diminishing.
UFU	Universidade Federal de Uberlândia.
URANS	Unsteady Reynolds-Averaged Navier-Stokes.
WENO	Weighted Essentially Non-Oscillatory.

Table of Contents

INTRODUCTION

1.1 Motivation and Context

Turbulent combustion lies at the heart of modern energy systems, powering everything from electricity generation to industrial manufacturing. In the oil and gas industry specifically, combustion processes operate under demanding conditions where safety, efficiency, and environmental compliance must be simultaneously achieved.

Gas turbines for power generation and mechanical drive applications, industrial furnaces and process heaters, flare systems for safe disposal of hydrocarbon streams, and gas compression stations all rely on the controlled release of chemical energy through combustion (TURNS, 2012; LAW, 2010). The economic stakes are enormous: a single percentage point improvement in gas turbine efficiency can translate into millions of dollars in fuel savings over a plant's operational lifetime, while unplanned shutdowns due to combustion instabilities or equipment damage carry costs that extend well beyond direct maintenance expenses (LIEUWEN; YANG, V., 2005).

The engineering challenge in these applications stems from the inherently complex nature of turbulent reacting flows. Unlike laminar flames, where chemical reactions proceed in an orderly, predictable manner, turbulent combustion involves a chaotic interplay between fluid motion and chemistry across a vast range of spatial and temporal scales (PETERS, 2000).

Large turbulent eddies continuously stretch, distort, and fragment the flame surface, while small-scale turbulence enhances molecular mixing and heat transfer within the reaction zone. This multi-scale interaction fundamentally determines flame stability, pollutant formation, heat release distribution, and ultimately, the operational envelope of combustion equipment.

Understanding and predicting these phenomena through computational methods has become essential for modern combustor design, as physical testing alone cannot explore the full parameter space within practical time and budget constraints (POINSOT; VEYNANTE, 2005).

1.1.1 Computational Approaches to Turbulent Combustion

Direct Numerical Simulation (DNS) represents the most fundamental approach to turbulent combustion modelling, resolving all scales of motion from the largest energy-containing eddies down to the smallest transformative structures, along with the complete chemical kinetics (CHEN, J. H. et al., 2009). While DNS provides unprecedented insight into flame physics and has proven invaluable for developing and validating turbulent combustion models, its computational requirements scale prohibitively with Reynolds number.

For a typical industrial gas turbine combustor operating at Reynolds numbers of 10^5–10^6, DNS would require grids with 10^{15}–10^{18} points—a computational burden that remains beyond current computing capabilities (POPE, 2000). Even for laboratory-scale flames, DNS studies are typically restricted to simplified configurations, reduced chemistry, and limited physical time, making this approach unsuitable for industrial design and optimisation. Only a handful of research groups worldwide currently possess both the computational resources and the highly specialised codes required to perform DNS of turbulent reacting flows. Notable examples include the group of J.H. Chen at Sandia National Laboratories, which employs the massively parallel DNS solver S3D (CHEN, J. H. et al., 2009), and CERFACS in Toulouse, France, which has developed the AVBP code—a massively parallel solver for compressible reacting flows on unstructured grids (CERFACS, 2026). Despite these capabilities, DNS remains a fundamental research tool rather than an engineering design methodology.

Reynolds-Averaged Navier-Stokes (RANS) simulations occupy the opposite end of the computational spectrum, modelling all turbulent fluctuations and computing only time-averaged quantities (WILCOX, 1998). This approach has dominated industrial CFD practice for decades due to its modest computational requirements, typically enabling simulations on engineering workstations within hours. However, RANS fundamentally cannot capture the unsteady phenomena that govern many critical combustion behaviours.

Thermoacoustic instabilities—the coupling between heat release oscillations and acoustic modes that can lead to catastrophic hardware damage—are inherently transient phenomena invisible to steady RANS calculations (LIEUWEN; YANG, V., 2005; POINSOT, 2017). Similarly, flame flashback and blow-off events, ignition sequences, and the dynamics of flame-vortex interactions all require resolution of temporal fluctuations that RANS averages away. As emissions regulations tighten and combustor designs push toward leaner operation near

the stability boundary, the limitations of RANS-based predictions become increasingly problematic.

Large Eddy Simulation (LES) has emerged as a compelling intermediate method between DNS and RANS, explicitly resolving the large, energy-containing turbulent structures while modelling only the effects of small-scale motions below the chosen cut frequency of the kinetic energy spectrum or grid resolution itself (POPE, 2000; SAGAUT, 2006).

For combustion applications, LES offers the crucial ability to capture unsteady flame dynamics, mixing processes, and flame-acoustics interactions that determine combustor operability (PITSCH, 2006; VEYNANTE; VERVISCH, 2002). Over the past two decades, LES has progressed from an academic research tool to an increasingly practical engineering method, driven by advances in both computing hardware and numerical algorithms.

Yet applying LES to turbulent combustion introduces a fundamental challenge absent in non-reacting flows: the flame itself occupies a spatial scale far smaller than what can be economically resolved. A typical hydrocarbon-air flame front has a thickness on the order of 0.1–1 mm, determined by the balance between molecular diffusion and chemical reaction rates (PETERS, 2000). To adequately resolve this thin reaction zone using conventional numerical methods would require grid spacing of order 10–100 μm, resulting in grid counts that approach DNS requirements and negate the computational advantage of LES. This "flame resolution problem" has motivated extensive research into combustion models that enable LES on practical grids without explicitly resolving the flame structure (PITSCH, 2006).

1.1.2 The Thickened Flame Model

The Thickened Flame Model (TFM), introduced by Butler and O'Rourke (BUTLER; O'ROURKE, 1977) and substantially developed by Colin et. al. (COLIN et al., 2000), offers an alternative solution to the flame resolution problem through a simple yet physically grounded transformation. Rather than attempting to resolve the actual flame thickness, TFM artificially thickens the flame to a scale resolvable on the LES grid while preserving the fundamental propagation characteristics.

This is achieved by simultaneously increasing the thermal and mass diffusivities by a thickening factor F while decreasing the reaction rate by the same factor. The resulting thickened flame propagates at the same laminar flame speed as the original thin flame but with a thickness increased by factor F, making it resolvable on coarser computational grids. The

mathematical basis for this transformation, rooted in the fundamental scaling relationships of premixed flame propagation, will be presented in detail in Chapter 2.

However, thickening the flame introduces a secondary effect: subgrid turbulent wrinkling, which increases the effective flame surface area and thus the turbulent burning velocity, becomes partially resolved rather than fully modelled (CHARLETTE; MENEVEAU; VEYNANTE, 2002a). A thicker flame is less susceptible to wrinkling by small turbulent eddies, potentially underestimating combustion intensity. To compensate, TFM incorporates an efficiency function that augments the reaction rate to account for lost subgrid wrinkling.

A critical refinement to the original TFM formulation is the introduction of sensor functions that localize the thickening to the flame region, leaving non-reacting flow unmodified (LEGIER; POINSOT; VEYNANTE, 2000). The sensor function is to identify cells within the reaction zone and activates thickening only where needed. This dynamic thickening approach ensures that turbulent mixing in non-reacting regions proceeds unaltered while enabling flame resolution where chemical reactions occur.

Several characteristics make TFM particularly attractive for implementation in the in-house code MFSim and for oil and gas industry applications.

First, the explicit coupling between grid resolution and thickening factor provides direct control over the trade-off between accuracy and computational cost—a critical consideration for engineering design cycles.

Second, TFM's compatibility with detailed chemical mechanisms enables prediction of minor species relevant to emissions (NO_x, CO) and flame stability, capabilities that tabulated chemistry approaches may sacrifice for computational efficiency (WANG; BOILEAU; VEYNANTE, 2011).

Third, the model's local formulation integrates naturally with adaptive mesh refinement (AMR) strategies, allowing computational resources to concentrate near the flame while using coarser resolution in non-reacting regions (MOUREAU; DOMINGO; VERVISCH, 2011). This AMR compatibility is particularly valuable for industrial geometries where flames occupy a small fraction of the total computational domain.

Despite these advantages, the classical TFM formulation is not without limitations, and recent research has identified several theoretical boundaries that define the current state of the art. The most fundamental concerns the flame response to stretch: as shown by Detomaso et al. (DE TOMASO; RIBER; CUENOT, 2023), the thickening transformation amplifies the

Markstein length by a factor F, causing thickened flames to overpredict sensitivity to strain and curvature—an effect particularly severe for mixtures with Lewis numbers far from unity. The efficiency function closure, whether based on DNS-calibrated spectral models (COLIN et al., 2000), fractal power-law formulations (CHARLETTE; MENEVEAU; VEYNANTE, 2002a; WANG; BOILEAU; VEYNANTE, 2011), or dynamic variants (CHARLETTE; MENEVEAU; VEYNANTE, 2002b; VOLPIANI; SCHMITT, T.; VEYNANTE, 2016), relies on assumptions about the turbulence spectrum that may not hold universally, and the estimation of subgrid-scale velocity in reacting flows remains problematic due to dilatation effects (XIA et al., 2023). Furthermore, the extension of TFM to non-premixed combustion requires a fundamentally different formulation, as diffusion flames obey distinct scaling laws where the chemical source term does not control flame properties in the high-Damköhler regime (CUENOT; SHUMKIVAN; BLANCHARD, 2022)—a theoretical framework that still lacks complete subgrid-scale closure for turbulent applications. These open challenges, along with the various modelling choices for sensors, efficiency functions, and stretch corrections reviewed in detail in Chapter 2, motivate the specific TFM formulation adopted in this work for implementation in MFSim.

1.1.3 The Case for Open-Source CFD

The choice of MFSim as the implementation platform reflects broader trends in scientific computing and engineering practice. Commercial CFD packages, while offering polished user interfaces and extensive validation, typically function as "black boxes" that limit users' ability to inspect, modify, or extend underlying algorithms. For research applications developing novel physical models, this opacity presents a fundamental barrier: implementing new combustion models in proprietary software requires either vendor collaboration or reverse engineering, neither of which supports the rapid iteration essential for research progress. Furthermore, commercial licensing costs can be prohibitive for universities, small enterprises, and researchers in developing economies, creating barriers to participation in computational combustion research.

Open-source CFD solvers address these limitations by providing full access to source code, enabling modification, extension, and rigorous verification of numerical methods. MFSim, developed within the MFLab research group at the Federal University of Uberlândia (UFU), represents such a platform specifically designed for multiphase and reacting flow simulations. Built

on block-structured adaptive mesh refinement with parallel scalability through MPI, MFSim provides the computational infrastructure necessary for LES of industrial combustion systems.

1.1.4 Industrial Applications Context

The industrial applications motivating this work span the full range of oil and gas combustion equipment. Gas turbines represent perhaps the highest-value application, with modern combined-cycle plants achieving thermal efficiencies exceeding 60% while meeting stringent NO_x emissions limits through lean premixed combustion (LIEUWEN; YANG, V., 2005). These machines operate with flame temperatures and pressures where small design changes can trigger thermoacoustic instabilities or blow-off, making accurate unsteady simulation essential for development. LES with TFM has demonstrated capability for capturing these phenomena in laboratory and simplified industrial configurations (ZHANG, H. et al., 2017), though validation against full-scale gas turbine data remains an active research frontier.

Industrial flares and thermal oxidizers present different modelling challenges centred on non-premixed combustion. These systems must safely combust variable fuel streams—potentially ranging from pure methane to heavy hydrocarbons with varying hydrogen sulfide content—while meeting destruction efficiency requirements and minimizing visible emissions. The diffusion flame regime requires different sensor functions than premixed combustion, motivating the multi-regime TFM approach developed in a few works (CUENOT; SHUM-KIVAN; BLANCHARD, 2022). Similarly, process heaters and furnaces involve both premixed burner flames and subsequent mixing with furnace gases, creating partially premixed conditions that challenge single-regime models.

This dissertation addresses the need for validated, accessible LES combustion modelling tools by implementing and validating the TFM within MFSim. The implementation encompasses premixed flame regime through appropriate sensor function formulations, with also description of non-premixed mathematical framework, with partially premixed capability identified for future development. Validation proceeds systematically from laminar reference cases through turbulent laboratory flames, establishing the accuracy and limitations of the approach before industrial application.

1.2 Objectives

This dissertation aims to extend the combustion modelling capabilities of MFSim through the implementation, verification, and validation of the TFM for LES of turbulent reacting flows. The work is structured around primary and secondary objectives that progressively build up.

1.2.1 Primary Objective

The primary objective of this work is to implement the TFM within the MFSim computational framework. This implementation encompasses the core TFM formulation, including the thickening transformation of diffusivity and reaction rate, the efficiency function to compensate for lost subgrid flame wrinkling, and sensor functions to localize thickening within the reaction zone.

The implementation follows a modular software architecture that facilitates future extensions and modifications. Complete documentation of the code structure, input parameters, and computational workflow accompanies the implementation.

1.2.2 Secondary Objectives

The secondary objectives focus on validating the TFM implementation:

- **Premixed combustion validation** employing a dynamic TFM approach with sensor functions, is validated through test cases. Two-dimensional turbulent premixed flames, to demonstrates the model's ability to capture flame brush characteristics and velocity statistics against experimental reference data;

- **Grid sensitivity and parameter studies** quantifying the sensitivity of results to key model parameters, particularly the maximum thickening factor $F_{\max}$. Grid convergence studies establish the relationship between mesh resolution, thickening factor, and solution accuracy, providing practical guidance for industrial applications where computational resources constrain mesh density.

1.2.3 Scope and Delimitations

To maintain focus and feasibility within the time frame of a master's dissertation, certain topics are explicitly excluded from the present scope:

- **Non-premixed and Partially premixed combustion**: While the theoretical framework for combined premixed and non-premixed sensors is presented, full implementation and validation of non-premixed and partially premixed capabilities is designated as future work;
- **Industrial geometry simulations**: Validation focuses on canonical laboratory configurations with well-characterized boundary conditions and experimental data; application to complex industrial geometries (e.g., full gas turbine combustors, industrial flares) is identified for subsequent studies;
- **Emissions modelling**: Prediction of pollutant species (NO_x, CO, soot) requires additional sub-models beyond the core TFM formulation and is not addressed in the present validation campaign;
- **Thermoacoustic coupling**: Although TFM-LES is capable of capturing combustion instabilities, systematic validation against thermoacoustic test cases is beyond the current scope.

These delimitations ensure that the core objectives—implementation, verification, and validation of TFM for premixed regime—receive thorough treatment while establishing clear directions for continued development.

1.3 Dissertation Structure

This dissertation is organized into six chapters that progress from theoretical foundations through implementation details to validation results and conclusions.

Chapter 1: introduces the industrial and scientific motivation, presents the TFM as the chosen approach to address the flame resolution problem in LES, and defines research objectives with explicit scope delimitations.

Chapter 2: provides theoretical foundations covering turbulent combustion fundamentals, LES methodology, combustion modelling approaches, and a detailed review of TFM development and current state of the art.

Chapter 3: presents the mathematical framework for reacting flows under LES filtering and TFM formulation, MFSim's numerical methods, and specific implementation details of the TFM module.

Chapter 4: demonstrates implementation correctness through systematic verification tests (passive mode, constant thickening, sensor function) and validation against canonical premixed combustion configurations.

Chapter 5: synthesizes the findings from validation and performance studies. Key results are summarized, highlighting successes and identifying limitations of the current implementation. The assumptions underlying efficiency function calibration, sensor threshold selection, and chemical mechanism choice are critically examined.

Chapter 6: summarizes the contributions of this dissertation and charts directions for continued development. Future work is organized by time frame: short-term refinements to model parameters and sensor functions, medium-term extensions to partially premixed combustion and advanced efficiency models, and long-term applications to industrial configurations, transient phenomena, and emissions prediction.

Appendices provide supplementary material including chemical mechanism details, input file examples, mathematical derivations, code structure documentation, and validation data sources.

LITERATURE REVIEW

This chapter establishes the theoretical foundations underlying the TFM and its application to turbulent combustion simulation. The review progresses from fundamental concepts of turbulent reacting flows through LES methodology to specific combustion modelling approaches, culminating in a detailed examination of TFM development and current state of the art.

2.1 Turbulent Combustion Fundamentals

Turbulent combustion involves the simultaneous occurrence of turbulent fluid motion and exothermic chemical reactions, creating a coupled system of extraordinary complexity. The interaction between turbulence and chemistry spans multiple orders of magnitude in both length and time scales, from the molecular level where chemical bonds break and form to the integral scale of the largest turbulent eddies. Understanding this multi-scale interaction is essential for developing and applying combustion models, as the dominant physical mechanisms vary dramatically across different operating regimes.

2.1.1 Turbulence-Chemistry Interaction

The fundamental challenge in turbulent combustion arises from the nonlinear coupling between fluid dynamics and chemical kinetics (PETERS, 2000). Turbulent motions affect combustion by enhancing mixing between reactants and products, increasing heat and mass transfer rates, and distorting the flame surface. Conversely, combustion affects turbulence through volumetric expansion associated with heat release, which accelerates the flow and generates vorticity due to density gradients, and through changes in fluid properties with temperature (POINSOT; VEYNANTE, 2005).

The relative importance of these interactions depends on the ratio of characteristic turbulent and chemical scales. When chemical reactions are fast compared to turbulent mixing,

chemistry occurs in thin layers that are wrinkled and stretched by the turbulent flow but maintain their internal structure—the flamelet regime. When turbulent mixing is fast compared to chemistry, reactions occur in a distributed manner throughout the turbulent field—the distributed reaction regime. Between these extremes lies a continuum of behaviours that challenges both physical understanding and numerical modelling.

Molecular transport plays a crucial role in turbulent combustion, particularly near the reaction zone where steep gradients in temperature and species concentration exist. The Lewis number, defined as the ratio of thermal to mass diffusivity:

$$\mathrm{Le} = \frac{\alpha}{D} = \frac{\lambda}{\rho c_p D}, \tag{2.1.1}$$

where α is thermal diffusivity, D is mass diffusivity, λ is thermal conductivity, ρ is density, and c_p is specific heat capacity, characterizes the relative rates of heat and mass transport. For hydrocarbon-air flames, Lewis number is typically close to unity for major species, simplifying analysis, though differential diffusion effects become important for light species such as hydrogen and radicals, also for predicting minor species including pollutants.

The Damköhler number quantifies the ratio of turbulent to chemical time scales:

$$\mathrm{Da} = \frac{\tau_t}{\tau_c} = \frac{l_t/u'}{\delta_L/S_L}, \tag{2.1.2}$$

where $\tau_t = l_t/u'$ is the integral turbulent time scale based on integral length scale l_t and turbulent velocity fluctuation u', and $\tau_c = \delta_L/S_L$ is the chemical time scale based on flame thickness δ_L and laminar flame speed S_L. Large Damköhler numbers ($\mathrm{Da} \gg 1$) indicate fast chemistry relative to turbulent transport, favouring flamelet behaviour. Small Damköhler numbers ($\mathrm{Da} \ll 1$) indicate slow chemistry, leading to distributed reactions or possible extinction. It concretely represents whether the fluid stays in the reactor long enough for the chemical reaction to occur.

The Karlovitz number provides a complementary characterization based on the smallest turbulent scales:

$$\mathrm{Ka} = \frac{\tau_c}{\tau_\eta} = \frac{\delta_L/S_L}{\eta/u_\eta} \tag{2.1.3}$$

where $\tau_\eta = \eta/u_\eta$ is the Kolmogorov time scale, η is the Kolmogorov length scale, and u_η is the Kolmogorov velocity scale. While the Damköhler number compares chemistry against the large-scale turbulent transport, the Karlovitz number compares it against the smallest and

most intense turbulent motions. It effectively measures the strain rate imposed by turbulence on the flame front, since $1/\tau_\eta$ represents the characteristic turbulent strain rate at the dissipative scales and $1/\tau_c$ represents the characteristic chemical rate. From a spatial perspective, Ka can be equivalently expressed as $\mathrm{Ka} = (\delta_L/\eta)^2$, directly comparing the flame thickness to the Kolmogorov length scale: for $\mathrm{Ka} < 1$, the flame is thinner than the smallest eddies and its internal structure remains undisturbed by turbulence; for $\mathrm{Ka} > 1$, the Kolmogorov eddies are small enough to penetrate the flame and enhance transport within the preheat and eventually the reaction zone. It concretely represents whether the smallest turbulent structures can mechanically disrupt the flame, in contrast to the Damköhler number which represents whether the flow resides long enough for chemistry to proceed to completion.

2.1.2 Flame Regimes and the Borghi Diagram

The classification of turbulent combustion regimes is commonly visualized through the Borghi diagram (also known as the Peters diagram or combustion regime diagram), which maps flame behaviour as a function of velocity ratio u'/S_L and length scale ratio l_t/δ_L (BORGHI, 1985; PETERS, 2000). This diagram, illustrated conceptually in Figure 2.1, delineates distinct regimes based on the Damköhler and Karlovitz numbers.

A. **Laminar flames** ($\mathrm{Re}_t < 1$): When the turbulent Reynolds number $\mathrm{Re}_t = u' l_t/\nu$ is less than unity, the flow is not turbulent and laminar flame theory applies. This regime serves as the foundation for understanding flame structure and provides reference quantities (flame speed, thickness) used to characterize turbulent flames;

B. **Wrinkled flamelets** ($\mathrm{Ka} < 1$, $\mathrm{Da} > 1$): In this regime, turbulent eddies are larger than the flame thickness, and turbulent velocities are smaller than the laminar flame speed. Temporally, the chemical time scale is shorter than both the Kolmogorov and integral turbulent time scales ($\tau_c < \tau_\eta < \tau_t$), meaning that the flame reacts faster than any turbulent motion can distort it. The flame surface is gently wrinkled by large-scale motions but retains its laminar internal structure, behaving as a collection of laminar flamelets that propagate at the local laminar flame speed;

C. **Corrugated flamelets** ($\mathrm{Ka} < 1$, $\mathrm{Da} > 1$, $u' > S_L$): As turbulent intensity increases, the flame surface becomes increasingly convoluted, forming pockets and cusps. The chemical time scale remains shorter than the Kolmogorov time scale ($\tau_c < \tau_\eta$), preserving the

laminar internal flame structure (Ka < 1), but the large-scale turbulent time scale now becomes comparable to or shorter than the flame transit time, substantially increasing the flame surface area and enhancing global burning rates. This regime is common in practical premixed combustion systems including gas turbines and spark-ignition engines;

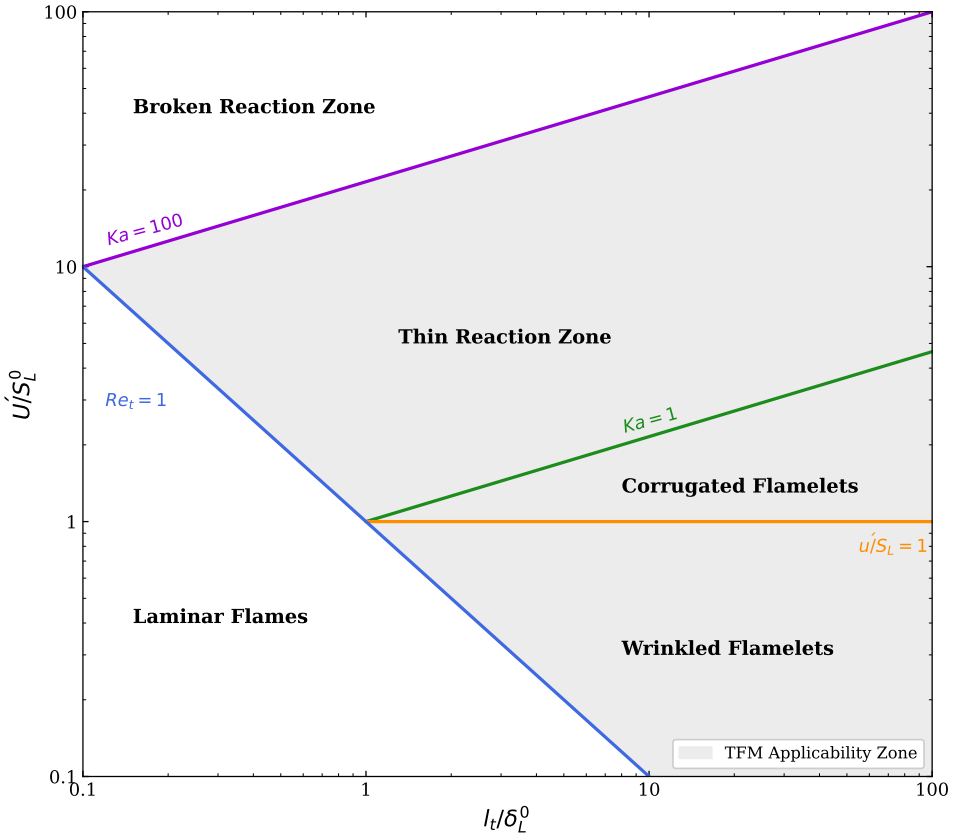

Figure 2.1: Borghi diagram showing turbulent premixed combustion regimes as a function of normalized turbulent velocity u'/S_L and length scale ratio l_t/δ_L.

D. **Thin reaction zones** ($1 < \mathrm{Ka} < 100$, $\mathrm{Ka}_\delta < 1$): When the Karlovitz number exceeds unity, the Kolmogorov time scale becomes shorter than the chemical time scale ($\tau_\eta < \tau_c$), meaning that the smallest eddies fluctuate faster than the flame can respond, and they penetrate the preheat zone. The regime boundary $\mathrm{Ka} \approx 100$ corresponds to the condition $\mathrm{Ka}_\delta \approx 1$, where Ka_δ is the Karlovitz number based on the reaction zone thickness δ_r:

$$\mathrm{Ka}_\delta = \frac{\tau_r}{\tau_\eta} = \left(\frac{\delta_r}{\eta}\right)^2, \tag{2.1.4}$$

with δ_r typically an order of magnitude thinner than the full flame thickness ($\delta_r \approx \delta_L/10$ for hydrocarbon-air flames from activation energy asymptotic (POINSOT; VEYNANTE,

2005)), yielding the estimate $\mathrm{Ka}_\delta \approx \mathrm{Ka}/100$. As long as $\mathrm{Ka}_\delta < 1$, the reaction zone time scale τ_r remains shorter than τ_η, so the reaction layer reacts faster than the smallest eddies can disrupt it and retains its thin, laminar-like structure. Turbulent transport enhances heat and mass transfer in the preheat zone, potentially thickening this region, while reactions still occur in a thin layer;

E. **Broken reaction zones** ($\mathrm{Ka}_\delta > 1$, equivalently $\mathrm{Ka} \gtrsim 100$): At very high Karlovitz numbers, the Kolmogorov time scale becomes shorter than even the reaction zone time scale ($\tau_\eta < \tau_r$), meaning that turbulent fluctuations are faster than the chemical reactions sustaining the flame. Turbulent eddies penetrate the reaction zone, potentially causing local extinction and leading to distributed or broken flame structures. This regime is characterized by strong departures from flamelet behaviour and presents significant modelling challenges.

The boundaries between regimes are not sharp transitions but rather gradual changes in dominant physical mechanisms. Moreover, practical combustion devices often operate across multiple regimes simultaneously or transiently. The TFM, as will be discussed in subsequent sections, is primarily applicable in the flamelet and thin reaction zone regimes where the flame retains a coherent structure that can be characterized by propagation speed and thickness.

2.1.3 Premixed Combustion

In premixed combustion, fuel and oxidizer are mixed prior to reaching the reaction zone, and a self-propagating flame front separates reactants from products (LAW, 2010), Figure 2.2 is a diagram illustrating this behaviour. The laminar premixed flame provides the fundamental reference state, characterized by two key quantities: the laminar flame speed S_L and the laminar flame thickness δ_L.

The laminar flame speed represents the velocity at which the flame front propagates into the unburnt mixture in the direction normal to the flame surface. For a one-dimensional steady flame, S_L is determined by the balance between heat release, thermal conduction, and mass diffusion . Typical values for stoichiometric hydrocarbon-air flames at atmospheric conditions range from 0.3–0.45 m/s, depending on the fuel (TURNS, 2012). The flame speed varies with equivalence ratio, pressure, and unburnt gas temperature, generally increasing with temperature and exhibiting a maximum near stoichiometric or slightly rich conditions.

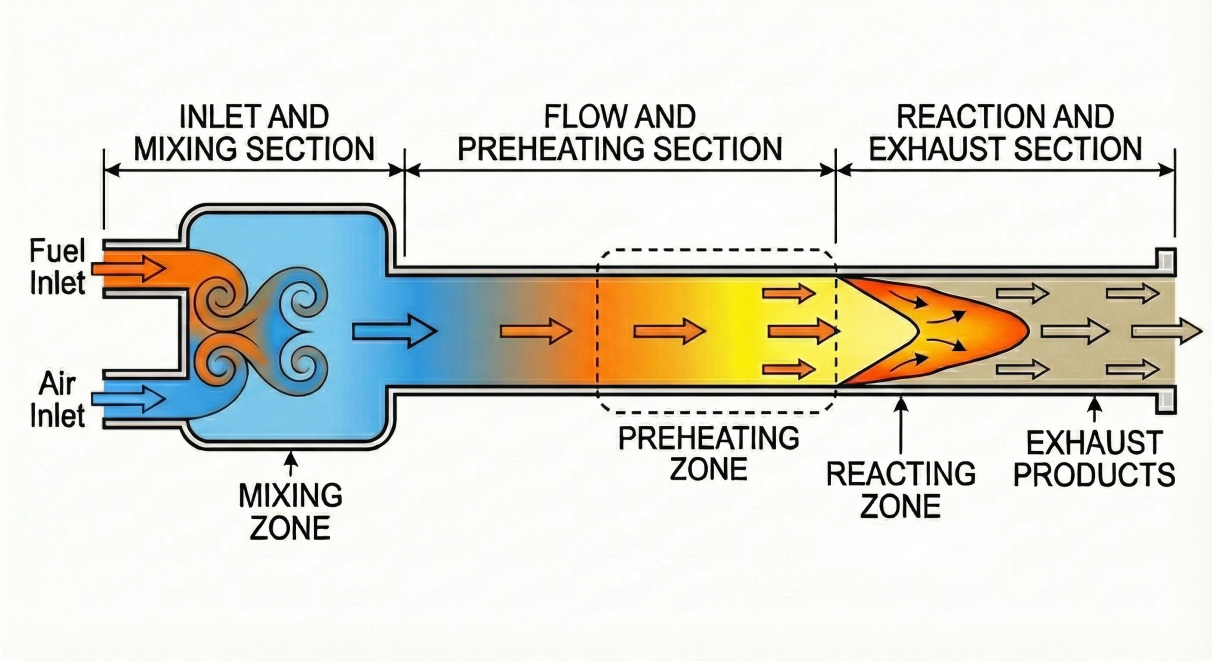

Figure 2.2: Premixed flame diagram.

The laminar flame thickness can be defined in several ways. The thermal thickness, based on the temperature gradient:

$$\delta_L = \frac{T_b - T_u}{(\partial T/\partial x)_{\max}}, \tag{2.1.5}$$

where T_b and T_u are burnt and unburnt gas temperatures. Alternative definitions based on species profiles or reaction rate distributions may yield different numerical values but similar scaling behaviour.

In turbulent premixed combustion, the flame surface is wrinkled by turbulent motions, increasing the effective flame area and thereby the global consumption rate of reactants. The turbulent flame speed S_T, defined as the mass consumption rate per unit projected flame area, exceeds the laminar flame speed by a factor that depends on the turbulence characteristics. Empirical correlations and theoretical models relate S_T/S_L to parameters such as u'/S_L, with typical values ranging from 2 to 10 in practical combustors.

The progress variable c provides a convenient scalar for tracking the extent of reaction in premixed flames. Defined to vary from zero in unburnt reactants to unity in fully burnt products, the progress variable can be based on temperature:

$$c = \frac{T - T_u}{T_b - T_u} \tag{2.1.6}$$

or on species mass fractions, such as a normalized sum of product species. The progress variable satisfies a transport equation that, for unity Lewis number, has a source term proportional to the reaction rate. This scalar plays a central role in many combustion models, including the sensor functions used in TFM.

2.1.4 Non-Premixed Combustion

In non-premixed (diffusion) combustion, fuel and oxidizer enter the reaction zone from separate streams, and burning occurs where they mix in appropriate proportions (PETERS, 2000), the diagram, Figure 2.3, illustrate this mechanism. Unlike premixed flames, non-premixed flames do not propagate; their position is determined by the mixing field rather than a balance between convection and reaction.

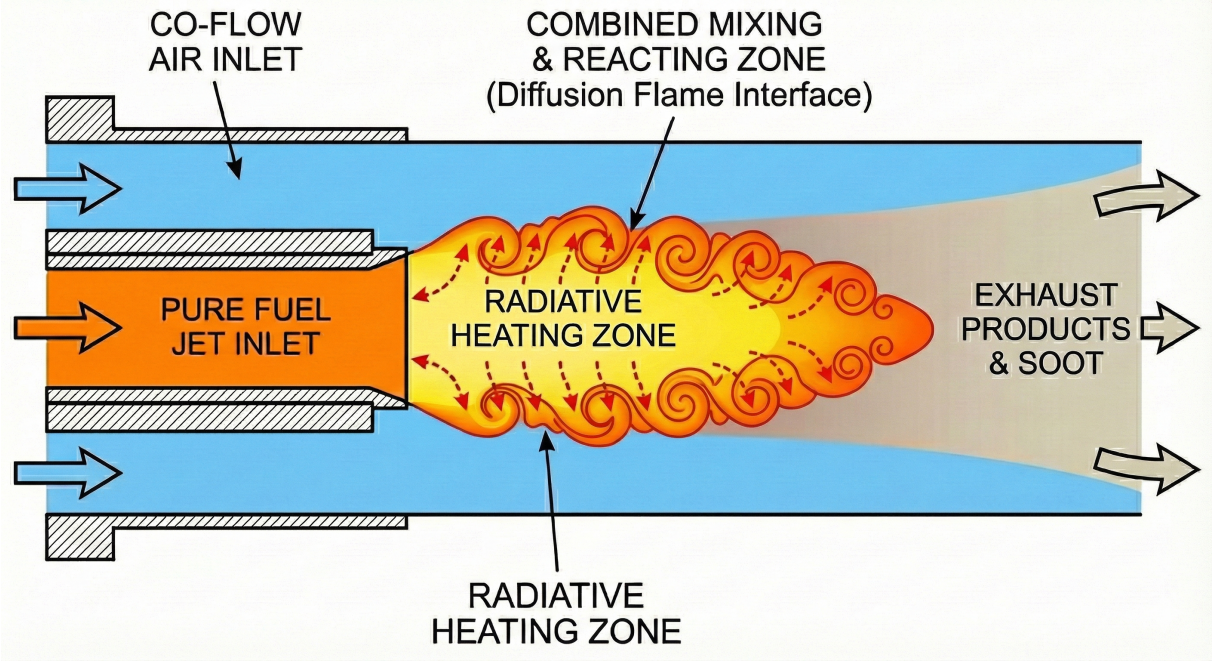

Figure 2.3: Non-premixed flame diagram.

The mixture fraction Z is the fundamental conserved scalar for non-premixed combustion, representing the local mass fraction originating from the fuel stream. For a two-stream problem (fuel and oxidizer), $Z = 1$ in pure fuel, $Z = 0$ in pure oxidizer, and intermediate values indicate mixed fluid (POINSOT; VEYNANTE, 2005). The mixture fraction satisfies a balance equation without chemical source terms:

$$\frac{\partial \rho Z}{\partial t} + \nabla \cdot (\rho \mathbf{u} Z) = \nabla \cdot (\rho D \nabla Z), \tag{2.1.7}$$

making it particularly prone to modelling.

For a given chemical system, there exists a stoichiometric mixture fraction Z_{st} at which fuel and oxidizer are present in exactly the proportions required for complete combustion. For methane-air combustion:

$$Z_{st} = \frac{1}{1 + \phi_{st}(Y_{O_2,\infty}/Y_{F,\infty})(W_F/W_{O_2})}, \tag{2.1.8}$$

where ϕ_{st} is the stoichiometric oxygen-to-fuel mass ratio, $Y_{O_2,\infty}$ and $Y_{F,\infty}$ are the oxidizer and fuel mass fractions in their respective streams, and W_F and W_{O_2} are molecular weights.

In the flamelet regime, non-premixed combustion occurs in thin layers near the stoichiometric surface $Z = Z_{st}$. The structure of these flamelets is transported by the scalar dissipation rate:

$$\chi = 2D|\nabla Z|^2, \tag{2.1.9}$$

which quantifies the rate of molecular mixing. High scalar dissipation rates increase diffusive transport within the flamelet, potentially leading to extinction when heat losses to the surroundings exceed heat release from reactions. The extinction scalar dissipation rate χ_q defines the limiting condition for flamelet survival.

To understand the physics governing flamelet structure and extinction, it is instructive to consider limiting cases that bracket the behaviour of real flames. Two fundamental limits define the extremes of non-premixed combustion: the fast chemistry limit, where reactions are infinitely rapid compared to mixing, and the extinction limit, where mixing overwhelms chemical reaction.

The Burke-Schumann limit represents the idealized case of infinitely fast chemistry, where reactions are confined to an infinitely thin stoichiometric surface (BURKE; SCHUMANN, 1928). In their seminal analysis, Burke and Schumann derived analytical solutions for laminar diffusion flames by assuming that fuel and oxidizer cannot coexist—any mixture reaching stoichiometric proportions reacts instantaneously to completion. This assumption eliminates chemical kinetics from the problem, reducing flame structure to a purely mixing-controlled process where temperature and species mass fractions become unique functions of mixture fraction. While real flames depart from this idealization due to finite-rate chemistry, the Burke-Schumann solution provides fundamental insight into diffusion flame geometry and

established the mixture fraction as the reference scalar for analysing non-premixed combustion.

2.1.5 Partially Premixed Combustion

Many practical combustion systems operate in partially premixed or stratified modes, where the equivalence ratio varies spatially or temporally throughout the combustion zone (VEYNANTE; VERVISCH, 2002). Gas turbine combustors with pilot flames, lifted jet flames, and stratified-charge engines all exhibit partially premixed characteristics. In these systems, both premixed and non-premixed combustion mechanisms may be active simultaneously or in different regions of the flow.

The flame index or Takeno index (YAMASHITA; SHIMADA; TAKENO, 1996), provides a mean of distinguishing locally between premixed and non-premixed combustion:

$$\mathrm{GFI} = \nabla Y_F \cdot \nabla Y_O, \tag{2.1.10}$$

where Y_F and Y_O are fuel and oxidizer mass fractions. Positive values indicate premixed combustion (fuel and oxidizer gradients aligned, both diffusing toward the reaction zone from the same side), while negative values indicate non-premixed combustion (gradients opposed, fuel and oxidizer approaching from opposite sides). Normalization of this index yields values between -1 and $+1$, facilitating regime identification in computational studies and enabling weighted contributions from premixed and non-premixed sub-models in multi-regime approaches.

Modelling partially premixed combustion requires frameworks that can capture both propagating premixed flame fronts and mixing-controlled diffusion flames, potentially within the same computational cell. Multi-regime approaches combine elements from premixed and non-premixed models, often using the flame index to weight contributions from each mechanism.

2.1.6 Characteristic Scales in Turbulent Combustion

The multi-scale nature of turbulent is characterized by a hierarchy of length and time scales spanning several orders of magnitude (POPE, 2000). Understanding these scales is essential for determining resolution requirements and identifying appropriate modelling strategies.

The largest turbulent motions occur at the integral scale l_t, which is comparable to the geometric dimensions of the flow. These energy-containing eddies have velocity scale u' and time scale $\tau_t = l_t/u'$ (TENNEKES; LUMLEY, 1972). Energy cascades from large to small scales through the inertial subrange, where the turbulent kinetic energy spectrum follows the Kolmogorov $-5/3$ power law. At the smallest scales, viscosity transform turbulent kinetic energy to heat. The Kolmogorov scales, derived from dimensional analysis assuming local isotropy at small scales (POPE, 2000), characterize this transformative range:

$$\eta = \left(\frac{\nu^3}{\varepsilon}\right)^{1/4}, \quad u_\eta = (\nu\,\varepsilon)^{1/4}, \quad \tau_\eta = \left(\frac{\nu}{\varepsilon}\right)^{1/2}, \tag{2.1.11}$$

where ν is kinematic viscosity and ε is the turbulent dissipation rate. The ratio of integral to Kolmogorov scales grows with Reynolds number: $l_t/\eta \sim \mathrm{Re}_t^{3/4}$ (TENNEKES; LUMLEY, 1972).

The laminar flame thickness δ_L and flame time $\tau_c = \delta_L/S_L$ characterize premixed combustion. For non-premixed flames, the reaction zone thickness scales with the inverse of scalar dissipation rate (PETERS, 1984). Chemical time scales for individual reactions span an enormous range, from nanoseconds for radical reactions to milliseconds for NO_x formation (LAW, 2010).

Table 2.1 summarizes typical values of characteristic scales for a representative turbulent premixed flame, illustrating the scale separation that motivates the development of combustion subgrid models.

Table 2.1: Characteristic scales for a representative turbulent premixed methane-air flame at atmospheric pressure. Values are order-of-magnitude estimates for a laboratory-scale burner (PETERS, 2000).

Scale	**Length**	**Time**
Integral (l_t, τ_t)	10 mm	1 ms
Kolmogorov (η, τ_η)	50 μm	50 μs
Laminar flame (δ_L, τ_c)	0.5 mm	1 ms
Gibson (l_G)	0.5 mm	—

The Gibson scale l_G, introduced by (PETERS, 1988) , is defined as the size of eddies having velocity equal to the laminar flame speed ($u'(l_G) = S_L$). This scale marks the transition between eddies that wrinkle the flame (larger scales) and those that are unable to significantly distort it (smaller scales). For $l_G > \eta$, a range of scales exists that wrinkle the flame without penetrating its structure, corresponding to the flamelet regime.

This hierarchy of scales, combined with the regime classifications presented earlier, provides the framework for understanding when and how the TFM can be applied effectively. The applicability of the model is intrinsically tied to the flamelet hypothesis, which assumes that the flame retains a coherent structure characterizable by a propagation speed and well-defined thickness. This assumption holds in the wrinkled flamelets, corrugated flamelets, and thin reaction zones regimes, but breaks down in the broken reaction zones regime, where turbulent eddies disrupt the reaction zone itself, leading to local extinction and distributed combustion. Similarly, at very low Damköhler numbers, reactions become volumetrically distributed rather than confined to a propagating front. Consequently, the TFM navigates the resolution challenge while remaining applicable within the flamelet and thin reaction zone regimes where flame structure is coherent—conditions that characterize most practical premixed combustion devices including gas turbines and spark-ignition engines.

2.2 LES Fundamentals

The fundamental premise of LES is that large-scale turbulent motions, which carry most of the turbulent kinetic energy and are geometry-dependent, are resolved directly on the computational grid, while the effects of small-scale motions, which tend toward universal behaviour, are represented through subgrid-scale (SGS) models (POPE, 2000; SAGAUT, 2006). This section presents the LES foundations relevant to turbulent combustion simulation and the TFM.

2.2.1 LES Philosophy and Filtering

The physical justification for LES rests on the observation that turbulent flows exhibit distinct behaviour at different scales (TENNEKES; LUMLEY, 1972). Large eddies are directly influenced by boundary conditions and geometry, varying significantly between flow configurations. Small eddies, in contrast, tend toward local isotropy and exhibit more universal characteristics. This universality at small scales suggests that their effects can be parametrized through relatively simple models, while large-scale motions must be computed explicitly.

Scale separation in LES is achieved through spatial filtering. A filtered variable $\bar{\phi}$ is defined by convolution with a filter kernel G:

$$\bar{\phi}(\vec{x}, t) = \int G(\vec{x} - \vec{x}', \Delta)\, \phi(\vec{x}', t)\, d\vec{x}', \tag{2.2.1}$$

where Δ is the filter width, determining the scale of separation between resolved and modelled motions. In practice, the computational grid acts as an implicit filter, with the filter width equal to the local cell size $\Delta = (\Delta x \Delta y \Delta z)^{1/3}$.

For variable-density flows such as reacting systems, Favre (density-weighted) filtering avoids unclosed terms involving density fluctuations (POINSOT; VEYNANTE, 2005):

$$\tilde{\phi} = \frac{\overline{\rho\phi}}{\bar{\rho}}. \tag{2.2.2}$$

The Favre-filtered equations retain a form similar to the original balance equations, with subgrid terms appearing in analogous locations to Reynolds stress terms in RANS. Unlike Reynolds averaging, where $\overline{\phi'} = 0$, the LES-filtered fluctuation is generally non-zero ($\bar{\phi}' \neq 0$), leading to additional unclosed terms that require modelling.

2.2.2 Filtered Balance Equations

Application of Favre filtering to the Navier-Stokes equations yields the filtered balance equations governing LES of reacting flows. The system comprises conservation of mass, momentum, energy, and chemical species.

The filtered continuity equation retains its original form:

$$\frac{\partial \bar{\rho}}{\partial t} + \frac{\partial(\bar{\rho}\tilde{u}_j)}{\partial x_j} = 0. \tag{2.2.3}$$

The filtered momentum equation becomes:

$$\frac{\partial(\bar{\rho}\tilde{u}_i)}{\partial t} + \frac{\partial(\bar{\rho}\tilde{u}_i\tilde{u}_j)}{\partial x_j} = -\frac{\partial \bar{p}}{\partial x_i} + \frac{\partial \bar{\tau}_{ij}}{\partial x_j} - \frac{\partial \tau_{ij}^{sgs}}{\partial x_j}, \tag{2.2.4}$$

where $\bar{\tau}_{ij}$ is the filtered viscous stress tensor and τ_{ij}^{sgs} is the subgrid-scale stress tensor:

$$\tau_{ij}^{sgs} = \bar{\rho}\left(\widetilde{u_i u_j} - \tilde{u}_i\tilde{u}_j\right), \tag{2.2.5}$$

representing the effect of unresolved velocity fluctuations on the resolved flow.

The filtered energy equation, expressed in terms of temperature, takes the form:

$$\frac{\partial(\bar{\rho}\tilde{T})}{\partial t} + \frac{\partial(\bar{\rho}\tilde{u}_j\tilde{T})}{\partial x_j} = \frac{\partial}{\partial x_j}\left(\frac{\lambda}{c_p}\frac{\partial \tilde{T}}{\partial x_j}\right) - \frac{\partial q_j^{sgs}}{\partial x_j} - \frac{1}{c_p}\sum_{k=1}^{N_s} h_k\overline{\dot{\omega}_k}, \tag{2.2.6}$$

where λ is the thermal conductivity, c_p is the specific heat capacity at constant pressure, h_k is the enthalpy of species k, and q_j^{sgs} is the subgrid-scale heat flux requiring closure.

For reacting flows, the filtered species transport equation is:

$$\frac{\partial(\bar{\rho}\tilde{Y}_k)}{\partial t} + \frac{\partial(\bar{\rho}\tilde{u}_j\tilde{Y}_k)}{\partial x_j} = \frac{\partial}{\partial x_j}\left(\bar{\rho}D_k\frac{\partial\tilde{Y}_k}{\partial x_j}\right) - \frac{\partial J_{k,j}^{sgs}}{\partial x_j} + \overline{\dot{\omega}_k}, \tag{2.2.7}$$

where D_k is the molecular diffusivity of species k, $J_{k,j}^{sgs}$ is the subgrid-scale species flux, and $\overline{\dot{\omega}_k}$ is the filtered chemical source term.

The subgrid-scale fluxes for heat and species are typically closed using gradient-diffusion assumptions:

$$q_j^{sgs} = -\frac{\mu_{sgs}}{\mathrm{Pr}_t}\frac{\partial\tilde{T}}{\partial x_j}, \qquad J_{k,j}^{sgs} = -\frac{\mu_{sgs}}{\mathrm{Sc}_t}\frac{\partial\tilde{Y}_k}{\partial x_j}, \tag{2.2.8}$$

where $\mu_{sgs} = \bar{\rho}\nu_{sgs}$ is the subgrid-scale dynamic viscosity, $\mathrm{Pr}_t \approx 0.9$ is the turbulent Prandtl number, and $\mathrm{Sc}_t \approx 0.7$ is the turbulent Schmidt number.

Alternative closures have been proposed to address the closure of this terms. More recently, machine-learning-based closures using convolutional neural networks or sparse symbolic regression have been explored to learn SGS scalar flux models directly from filtered DNS data, though their stability and generalisability in *a posteriori* LES remain active research topics (LAPEYRE et al., 2019).

The closure of the filtered reaction rate $\overline{\dot{\omega}_k}$ represents the central challenge in LES of reacting flows. Due to the highly nonlinear dependence of reaction rates on temperature and species concentrations, the filtered rate cannot be computed directly from filtered quantities. This closure problem is addressed by combustion models, as discussed in Section 2.3.

2.2.3 Subgrid-Scale Modelling

The subgrid-scale stress tensor τ_{ij}^{sgs} must be modelled to close the filtered momentum equation. The most common approach employs the Boussinesq eddy-viscosity hypothesis (POPE, 2000):

$$\tau_{ij}^{sgs} - \frac{1}{3}\tau_{kk}^{sgs}\delta_{ij} = -2\bar{\rho}\nu_{sgs}\left(\tilde{S}_{ij} - \frac{1}{3}\tilde{S}_{kk}\delta_{ij}\right), \tag{2.2.9}$$

where ν_{sgs} is the subgrid-scale eddy viscosity and $\tilde{S}_{ij} = \frac{1}{2}(\partial\tilde{u}_i/\partial x_j + \partial\tilde{u}_j/\partial x_i)$ is the filtered strain rate tensor. While this linear stress-strain relationship forms the basis of most practical SGS models, direct evaluation against DNS and experimental databases has shown that the

hypothesis is rarely strictly satisfied locally, though it remains effective for capturing mean dissipation behaviour (SCHMITT, F. G., 2007).

2.2.3.1 Smagorinsky Model

The Smagorinsky model (SMAGORINSKY, 1963) computes the eddy viscosity as:

$$\nu_{sgs} = (C_s\Delta)^2|\tilde{S}|, \tag{2.2.10}$$

where $C_s \approx 0.1$–0.2 is the Smagorinsky constant and $|\tilde{S}| = \sqrt{2\tilde{S}_{ij}\tilde{S}_{ij}}$. Despite its simplicity and continued widespread use, the model has well-documented limitations: the constant is not universal and varies across flow configurations, the model is overly dissipative near walls and in laminar regions, and it does not vanish in solid body rotation (MOSER; HAERING; YALLA, 2021). Near-wall behaviour typically requires damping functions such as the van Driest correction (VAN DRIEST, 1956), which reduces the mixing length scale in the viscous sublayer. Recent mathematical analysis has demonstrated that appropriate damping functions can correct the over-dissipation of the Smagorinsky model while maintaining consistency with Kolmogorov phenomenology (PAKZAD, 2017). Comparative assessments across various flow configurations, including wall-bounded jets and atmospheric boundary layers, confirm that the constant-coefficient Smagorinsky model with van Driest damping remains competitive for near-wall predictions when properly calibrated (VISWANATHAN; PATEL, 2020; GHOBRIAL et al., 2025).

2.2.3.2 Dynamic Smagorinsky Model

The Dynamic Smagorinsky model (GERMANO et al., 1991; LILLY, 1992) addresses the limitations of the constant-coefficient Smagorinsky model by computing the model coefficient from the resolved flow field rather than prescribing it a priori.

The procedure employs a test filter $\widehat{\Delta} > \Delta$ (typically $\widehat{\Delta} = 2\Delta$) applied to the resolved field. The Germano identity relates the SGS stresses at the grid and test filter levels through the resolved turbulent stress:

$$L_{ij} = \widehat{\overline{\rho}\tilde{u}_i\tilde{u}_j} - \frac{\widehat{\overline{\rho}\tilde{u}_i}\widehat{\overline{\rho}\tilde{u}_j}}{\widehat{\overline{\rho}}}, \tag{2.2.11}$$

which can be computed directly from the resolved velocity field. Assuming scale-invariance of the model coefficient and applying a least-squares minimisation (LILLY, 1992), the dynamic

coefficient becomes:

$$C_s^2 = \frac{\langle L_{ij} M_{ij} \rangle}{\langle M_{ij} M_{ij} \rangle}, \tag{2.2.12}$$

where M_{ij} involves the difference between strain rate tensors at test and grid filter levels, and $\langle \cdot \rangle$ denotes spatial averaging over homogeneous directions or local smoothing for stability.

The dynamic procedure offers key advantages: the coefficient adapts to local flow conditions, vanishes naturally in laminar regions and near solid walls without requiring ad hoc damping functions, and can assume negative values to represent backscatter. However, the locally computed coefficient exhibits large fluctuations that may cause numerical instability, necessitating averaging or clipping of negative values in practical implementations (PIOMELLI et al., 1991).

Recent literature continues to refine and extend the Dynamic Smagorinsky Model. Rozema et al. (ROZEMA; BAE; VERSTAPPEN, 2022) identified a fundamental singularity in the locally applied dynamic coefficient—arising when no averaging over homogeneous directions is performed—and proposed the dynamic gradient Smagorinsky model (DGSM) as a remedy, replacing the strain-rate tensor with the full velocity gradient tensor to remove the singularity. On the computational side, machine-learning approaches have been explored to reduce the cost of the double-filtering operation inherent to the dynamic procedure (DAI et al., 2023), while in the context of atmospheric modelling, the DSM has recently been implemented in numerical weather prediction frameworks, where it was shown to reduce the excessive dissipation characteristic of the fixed-coefficient model (ZHANG, X.; HUANG; MA, 2024).

2.2.4 Resolution Requirements

The quality of LES depends critically on the relationship between filter width Δ and the turbulent scales present. Pope (POPE, 2004) proposed that well-resolved LES should resolve at least 80% of the turbulent kinetic energy:

$$M = \frac{k_{sgs}}{k_{resolved} + k_{sgs}} < 0.2. \tag{2.2.13}$$

For turbulent combustion, resolution requirements become more stringent. The flame thickness is often smaller than typical LES grid spacing, creating the fundamental challenge that motivates combustion models such as TFM.

2.2.4.1 Implications for TFM

The ratio Δ/δ_L determines the thickening factor required in TFM. For practical LES with grid spacing $\Delta \sim 1$ mm and flame thickness $\delta_L \sim 0.1$ mm, thickening factors $F = 5$–20 may be necessary to place several grid points within the flame.

This relationship has important implications for adaptive mesh refinement:

- The thickening factor can adapt to local resolution, applying stronger thickening in coarse regions and reduced thickening where the mesh is refined;
- Refinement criteria based on flame indicators (temperature gradients, sensor function) can ensure adequate resolution in the reaction zone;
- The effective filter width changes with AMR level, requiring the subgrid model to adjust accordingly.

The TFM formulation presented in Section 3.1.6 incorporates dynamic thickening that naturally accommodates variable mesh resolution, ensuring that the flame remains resolvable regardless of local grid spacing.

2.2.5 Implicit Filtering and Discretisation

An important practical consideration in LES is the relationship between filtering and numerical discretisation. When the balance equations are discretised using finite volume or finite difference methods, the solution is inherently filtered by the computational mesh (SILVEIRA-NETO, 2020). Within each control volume, variables are represented by discrete values (typically cell averages or nodal values), and all spatial variations at scales smaller than the cell size are lost. Similarly, temporal discretisation filters out phenomena with characteristic times smaller than the computational time step.

This discretisation process constitutes an implicit filtering operation. The computational mesh acts as a box filter with filter width equal to the local cell size, $\Delta = (\Delta x \Delta y \Delta z)^{1/3}$. Consequently, in most practical LES implementations, explicit filtering operations are not applied; instead, the grid itself defines the filter, and the cutoff wavenumber is determined by the mesh resolution (POPE, 2000).

This implicit filtering approach has important implications for the formulation and application of subgrid-scale models. First, the subgrid models must be consistent with the effective

filter width imposed by the grid, ensuring that the modelled dissipation scales appropriately with local resolution. Second, in regions of non-uniform mesh, the filter width varies spatially, which can introduce inconsistencies if the SGS model does not account for this variation. Third, for adaptive mesh refinement strategies, as employed in MFSim, the filter width changes dynamically as the mesh is refined or coarsened; this requires subgrid models that appropriately adjust to local resolution without introducing spurious discontinuities or excessive dissipation at refinement interfaces.

2.2.6 Relationship to RANS and DNS

The filtered balance equations represent a general framework that encompasses different turbulence modelling approaches depending on the filter width. This generality can be understood by considering limiting cases (SILVEIRA-NETO, 2020).

When the filter width tends toward the Kolmogorov scales ($\Delta \rightarrow \eta$), the subgrid tensors vanish ($\tau_{ij}^{sgs} \rightarrow 0$), and the filtered equations reduce to the original Navier-Stokes equations. In this limit, all turbulent scales are resolved, corresponding to DNS.

Conversely, when the filter width encompasses all turbulent fluctuations, the filtered equations approach the Reynolds-Averaged equations. In this interpretation, RANS represents the extreme limit of filtering where all frequencies and wavenumbers are filtered out, retaining only the mean behaviour.

LES occupies the intermediate range, where the filter width is larger than the Kolmogorov scale but smaller than the energy-containing scales. This positioning allows LES to resolve the large, energetic, geometry-dependent structures while modelling only the small, more universal subgrid scales.

2.3 LES Combustion Modelling Approaches

The closure of the filtered chemical source term $\overline{\dot{\omega}_k}$, introduce in Equation (2.2.7), constitutes the central challenge in LES of reacting flows. The highly nonlinear relation of reaction rates on the transported scalars of balance equations hinder expressing the filtered reaction rate simply in terms of filtered quantities. This section surveys the principal modelling approaches developed to address this closure problem.

2.3.1 The Closure Problem for Filtered Reaction Rates

The fundamental challenge in turbulent combustion modelling arises from the highly nonlinear dependence of reaction rates on temperature and species concentrations (POINSOT; VEYNANTE, 2005). To illustrate this, consider a single irreversible reaction. The reaction rate follows the Arrhenius law:

$$k(T) = AT^n \exp\left(-\frac{E_a}{RT}\right), \tag{2.3.1}$$

where A is the pre-exponential factor, n is the temperature exponent, E_a is the activation energy, and R is the universal gas constant. The chemical source term for a species depends on this rate constant multiplied by concentration terms:

$$\dot{\omega} \propto k(T) \prod [X_j]^{\nu_j}, \tag{2.3.2}$$

where $[X_j]$ denotes molar concentrations and ν_j are stoichiometric coefficients.

The strong nonlinearity of the exponential term in Equation (2.3.1) means that small temperature fluctuations produce large variations in reaction rate. Consequently, the filtered reaction rate cannot be obtained from filtered quantities alone:

$$\overline{\dot{\omega}_k(T, Y_1, \ldots, Y_{N_s})} \neq \dot{\omega}_k(\bar{T}, \bar{Y}_1, \ldots, \bar{Y}_{N_s}). \tag{2.3.3}$$

This inequality encapsulates the fundamental closure problem in turbulent combustion modelling. The subgrid fluctuations of temperature and composition, which are not resolved in LES, significantly affect the mean reaction rate. Modelling approaches must therefore account for the interaction between subgrid turbulence and chemistry.

The nature of this interaction depends on the combustion regime. In premixed flames, the challenge is capturing the propagation of a thin reaction front through a turbulent flow field. In non-premixed flames, the challenge is modelling the mixing-controlled reaction occurring where fuel and oxidizer meet. Different modelling strategies have emerged for each regime, though unified approaches capable of handling mixed-mode combustion remain an active research area (PITSCH, 2006).

2.3.2 Premixed Combustion Models

In premixed combustion, fuel and oxidizer are mixed prior to reaction, and a self-propagating flame front separates reactants from products. The flame front is typically thin compared to the LES filter width, presenting a resolution challenge that various modelling approaches address differently.

2.3.2.1 Flame Surface Density Models

Flame Surface Density (FSD) models characterize the flame through the surface area of the reaction zone per unit volume, denoted Σ (BOGER et al., 1998; HAWKES; CANT, 2000). The filtered reaction rate is expressed as:

$$\overline{\dot{\omega}} = \rho_u S_L I_0 \Sigma, \tag{2.3.4}$$

where ρ_u is the unburnt mixture density, S_L is the laminar flame speed, and I_0 is a stretch factor accounting for flame stretch effects.

The flame surface density requires modelling, either through algebraic expressions relating Σ to resolved quantities or through a transport equation that accounts for surface production (by turbulent straining), destruction (by curvature and propagation), and convection. The transport equation approach provides more physical detail but introduces additional modelling assumptions for the unclosed terms.

FSD models capture the enhancement of burning rate through increased flame surface area, a key mechanism in turbulent premixed combustion. However, they rely on the flamelet assumption and may require adjustment of model constants for different combustion regimes.

2.3.2.2 G-Equation Model

The G-equation approach represents the flame as a propagating surface tracked by a level-set function $G(\vec{x}, t)$ (WILLIAMS, 1985). The flame surface is defined as the iso-contour $G = G_0$, with $G < G_0$ in the unburnt mixture and $G > G_0$ in the burnt products. The evolution of this surface is governed by:

$$\frac{\partial G}{\partial t} + \vec{u} \cdot \nabla G = S_T |\nabla G|, \tag{2.3.5}$$

where S_T is the turbulent flame speed that must be modelled.

For LES, the filtered G-equation requires closure for the turbulent flame speed at the subgrid level. Models relate S_T to the laminar flame speed S_L and subgrid turbulence characteristics, often through correlations of the form $S_T/S_L = f(u'/S_L)$, where u' represents subgrid velocity fluctuations (PITSCH, 2006).

The G-equation approach offers computational efficiency since it avoids resolving the internal flame structure, requiring only the tracking of a surface. However, it assumes a thin flame regime (flamelet assumption) and provides limited information about flame structure—temperature and species profiles must be reconstructed from flamelet libraries. Extension to detailed chemistry and multi-species transport is not straightforward.

2.3.2.3 Thickened Flame Model

The TFM, also known as the Artificially Thickened Flame (AFT) model, takes a fundamentally different approach by modifying the flame structure itself to make it resolvable on the LES grid (BUTLER; O'ROURKE, 1977; COLIN et al., 2000). Rather than modelling the effects of an unresolved flame, TFM artificially thickens the flame by a factor F while preserving the laminar flame speed, allowing direct resolution of the modified flame structure.

This approach enables the use of detailed chemical mechanisms and provides direct access to species and temperature fields within the flame. An efficiency function compensates for the reduced flame wrinkling caused by thickening. The TFM formulation is detailed in Section 2.4.

2.3.2.4 Flamelet/Progress Variable Method

The Flamelet/Progress Variable (FPV) approach, also known as Flamelet-Generated Manifolds (FGM) when applied with a progress variable, parametrizes the thermochemical state using mixture fraction and a progress variable c that tracks the extent of reaction (PIERCE; MOIN, 2004; OIJEN; GOEY, 2000):

$$\phi = \phi(Z, c). \tag{2.3.6}$$

The progress variable is typically defined based on temperature gradients or as a linear combination of species mass fractions chosen to monotonically increase from unburnt to burnt states. Transport equations are solved for Z and c, and the thermochemical state is retrieved from pre-tabulated manifolds.

The FPV/FGM approach offers computational efficiency through tabulation while retaining the ability to capture partially premixed combustion where both mixture fraction and

reaction progress vary. It has been successfully applied to a wide range of flames, though the assumption that all thermochemical states lie on a low-dimensional manifold may break down in highly strained or extinguishing flames.

2.3.2.5 Transported Probability Density Function Methods

Probability density function methods for turbulent combustion encompass a range of approaches, from presumed PDF methods where the shape of the distribution is assumed a priori and parametrized by its moments to transported PDF methods that solve an evolution equation for the full distribution (POPE, 1985).

Transported PDF methods provide perhaps the most complete treatment of turbulence-chemistry interaction by solving a transport equation for the joint probability density function of velocity and/or scalars (HAWORTH, 2010; VEDOVOTO et al., 2017):

$$\frac{\partial \tilde{f}}{\partial t} + \frac{\partial}{\partial x_j}(\tilde{u}_j \tilde{f}) + \frac{\partial}{\partial \psi_k}(\dot{\omega}_k \tilde{f}) = \text{mixing and transport terms}, \tag{2.3.7}$$

where $\tilde{f}$ is the Favre-filtered PDF and ψ_k represents the sample space for scalars.

A key advantage of transported PDF methods is that the chemical source term appears in closed form, no modelling is required for this term since reactions depend only on the local instantaneous composition, which is known in PDF space. The closure challenge shifts to modelling the mixing term that represents the effect of molecular diffusion in driving the PDF toward a delta function.

An important distinction exists between two major methodologies, the filtered density function (FDF) and the filtered probability density function (FPDF) in the context of LES. The FDF, introduced by Pope (POPE, 1990), describes the local subfilter state of a single realization and can be evaluated from instantaneous fields such as DNS data. The FPDF, in contrast, is a statistical property defined as the ensemble average of the FDF over many realizations given the same resolved field (COLUCCI et al., 1998).

2.3.3 Comparison of Modelling Approaches

Each combustion modelling approach involves trade-offs between physical fidelity, computational cost, and range of applicability. Table 2.2 summarizes key characteristics of the principal approaches discussed in this section.

Table 2.2: Comparison of LES combustion modelling approaches.

Approach	Regime	Chemistry	Cost	Limitations
G-equation	Premixed	Tabulated	Low	Flamelet assumption; no internal flame structure
FSD	Premixed	Reduced/Tab.	Low-Medium	Flamelet assumption; model constants
TFM	Premixed (initially)	Detailed	Medium-High	Efficiency function calibration
FPV/FGM	All regimes	Tabulated	Low-Medium	Manifold assumption
PDF Transport	All regimes	Detailed	Very High	Mixing model; particle count

The TFM occupies a distinctive position among these approaches. Its explicit grid coupling—the thickening factor is directly related to the ratio of grid spacing to flame thickness—provides transparent control over the accuracy-cost trade-off. The compatibility with detailed chemistry enables prediction of minor species important for emissions, while the local formulation integrates naturally with adaptive mesh refinement. These characteristics, combined with the ability to extend the approach to non-premixed regimes through appropriate sensor functions, motivate its selection for implementation in MFSim.

2.4 Thickened Flame Model: State of the Art

2.4.1 Fundamental Principles of Flame Thickening

In premixed combustion, the flame front separating fresh reactants from burnt products is characterized by steep gradients in temperature and species concentrations occurring over a thickness δ_L^0 that scales with molecular transport properties (WILLIAMS, 1985):

$$\delta_L^0 = \frac{D_{th}}{S_L^0}, \tag{2.4.1}$$

where D_{th} is the thermal diffusivity of the unburnt mixture and S_L^0 is the unstretched laminar flame speed. For typical hydrocarbon-air flames at atmospheric conditions, δ_L^0 ranges from 0.1

to 1 mm—far smaller than the grid spacing affordable in LES of practical combustion devices, which typically employs cells of several millimetres (POINSOT; VEYNANTE, 2005).

Accurate resolution of flame structure requires approximately 10–20 grid points across the flame thickness to capture the temperature and species gradients that govern heat release and pollutant formation (COLIN et al., 2000). Meeting this requirement directly would demand grid spacings of order $\Delta x \approx \delta_L^0/10 \sim 10\text{–}100\ \mu$m, rendering full-scale LES of industrial combustors computationally intractable. The Thickened Flame Model addresses this resolution challenge by artificially modifying the flame structure to make it resolvable on coarser grids while preserving essential combustion characteristics.

The theoretical basis for artificial flame thickening derives from the classical scaling relations of laminar premixed flames. From asymptotic analysis of premixed flame structure (PETERS, 2000), the laminar flame speed and thickness depend on the molecular diffusivity D and a characteristic reaction rate $\dot{\omega}$ as:

$$S_L^0 \propto \sqrt{D \cdot \dot{\omega}}, \tag{2.4.2}$$

$$\delta_L^0 \propto \frac{D}{S_L^0} = \sqrt{\frac{D}{\dot{\omega}}}. \tag{2.4.3}$$

An equivalent derivation can be obtained from purely phenomenological arguments, without recourse to asymptotic expansions. Balancing the enthalpy flux conducted ahead of the reaction zone against the volumetric heat release rate, and noting that at steady state the convective and diffusive fluxes must be equal, yields $S_L^0 \sim D/\delta_L^0$ directly (POINSOT; VEYNANTE, 2005). Substituting this relation into the heat-release balance closes the system and recovers Equations. (2.4.2)– (2.4.3). Alternatively, equating the flame transit time $\tau_f \sim \delta_L^0/S_L^0$ with the chemical time scale $\tau_c \sim \dot{\omega}^{-1}$ leads to the same scaling by a simple dimensional argument (WILLIAMS, 1985; VEYNANTE; VERVISCH, 2002). These phenomenological derivations make explicit that S_L^0 and δ_L^0 are set by the competition between molecular diffusion, which tends to broaden the flame, and chemical reaction, which tends to sharpen it—the physical picture that directly motivates the artificial thickening strategy.

These scaling relations reveal that the flame speed and thickness can be independently controlled by appropriately modifying the diffusivity and reaction rate. Specifically, if the

diffusivity is multiplied by a factor F while the reaction rate is divided by the same factor:

$$D \to F \cdot D, \qquad \dot{\omega} \to \frac{\dot{\omega}}{F}, \tag{2.4.4}$$

then the resulting thickened flame exhibits:

$$S_L^F \propto \sqrt{FD \cdot \frac{\dot{\omega}}{F}} = \sqrt{D \cdot \dot{\omega}} \propto S_L^0, \tag{2.4.5}$$

$$\delta_L^F \propto \sqrt{\frac{FD}{\dot{\omega}/F}} = F\sqrt{\frac{D}{\dot{\omega}}} \propto F \cdot \delta_L^0. \tag{2.4.6}$$

This transformation preserves the laminar flame speed—crucial for capturing correct flame propagation—while increasing the flame thickness by factor F, enabling resolution on coarser grids. In practice, the thickening is applied to all diffusion coefficients (thermal conductivity λ and species diffusivities D_k) to maintain consistent transport properties across the thickened flame structure (COLIN et al., 2000; POINSOT; VEYNANTE, 2005).

The thickening factor is typically chosen such that the thickened flame spans a target number of grid points n_c:

$$F = \frac{n_c \Delta x}{\delta_L^0}, \tag{2.4.7}$$

with n_c typically ranging from 5 to 10 for adequate numerical resolution (COLIN et al., 2000; DURAND; POLIFKE, 2007). For non-uniform meshes, the local grid spacing Δx determines a spatially varying thickening factor, a concept that would later evolve into dynamic thickening approaches.

The original TFM formulation applied a constant, global thickening factor throughout the computational domain. While this static approach successfully resolves the flame front, it introduces artificial diffusion in non-reacting regions where accurate mixing prediction is essential—a limitation that motivated subsequent developments in dynamic thickening.

Butler and O'Rourke (BUTLER; O'ROURKE, 1977) provided the foundational mathematical framework for the thickening approach in 1977, demonstrating that the transformation corresponds to a self-similar coordinate dilation normal to the flame front. Their seminal work established the theoretical basis by showing that the transformation can be implemented through modification of diffusion coefficients and reaction source terms without altering the underlying numerical method. Although their original implementation targeted two-dimensional

unsteady reacting flows with simplified chemistry, the core concept of preserving flame speed while increasing thickness has remained central to all subsequent TFM developments.

Colin et al. (COLIN et al., 2000) significantly advanced the approach for LES applications two decades later, providing a rigorous derivation of the thickening transformation within the LES filtering framework. Their work introduced the critical concept of the efficiency function to account for lost subgrid flame wrinkling—a consequence of the thickening that reduces the flame's interaction with small-scale turbulent eddies. The TFM formulation presented by Colin et al. became the foundation for subsequent developments, establishing the model as a practical tool for turbulent combustion simulation.

Following these foundational contributions, Legier et al. (LEGIER; POINSOT; VEYNANTE, 2000) introduced dynamic thickening with flame sensors, ensuring that thickening is applied only in the reaction zone while preserving accurate mixing elsewhere. This development addressed the primary limitation of the static approach and enabled application to more complex configurations involving fuel-air mixing upstream of the flame. The combined contributions of Butler and O'Rourke, Colin et al., and Legier et al. established the theoretical and practical foundations upon which the extensive body of TFM research has subsequently built.

2.4.2 Efficiency Function and Wrinkling Factor Models

2.4.2.1 The Flame Wrinkling Problem

The artificial thickening of the flame front introduces a fundamental modification to flame-turbulence interaction. In turbulent premixed combustion, eddies wrinkle the flame surface, increasing its area and thereby enhancing the overall burning rate. However, turbulent eddies with scales smaller than the thickened flame thickness $F\delta_L^0$ can no longer wrinkle the flame front as they would in the original thin flame. This reduced wrinkling leads to decreased flame surface area and, consequently, an underpredicted overall burning rate (COLIN et al., 2000; CHARLETTE; MENEVEAU; VEYNANTE, 2002a).

Figure 2.4 illustrates this phenomenon conceptually. For the real thin flame (thickness δ_L^0), turbulent eddies across a broad range of scales contribute to flame wrinkling. For the thickened flame (thickness $F\delta_L^0$), only eddies larger than approximately $\beta F\delta_L^0$ (with $\beta \approx 5$) can effectively wrinkle the flame surface (COLIN et al., 2000). The eddies in the range between δ_L^0 and $F\delta_L^0$ that would wrinkle the real flame are effectively filtered out by the thickening operation.

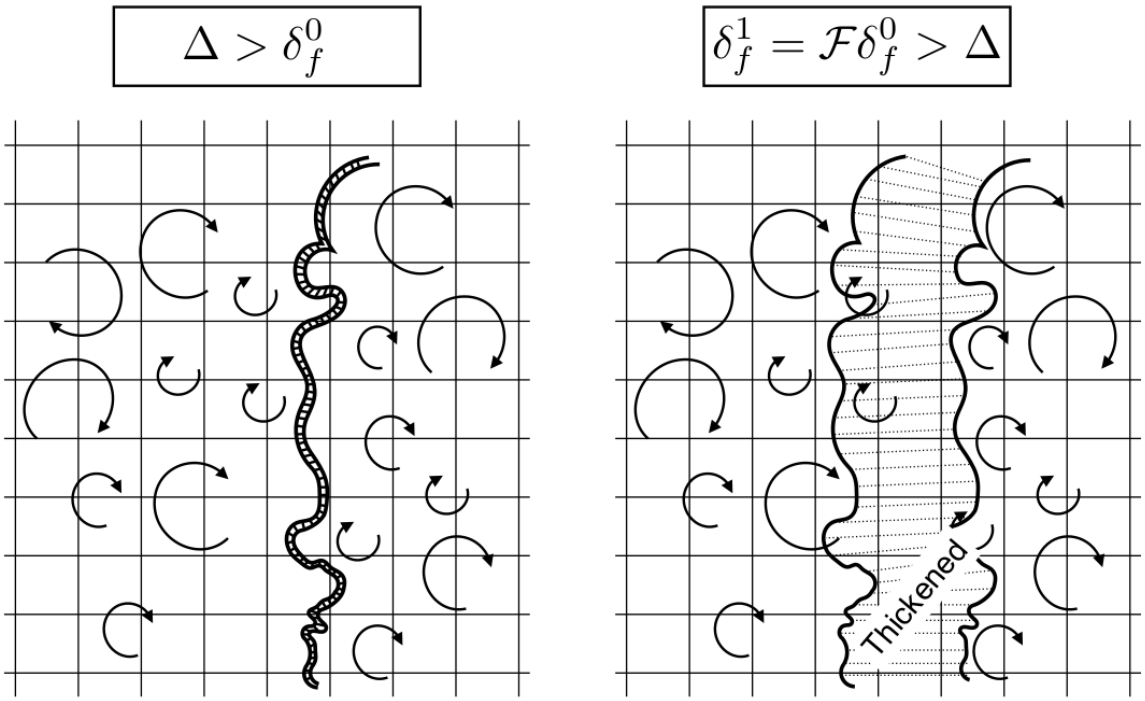

Figure 2.4: Classical TFM wrinkling problem. Only the flame is thickened while turbulence is unaffected by the transformation. Eddies smaller than the thickened flame thickness cannot wrinkle the flame front, reducing the effective flame surface area. Adapted from (RATHORE; NAVARRO-MARTINEZ, 2023).

To compensate for this loss of flame surface, an efficiency function E is introduced that enhances the reaction rate beyond the $1/F$ reduction from thickening:

$$\dot{\omega} \rightarrow \frac{E}{F}\dot{\omega}, \tag{2.4.8}$$

where $E \geq 1$ recovers the subgrid wrinkling contribution. Equivalently, the efficiency function can be understood through the wrinkling factor Ξ, representing the ratio of actual wrinkled flame surface to its projected area:

$$E = \frac{\Xi(\delta_L^0)}{\Xi(F\delta_L^0)}, \tag{2.4.9}$$

where the numerator represents the total wrinkling of the real thin flame and the denominator represents the resolved wrinkling of the thickened flame (COLIN et al., 2000; CHARLETTE; MENEVEAU; VEYNANTE, 2002a). The efficiency function thus bridges the gap between subgrid turbulence-flame interaction in the real and artificially thickened flames.

2.4.2.2 Colin et al. Efficiency Function

Colin et al. (COLIN et al., 2000) developed the first efficiency function based on DNS of flame-vortex interactions and ITNFS (Intermittent Turbulence Net Flame Stretch) theory. The wrinkling factor is modelled as:

$$\Xi = 1 + \alpha\Gamma\left(\frac{\Delta_e}{\delta_L^0}, \frac{u'_{\Delta_e}}{S_L^0}\right)\frac{u'_{\Delta_e}}{S_L^0}, \tag{2.4.10}$$

where $\alpha = (2\ln 2)/(3c_{ms})[\mathrm{Re}_t^{1/2} - 1]$ with $c_{ms} = 0.28$, and:

$$\Gamma = 0.75\exp\left[-\frac{1.2}{(u'_{\Delta_e}/S_L^0)^{0.3}}\right]\left(\frac{\Delta_e}{\delta_L^0}\right)^{2/3}. \tag{2.4.11}$$

This formulation has been widely adopted and validated (DURAND; POLIFKE, 2007; DE; ACHARYA, 2009b; XIA et al., 2023; MULI, 2024; SEHOLE, 2024).

2.4.2.3 Charlette et al. Power-Law Model

Charlette et al. (CHARLETTE; MENEVEAU; VEYNANTE, 2002a) derived a wrinkling model from fractal theory, exploiting that turbulent flame fronts exhibit self-similar characteristics with fractal dimension $D_f \approx 2.1$–2.4 (GOULDIN, 1987). The wrinkling factor is:

$$\Xi = \left(1 + \min\left[\frac{\Delta}{\delta_L^0} - 1, \Gamma_\Delta\frac{u'_\Delta}{S_L^0}\right]\right)^\beta, \tag{2.4.12}$$

where $\beta = D_f - 2 \approx 0.3$–$0.5$, and $\Gamma_\Delta = [(f_u^{-a} + f_\Delta^{-a})^{-b/a} + f_{\mathrm{Re}}^{-b}]^{-1/b}$ blends asymptotic behaviours with $a \approx 0.6$–0.8 and $b = 1.4$. The model ensures $\Xi = 1$ for laminar flames, $\Xi \to (\Delta/\delta_L^0)^\beta$ at fractal saturation, and $\Xi \to 1$ for resolved flames.

2.4.2.4 Dynamic Efficiency Function

Charlette et al. (CHARLETTE; MENEVEAU; VEYNANTE, 2002b) introduced dynamic determination of β using a Germano-like identity requiring total reaction rate preservation between filter and test-filter scales. Wang et al. (WANG; BOILEAU; VEYNANTE, 2011) found that estimating subgrid velocity at both scales led to instabilities and proposed a simplified

formulation based on the saturated limit:

$$\beta = 1 + \frac{\log\left(\left\langle \widehat{W_{\Delta,k}(\tilde{Q})} \right\rangle / \left\langle W_{\gamma\Delta,k}(\hat{\tilde{Q}}) \right\rangle\right)}{\log(\gamma)}, \tag{2.4.13}$$

which eliminates the need for test-filter-scale velocity estimation. Validation on Chen F1–F3 flames showed $\beta \approx 0.2$ for F3 and $\beta \approx 0.4$ for F1/F2, with approximately 20% extra computational cost. Veynante and Moureau (VEYNANTE; MOUREAU, 2015) recommended the saturated Charlette model, while Volpiani et al. (VOLPIANI; SCHMITT, T.; VEYNANTE, 2016) found global β evaluation more stable than local evaluation.

2.4.2.5 Subgrid Velocity Estimation

Both Colin and Charlette formulations require subgrid velocity u'_Δ. The Smagorinsky-based estimate $u'_\Delta = C_s\Delta|\tilde{S}|$ is problematic for reacting flows as it responds to dilatation. Colin et al. (COLIN et al., 2000) proposed a vorticity-based estimate:

$$u'_{\Delta_e} = c_2\Delta x^3 \left|\nabla^2(\nabla \times \tilde{\vec{u}})\right| \left(\frac{\Delta_e}{10\Delta x}\right)^{1/3}, \tag{2.4.14}$$

with $c_2 = 2$, ensuring $u'_\Delta = 0$ for irrotational flows. Durand and Polifke (DURAND; POLIFKE, 2007) developed a finite-volume formulation for unstructured grids. Xia et al. (XIA et al., 2023) compared vorticity-based (Colin) and strain-based (Lilly) models, finding the Colin formulation more robust.

Wang et al. (WANG; BOILEAU; VEYNANTE, 2011) modified the original power-law formulation by Charlette et al. (CHARLETTE; MENEVEAU; VEYNANTE, 2002a) to correct its asymptotic behaviour. They replaced the saturation term (Δ/δ_l^0) with $(F-1)$ to ensure that the efficiency function Ξ correctly tends to unity when the flame is fully resolved ($F \to 1$). The modified efficiency function is expressed as:

$$\Xi = \left(1 + \min\left[F - 1, \Gamma\left(\frac{\Delta}{\delta_l^0}, \frac{u'_\Delta}{s_l^0}, \mathrm{Re}_\Delta\right)\frac{u'_\Delta}{s_l^0}\right]\right)^\beta, \tag{2.4.15}$$

where Γ is the spectral efficiency function accounting for the net straining effect of sub-grid scales. While Wang et al. originally proposed determining the exponent β dynamically, several studies have adopted this structural correction while retaining a static model constant. Specifically, Proch and Kempf and Zhang et al. implemented Equation 2.4.15 with a fixed value of

$\beta = 0.5$. In contrast, Dressler et al. utilized the original Charlette formulation (without the -1 correction) with static $\beta = 0.5$.

A further simplification exploits the saturated limit of the power-law model. In regimes of high turbulence intensity, where the strain term exceeds the geometric limitation ($\Gamma u'_\Delta / s_l^0 \geq F - 1$), the efficiency function becomes independent of the sub-grid velocity fluctuation u'_Δ. In this limit, the minimum operator in Equation 2.4.15 selects the geometric term, reducing the expression to:

$$\Xi \to (1 + F - 1)^\beta = F^\beta. \tag{2.4.16}$$

This saturated regime corresponds to the classical fractal flame surface model, where wrinkling scales purely as a function of the filter width ratio raised to the power $\beta = D_f - 2$, where D_f is the fractal dimension. This "saturated" formulation eliminates the need for sub-grid velocity estimation and has been successfully applied by Volpiani et al. for the Chen F3 flame and explicitly adopted by Lomada et al. ($E = F_{\text{dyn}}^\beta$) for partially-premixed configurations.

Lomada et al. (LOMADA; PFITZNER; KLEIN, 2024) explicitly adopted this saturated formulation with $\beta = 0.5$, referencing the analysis by Veynante and Moureau (VEYNANTE; MOUREAU, 2015). This approach is computationally efficient and avoids the modelling uncertainties associated with u'_Δ estimation. However, the assumption of saturation may not hold in regions of low turbulence intensity or near flammability limits, where the full model would predict $E < F^\beta$.

De and Acharya (DE; ACHARYA, 2009a) proposed a modified Γ function excluding slow eddies ($u' < S_L^0/2$) from wrinkling contribution:

$$\Gamma_n = 0.75 \exp\left[-1.2 \left(\frac{u'_{\Delta_e}}{S_L^0}\right)^{-0.3}\right] \left(\frac{\Delta_e}{\delta_L^F}\right)^{2/3}, \tag{2.4.17}$$

providing improved agreement with DNS for strained configurations.

Table 2.3 compares the efficiency function models.

2.4.3 Dynamic Thickening and Flame Sensors

The original TFM formulation applied a uniform thickening factor throughout the computational domain. While this global thickening approach successfully resolves the flame front, it modifies diffusion not only in the flame region but also in non-reacting zones where accu-

Table 2.3: Comparison of efficiency function models for TFM.

Model	**Theoretical Basis**	**Key Parameters**	**Subgrid Velocity**	**Cost**
Colin et al.	DNS flame-vortex, ITNFS	α, c_{ms}	Required	Moderate
Charlette (original)	Fractal theory, spectral analysis	β, a, b, C_k	Required	Moderate
Wang-modified	Charlette with $F-1$ correction	β (static 0.5)	Required	Moderate
Dynamic β	Germano-like identity	β (computed), γ	Filter scale only	High
Saturated	Fractal saturation limit	β (static 0.5)	Not required	Low
De & Acharya	Modified spectral integration	Γ_n function	Required	Moderate

rate mixing prediction is essential. Near walls, at fuel injection points, and in mixing layers, enhanced diffusion can lead to incorrect species distributions and altered flame stabilisation (DURAND; POLIFKE, 2007).

To address this limitation, Legier et al. (LEGIER; POINSOT; VEYNANTE, 2000) introduced the Dynamically Thickened Flame (DTF) model, which applies thickening only in the vicinity of the flame front. Away from the flame, the transport equations retain their original unthickened form, preserving accurate mixing behaviour. It is important to note that the term "dynamically thickened flame" refers to spatially varying thickening based on a flame sensor, not to the dynamic determination of model parameters in the Germano sense (WANG; BOILEAU; VEYNANTE, 2011).

The DTF model employs a flame sensor $\Omega(\vec{x}, t)$ to identify the flame region. The local thickening factor becomes:

$$F(\vec{x}, t) = 1 + (F_{\max} - 1)\Omega(\vec{x}, t), \tag{2.4.18}$$

where $F_{\max}$ is the maximum thickening factor and Ω varies between 0 (non-reacting regions) and 1 (flame region). This formulation ensures a smooth transition between thickened and unthickened regions, avoiding numerical discontinuities.

The maximum thickening factor $F_{\max}$ is determined by the grid resolution requirement that the thickened flame spans a sufficient number of computational cells for accurate numerical

representation:

$$F_{\max} = \frac{n_c \Delta x}{\delta_L^0}, \tag{2.4.19}$$

where n_c is the target number of grid points across the thickened flame (typically 5–10) and Δx is the local grid spacing (COLIN et al., 2000; DURAND; POLIFKE, 2007). For non-uniform meshes, Δx may be evaluated locally, yielding a spatially varying $F_{\max}$ that adapts to grid refinement. In regions where the flame is already resolved ($\Delta x < \delta_L^0/n_c$), the formulation naturally yields $F_{\max} < 1$, which is typically clipped to unity to avoid artificial flame thinning. Typical values of thickening factors in practical LES range from $F = 4$ to $F = 10$ (HASTI et al., 2016).

The design of the flame sensor Ω is critical to the success of the DTF approach. An effective sensor must reliably detect the flame region across varying operating conditions while avoiding spurious activation in non-reacting zones. Several sensor formulations have been proposed in the literature, each with distinct advantages and limitations.

2.4.3.1 Arrhenius-like and Reaction Rate Sensors

Legier et al. (LEGIER; POINSOT; VEYNANTE, 2000) proposed a sensor based on reduced Arrhenius expression:

$$\Omega = \max\left(0, \tanh\left(\beta' \frac{Y_F^{\nu_F} Y_O^{\nu_O} \exp(-\Gamma T_a/T)}{|\dot{\omega}_F|^{1D}_{\max}}\right)\right), \tag{2.4.20}$$

with $\beta' \approx 500$ and $\Gamma \approx 0.5$ to trigger at temperatures below the reaction zone, ensuring the preheat zone is also thickened. Simpler variants use normalised reaction rate directly (WANG; BOILEAU; VEYNANTE, 2011; XIA et al., 2023; DE TOMASO; RIBER; CUENOT, 2023):

$$\Omega = \tanh\left(\eta \frac{|\dot{\omega}_F|}{|\dot{\omega}_F|^{1D}_{\max}}\right). \tag{2.4.21}$$

Han et al. (HAN et al., 2019) proposed a sensor for high Karlovitz number flames:

$$\Omega = \max\left\{\left(\tanh\left(100 \frac{\dot{\omega}_c}{\dot{\omega}_{c,\max}}\right) - 0.25\right)/0.75,\ 0\right\}, \tag{2.4.22}$$

where $\dot{\omega}_c$ and $\dot{\omega}_{c,\max}$ are the progress variable source term and its maximum, with reference values tabulated as $\dot{\omega}_{c,\max}(Z, c, Y_H)$ for strain-sensitive thickening. Dressler et al. (DRESSLER

et al., 2021) adopted a similar formulation:

$$\Omega = \max\left(0, \tanh\left(5\frac{\dot{\omega}_{PV}}{\max(\dot{\omega}_{PV})} - 1\right)\right). \tag{2.4.23}$$

Xia et al. (XIA et al., 2023) explored sensors based on single reaction step rates, while Zhang et al. (ZHANG, P. et al., 2021) tested sensors based on combined CO, CO_2, and H_2O source terms.

2.4.3.2 Heat Release Rate Sensors

Heat release rate sensors identify the flame based on local heat release normalised by a reference value (ZHANG, P. et al., 2021; SEHOLE, 2024):

$$\Omega = \tanh\left(\eta\frac{\dot{Q}}{\dot{Q}^{1D}_{\max}}\right), \tag{2.4.24}$$

where $\dot{Q}$ is the local heat release rate. Zhang et al. (ZHANG, P. et al., 2021) compared HRR-based sensors against CEMA-based detection, finding that HRR sensors may activate in post-flame equilibrium regions. Sehole (SEHOLE, 2024) implemented an optimised TFM sensor based on heat release rate with smoothing filters for improved numerical stability.

2.4.3.3 Asymmetric Sensors

Rathore and Navarro-Martinez (RATHORE; NAVARRO-MARTINEZ, 2023) developed an asymmetric sensor using a fifth-order polynomial fit of heat release rate conditioned on progress variable:

$$\Omega = f(c) = \sum_{i=0}^{5} a_i c^i, \tag{2.4.25}$$

where coefficients a_i are fitted to bias thickening toward the high-temperature oxidation zone. The authors argue that this is physically motivated, since reactions at higher progress variable involve higher temperatures and greater energy release, requiring more thickening to resolve the strongly nonlinear reaction dynamics. Beyond the physical justification, the asymmetric shape offers two practical advantages. First, many modern combustion codes apply a cut-off temperature below which chemical kinetics are deactivated for efficiency; the near-zero value of Ω on the cold side of the flame ($c \lesssim 0.1$) prevents artificial diffusivity enhancement in the fresh-mixture region where chemistry is numerically disabled, thereby avoiding spurious pre-

ignition. Second, the sensor inherits the low computational overhead of any static, progress-variable-based sensor, since it requires only a single, cheap one-dimensional flame simulation as pre-processing and no runtime evaluation of SGS quantities.

2.4.3.4 Progress Variable Sensors

Durand and Polifke (DURAND; POLIFKE, 2007) proposed a parabolic sensor based on progress variable $c = (T - T_u)/(T_{ad} - T_u)$:

$$\Omega = 16[c(1-c)]^2, \tag{2.4.26}$$

which equals unity at $c = 0.5$ and vanishes in fresh and burnt gases. This formulation has been widely adopted (DE; ACHARYA, 2009b; LOMADA; PFITZNER; KLEIN, 2024). Gaussian variants take the form:

$$\Omega = \exp\left(-\frac{(c-c_0)^2}{2\sigma_c^2}\right), \tag{2.4.27}$$

where c_0 and σ_c control the centre and width. Box sensors use step functions based on progress variable limits (MULI, 2024):

$$\Omega = \begin{cases} 1 & \text{if } c_{\min} < c < c_{\max} \\ 0 & \text{otherwise} \end{cases}. \tag{2.4.28}$$

Muli (MULI, 2024) compared Gaussian, box, and gradient-based sensors within the dynamic ATF framework implemented in OpenFOAM, using a one-dimensional planar flame propagation test as the canonical validation case. The gradient-based sensor, formulated following Proch et al. (Equation (2.4.30)) detects the flame front through the magnitude of the progress variable gradient normalised by its maximum value across the domain. All three sensor formulations were coupled to the progress variable transport equation

$$\frac{\partial \bar{\rho}\,\tilde{b}}{\partial t} + \nabla\cdot\left(\bar{\rho}\,\tilde{U}\,\tilde{b}\right) = \nabla\cdot\left(\mathcal{F}(\Omega)\,E\,D\,\nabla\tilde{b}\right) + \mathcal{F}(\Omega)\,E(\Omega)\,\dot{\omega}_c, \tag{2.4.29}$$

where $b = 1 - c$ is the combustion regress variable, from which the local thickening factor $\mathcal{F} = 1 + (\mathcal{F}_c - 1)\,\Omega$ is computed at each computational cell.

The one-dimensional validation demonstrated that the dynamic implementation successfully confined the thickening to the reaction zone, leaving regions of pure mixing unaffected and thereby preserving the local diffusion transport outside the flame front.

2.4.3.5 Gradient-Based Sensors

Proch and Kempf (PROCH; KEMPF, 2014) developed a sensor based on normalised progress variable gradient:

$$\Omega = \frac{|\nabla Y_c|}{|\nabla Y_c|^{1D}_{\max}}, \tag{2.4.30}$$

with reference values tabulated in FGM as functions of mixture fraction for consistent thickening across varying equivalence ratios in stratified flames (ZHANG, H. et al., 2017).

2.4.3.6 Chemical Species and Radical Sensors

Intermediate radicals naturally confined to the reaction layer can serve as flame markers. Zhang et al. (ZHANG, P. et al., 2021) tested HCO-based sensors for gas turbine combustor simulations,

$$\Omega = \tanh\left(C_1 \frac{[\mathrm{HCO}]}{[\mathrm{HCO}]_{\max}}\right), \tag{2.4.31}$$

where C_1 is a sharpness parameter and $[\mathrm{HCO}]_{\max}$ is the peak value from a reference unstrained laminar flame. The HCO radical correlates with the heat release rate with a coefficient exceeding 90% across a wide range of equivalence ratios and inlet temperatures, and naturally avoids activating in the low-intensity post-flame region under fuel-lean and stoichiometric conditions (ZHANG, P. et al., 2021). This makes it a more selective marker than HRR for detailed chemical mechanisms. Its principal limitation is that it fails to exclude the low-intensity HRR region under fuel-rich conditions, where the HCO profile broadens significantly.

2.4.3.7 CEMA-Based Sensors

Zhang et al. (ZHANG, P. et al., 2021) introduced sensors based on Chemical Explosive Mode Analysis using eigenvalues of the chemical Jacobian $\mathbf{J} = \partial\dot{\omega}_k/\partial Y_j$:

$$\Omega = f(\lambda_{\mathrm{exp}}), \quad \text{where} \quad \lambda_{\mathrm{exp}} = \max(\mathrm{Re}(\lambda_i)), \quad \mathbf{J}\vec{v}_i = \lambda_i \vec{v}_i. \tag{2.4.32}$$

Regions with $\lambda_{\text{exp}} > 0$ exhibit chemical runaway corresponding to active flame zones, distinguishing explosive from non-explosive regions without reference flames. Because the sensor relies solely on local chemical state rather than on a pre-computed reference flame, it is inherently independent of equivalence ratio and fuel type (ZHANG, P. et al., 2021). Validated against lean and rich methane/air flames as well as a hydrogen/air reheat combustor, the CEMA-based sensor consistently identified a more compact thickening region than either the HRR- or HCO-based sensors, avoiding unnecessary thickening in post-flame equilibrium and diffusion-controlled zones under all tested conditions.

2.4.3.8 Geometric Sensors

Rochette et al. (ROCHETTE et al., 2020) proposed a chemistry-independent sensor based on Hessian curvature analysis of a scalar field ϕ (reaction rate or density):

$$\Omega = f(\kappa_{\text{ridge}}), \quad \text{where} \quad \mathbf{H} = \nabla\nabla\phi, \quad \kappa_{\text{ridge}} = \lambda_{\max}(\mathbf{H}), \tag{2.4.33}$$

identifying flame fronts as topological ridges without chemical pre-calibration. This approach can be coupled with a PID controller to dynamically maintain target resolution.

2.4.3.9 Relaxation Sensors

Relaxation sensors transport a fictitious species to create smoothed fields covering diffusion zones. Rochette et al. (ROCHETTE et al., 2020) proposed this approach, later implemented by Marchal (MARCHAL, 2023) following the formulation of Jaravel et al. for compatibility with high-order Spectral Difference methods. The base sensor is first constructed:

$$\Omega_0 = \max\left(0, \min\left(2F_{\max}\frac{|\dot{\omega}_F|}{|\dot{\omega}_F|^{1D}_{\max}} - 1, 1\right)\right), \tag{2.4.34}$$

then extended via transport of a fictitious species ψ:

$$\frac{\partial \rho\psi}{\partial t} + \nabla\cdot(\rho\vec{u}\psi) = \nabla\cdot(\rho D_\psi \nabla\psi) + \rho\frac{\Omega_0 - \psi}{\tau_\psi}, \tag{2.4.35}$$

with the final sensor $\Omega = \psi$.

Table 2.4 compares sensor formulations.

Table 2.4: Comparison of flame sensor formulations for dynamic thickening.

Sensor Type	**Basis**	**Key Characteristics**
Arrhenius/Reaction rate	$Y_F^{\nu_F} Y_O^{\nu_O} \exp(-T_a/T)$ or $\lvert\dot{\omega}\rvert$	Chemistry-aware; requires reference; may miss preheat
Heat release rate	Local $\dot{Q}$	Simple; may activate in equilibrium zones
Asymmetric	HRR polynomial fit on c	Biased toward oxidation zone
Progress variable	$c(1-c)$ parabolic, Gaussian, or box	Simple; requires temperature bounds
Gradient-based	$\lvert\nabla Y_c\rvert/\lvert\nabla Y_c\rvert^{1D}_{\max}$	Handles stratification via tabulation
Chemical species	Radical concentration (HCO, H)	Confined to reaction layer; mechanism-dependent
CEMA-based	Jacobian eigenvalues $\lambda_{\exp}$	No reference needed; higher cost
Geometric	Hessian curvature κ_{ridge}	Chemistry-independent; self-adapting
Relaxation	Transported species ψ	Smooth field; covers diffusion zones

2.4.4 Stretch and Curvature Effects

A fundamental limitation of the classical TFM arises when flames are subjected to stretch. For weakly stretched flames, the consumption speed deviates from the unstretched laminar value according to the linear Markstein relation $s_c = S_L^0 - \mathcal{L}_c\kappa$, where $\mathcal{L}_c$ is the consumption-based Markstein length and κ is the stretch rate (POINSOT; VEYNANTE, 2005; PETERS, 2000). As demonstrated by Detomaso et al. (DE TOMASO; RIBER; CUENOT, 2023), the thickening transformation amplifies the flame's response to stretch, with the Markstein length scaling as $\mathcal{L}_c^F = F\mathcal{L}_c$. Consequently, a thickened flame subjected to stretch κ behaves as if the original thin flame experienced stretch $F\kappa$, leading to underestimation of consumption speed at high strain rates and premature extinction in highly strained regions.

Quillatre (QUILLATRE, 2014) developed the TF-adapt model to mitigate this effect by modifying the species Lewis numbers according to $\text{Le}^F = 1 + (\text{Le}_0 - 1)/F$, which counteracts the Markstein length amplification. This approach recovers the correct slope $\partial s_c/\partial\kappa$ for small stretch rates but relies on asymptotic theory valid only for weak stretch.

Detomaso et al. (DE TOMASO; RIBER; CUENOT, 2023) proposed the Stretched-Thickened Flame (S-TF) model, introducing separate scaling factors for thermal diffusivity (F_{th}), species diffusivities (F_{sp}), and reaction rate (F_r). These factors are determined by imposing preser-

vation of unstretched flame speed, target thermal thickness $F\delta_L^0$, and correct stretched flame speed at a specified target stretch rate κ^*. The S-TF model accurately reproduces consumption speed variation with strain rate up to extinction for counterflow flames and correctly captures curvature-dependent propagation speed for expanding flames, without requiring local stretch evaluation during simulation.

The modified TFM (MTFM) approach of Rathore and Navarro-Martinez (RATHORE; NAVARRO-MARTINEZ, 2023) addresses stretch effects differently by applying thickening to all transport equations including momentum, preserving the Damköhler number and reducing the need for efficiency function corrections in flame-vortex interactions.

2.4.5 Extension to Non-Premixed Combustion

The original TFM was derived for premixed flames exploiting scaling relations $S_L^0 \propto \sqrt{D\dot{\omega}}$ and $\delta_L^0 \propto \sqrt{D/\dot{\omega}}$. Non-premixed flames exhibit different physics: for high-Damköhler diffusion flames, Cuenot et al. (CUENOT; SHUM-KIVAN; BLANCHARD, 2022) showed that consumption rate and thickness scale as $\dot{\Omega} \propto \sqrt{aD}$ and $\delta_f \propto \sqrt{D/a}$, where a is the strain rate. The chemical source term does not appear—these flames are mixing-controlled. Applying premixed thickening ($D \to FD$, $\dot{\omega} \to \dot{\omega}/F$) to diffusion flames increases thickness by $\sqrt{F}$ rather than F and modifies consumption rate by $\sqrt{F}$.

For proper diffusion flame thickening, Cuenot et al. (CUENOT; SHUM-KIVAN; BLANCHARD, 2022) proposed $D \to FD$ and $a \to a/F$, which yields $\delta_f^F = F\delta_f$ and $\dot{\Omega}^F = \dot{\Omega}$. However, modifying strain rate in governing equations is not straightforward, so practical implementations often apply premixed thickening even to non-premixed regions, accepting some error.

For non-premixed combustion, the flame sensor is reformulated using mixture fraction. A Gaussian sensor centred on stoichiometry is commonly employed (LEGIER; POINSOT; VEYNANTE, 2000; MULI, 2024):

$$\Omega_{\text{diff}} = \exp\left(-\frac{(Z - Z_{st})^2}{2\sigma_Z^2}\right), \tag{2.4.36}$$

where σ_Z controls sensor width (typically 0.01–0.02 for methane-air with $Z_{st} \approx 0.055$). Sehole (SEHOLE, 2024) and Muli (MULI, 2024) implemented combined sensors in OpenFOAM using logical combinations of progress variable and mixture fraction sensors.

2.4.6 Advanced Implementations, Coupling Strategies, and Validation

The TFM framework has been extended to address complex combustion configurations through coupling with tabulated chemistry, alternative thickening paradigms, multi-physics interactions, and high-order numerical methods. This section reviews these developments alongside the validation cases that established their applicability.

2.4.6.1 Tabulated Chemistry Coupling

The TF-FGM approach couples TFM with Flamelet-Generated Manifolds, applying thickening and efficiency modifications to the progress variable equation while retrieving thermochemical state from pre-tabulated manifolds. Proch and Kempf (PROCH; KEMPF, 2014) applied TFM-FGM to the Cambridge stratified flames (SwB1, SwB5, SwB9), tabulating sensor reference values as functions of mixture fraction for consistent thickening across varying equivalence ratios. Zhang et al. (ZHANG, H. et al., 2017) compared DTF-FGM against PPDF-FGM for Cambridge SwB1/SwB2, emphasising subgrid variance importance for CO prediction. Auzillon et al. (AUZILLON et al., 2011) compared TFM against F-TACLES for laminar and pulsating Bunsen flames, finding that TFM spreads thermal thickness more than reaction thickness, affecting flame dynamics under strong unsteady forcing.

2.4.6.2 Modified TFM

Rathore and Navarro-Martinez (RATHORE; NAVARRO-MARTINEZ, 2023) proposed the MTFM model, applying thickening to all conservation equations including momentum by scaling the viscous stress tensor by F. This preserves the Damköhler number and flame-vortex interaction characteristics, potentially eliminating the need for efficiency functions. Validation against DNS of flame-vortex interactions and the Yuen and Gülder M14 Bunsen flame showed improved capture of vortex-induced wrinkling, pocket formation, and curvature statistics compared to classical TFM.

2.4.6.3 Partially-Premixed Flames

Lomada et al. (LOMADA; PFITZNER; KLEIN, 2024) compared TFM against Flame Surface Density (FSD) models for the turbulent partially-premixed Sydney piloted flame (FJ200-5GP-

Lr75-57), finding that FSD yields better agreement with experimental temperature and species distributions, whereas TFM with a global two-step mechanism tends to overestimate them. Volpiani et al. (VOLPIANI; SCHMITT, T.; VEYNANTE, 2016) performed a posteriori tests of global and local dynamic formulations for the flame wrinkling factor on a turbulent jet flame, showing good agreement without manual parameter tuning.

2.4.6.4 Spray Combustion

When droplets traverse thickened flames, they experience artificially extended high-temperature regions affecting evaporation rate and heat transfer. Dressler et al. (DRESSLER et al., 2021) developed projection and refraction correction methods, validating against the Sydney ethanol spray flame (EtF6) with significant improvement in droplet diameter and evaporation predictions.

2.4.6.5 Adaptive Mesh Refinement

Hasti et al. (HASTI et al., 2016) coupled TFM with AMR for the Volvo bluff-body flame ($\phi = 0.62$) using zonal thickening ($F = 3$ in the recirculation zone, $F = 7$ downstream), demonstrating that AMR enables efficient simulations while maintaining accuracy. Rochette et al. (ROCHETTE et al., 2020) proposed coupling their geometric sensor with a PID controller to dynamically maintain target grid points across the flame.

2.4.6.6 High-Order Methods and Open-Source Implementations

Marchal (MARCHAL, 2023) implemented TFM within a Spectral Difference method, adopting the relaxation sensor of Rochette et al. (ROCHETTE et al., 2020) for smooth fields compatible with high-order discretisation. Validation against AVBP solutions for the Volvo bluff-body and Cambridge burner (SwBc, SwB1) demonstrated comparable accuracy with fewer degrees of freedom. Open-source implementations in OpenFOAM have been documented by Muli (MULI, 2024) and Sehole (SEHOLE, 2024), providing reference implementations for premixed and non-premixed combustion modes.

2.4.6.7 Canonical and Industrial Validation Cases

The foundational validation of TFM was established through one-dimensional flames: Butler and O'Rourke (BUTLER; O'ROURKE, 1977) validated the original method, Colin et al.

(COLIN et al., 2000) derived the efficiency function from DNS of flame-vortex interactions, and Legier et al. (LEGIER; POINSOT; VEYNANTE, 2000) validated DTF for laminar propane/air flames. Detomaso et al. (DE TOMASO; RIBER; CUENOT, 2023) validated the S-TF model for counterflow and expanding flames under varying strain.

The Chen F1, F2, F3 piloted Bunsen flames (Re $\approx$ 52,000, 40,000, 24,000) provide canonical turbulent validation. De and Acharya (DE; ACHARYA, 2009b) compared TFM variants against PDF and G-equation models for F3. Wang et al. (WANG; BOILEAU; VEYNANTE, 2011) validated dynamic TFM on all three flames, showing $\beta \approx 0.2$ for F3 and $\beta \approx 0.4$ for F1/F2. Xia et al. (XIA et al., 2023) compared Colin versus Charlette efficiency functions.

For bluff-body flames, Durand and Polifke (DURAND; POLIFKE, 2007) validated TFM in Fluent for the Volvo configuration ($\phi = 0.65$). For gas turbine applications, Zhang et al. (ZHANG, P. et al., 2021) validated LES/TFM for the DLR Flame A dual swirl combustor, also testing sensor robustness under autoignition conditions.

Table 2.5 summarises the validation database.

Table 2.5: Summary of TFM validation cases in the literature.

Configuration	**Key References**	**Validated Quantities**	**Model Variants**
1D laminar	Butler (1977), Colin (2000), Legier (2000), Detomaso (2023), Muli (2024)	Flame speed, structure, stretch	Static, DTF, S-TF
Bunsen	De (2009), Wang (2011), Xia (2023), Rathore (2023), Muli (2024)	Velocity, TKE, T, species, curvature	Colin, Charlette, MTFM
Bluff-body	Durand (2007), Hasti (2018), Marchal (2023)	Velocity, T, CO	DTF, TFM-FGM, AMR
Swirl/stratified	Proch (2014), Zhang H. (2017), Marchal (2023)	Velocity, T, ϕ, CO	TFM-FGM, DTF-FGM
Partially-premixed	Lomada (2024), Volpiani (2016)	T, species, flame wrinkling	TFM, FSD comparison
Spray	Dressler (2021)	Droplet properties, T, evaporation	TFM-FGM with corrections
Gas turbine	Zhang P. (2021)	Velocity, T, O_2, CO	DTF detailed chemistry

MATHEMATICAL MODELLING AND NUMERICAL METHODS

This chapter presents the mathematical formulation and numerical methods employed for the simulation of turbulent reacting flows using the TFM in MFSim. The balance equations for multi-species reacting flows are first introduced, followed by the detailed TFM formulation for both premixed and non-premixed combustion. The numerical methods implemented in MFSim are then described, including spatial and temporal discretization, pressure-velocity coupling, and the specific implementation details of the TFM module.

3.1 Reacting Flows Mathematical Modelling

The simulation of turbulent reacting flows requires solving the balance equations for mass, momentum, energy, and chemical species. These equations, collectively known as the multi-species reacting Navier-Stokes equations, form the foundation for computational combustion (POINSOT; VEYNANTE, 2005; WILLIAMS, 1985).

3.1.1 Balance Equations

The mass balance equation expresses the principle that mass is neither created nor destroyed during combustion—chemical reactions merely transform species without altering total mass:

$$\frac{\partial \rho}{\partial t} + \frac{\partial (\rho u_j)}{\partial x_j} = 0, \tag{3.1.1}$$

where ρ is the mixture density and u_j represents the velocity components.

The momentum equation for reacting flows retains the same form as for non-reacting flows, though combustion significantly affects the flow field through density variations and

temperature-dependent viscosity:

$$\frac{\partial(\rho u_i)}{\partial t} + \frac{\partial(\rho u_i u_j)}{\partial x_j} = -\frac{\partial p}{\partial x_i} + \frac{\partial \tau_{ij}}{\partial x_j} + \rho g_i, \tag{3.1.2}$$

where p is the thermodynamic pressure, g_i represents body forces, and τ_{ij} is the viscous stress tensor. For a Newtonian fluid under Stokes' hypothesis, the viscous stress tensor is given by:

$$\tau_{ij} = \mu \left(\frac{\partial u_i}{\partial x_j} + \frac{\partial u_j}{\partial x_i} - \frac{2}{3} \frac{\partial u_k}{\partial x_k} \delta_{ij} \right), \tag{3.1.3}$$

where μ is the dynamic viscosity and δ_{ij} is the Kronecker delta. Although no explicit reaction terms appear in Equation (3.1.2), combustion strongly influences the flow through pressure increase from heat release and density decrease from gas expansion, which can change the local Reynolds number by an order of magnitude across the flame front (POINSOT; VEYNANTE, 2005).

The energy equation for reacting flows can be written in several forms. Using temperature T as the transported variable, the energy balance equation reads:

$$\frac{\partial(\rho T)}{\partial t} + \frac{\partial(\rho u_j T)}{\partial x_j} = \frac{\partial}{\partial x_j} \left(\rho D_{th} \frac{\partial T}{\partial x_j} \right) + \frac{Q}{c_p} \dot{\omega}_F, \tag{3.1.4}$$

where $D_{th} = \lambda/(\rho c_p)$ is the thermal diffusivity, c_p is the mixture specific heat at constant pressure, Q is the heat of reaction, and $\dot{\omega}_F$ is the fuel reaction rate. The mixture specific heat capacity is defined as the mass-weighted average of the species heat capacities:

$$c_p = \sum_{k=1}^{N_s} Y_k c_{p,k}(T), \tag{3.1.5}$$

For a single-step global reaction of the form:

$$\nu'_F \mathcal{F} + \nu'_O \mathcal{O} \longrightarrow \nu''_P \mathcal{P}, \tag{3.1.6}$$

the fuel reaction rate is expressed using the Arrhenius law (Equation (3.1.18)). The heat of reaction Q represents the energy released per unit mass of fuel consumed.

The composition of a reacting mixture is described by the mass fractions Y_k, defined as the ratio of the mass of species k to the total mixture mass:

$$Y_k = \frac{m_k}{m} = \frac{\rho_k}{\rho}, \tag{3.1.7}$$

where ρ_k is the partial density of species k. By definition, the mass fractions satisfy the constraint $\sum_{k=1}^{N_s} Y_k = 1$. Alternatively, composition may be expressed through mole fractions X_k, related to mass fractions by:

$$X_k = \frac{Y_k / W_k}{\sum_{j=1}^{N_s} Y_j / W_j} = Y_k \frac{\bar{W}}{W_k}, \tag{3.1.8}$$

where W_k is the molecular weight of species k and $\bar{W} = \left(\sum_{k=1}^{N_s} Y_k / W_k\right)^{-1}$ is the mean molecular weight of the mixture.

The balance of mass for individual species k introduces the chemical source term that distinguishes reacting from non-reacting flows:

$$\frac{\partial(\rho Y_k)}{\partial t} + \frac{\partial(\rho u_j Y_k)}{\partial x_j} = -\frac{\partial J_{k,j}}{\partial x_j} + \dot{\omega}_k \qquad \text{for } k = 1, \ldots, N_s, \tag{3.1.9}$$

where Y_k is the mass fraction of species k, $J_{k,j}$ is the diffusive flux of species k in direction j, $\dot{\omega}_k$ is the chemical production rate of species k, and N_s is the total number of species in the mixture.

The rigorous description of molecular diffusion in multicomponent gas mixtures requires solving the Stefan-Maxwell equations, which account for binary interactions between all species pairs (HIRSCHFELDER; CURTISS; BIRD, 1964). However, this multicomponent formulation is computationally expensive, requiring matrix inversions at each point and time step. A simplified mixture-averaged approach approximates the diffusion velocity of each species as driven by its own concentration gradient, with an effective diffusion coefficient D_k representing diffusion of species k into the remaining mixture (BIRD; STEWART; LIGHTFOOT, 2002):

$$D_k = \frac{1 - Y_k}{\sum_{j \neq k} X_j / \mathcal{D}_{kj}}, \tag{3.1.10}$$

where $\mathcal{D}_{kj}$ are the binary diffusion coefficients. This approximation is accurate when one species dominates the mixture (as with nitrogen in air) or when all binary diffusivities are

similar. For most combustion applications, the mixture-averaged model provides sufficient accuracy at significantly reduced cost (COFFEE; HEIMERL, 1981).

The diffusive flux is then modelled using Fick's law with an effective diffusion coefficient:

$$J_{k,j} = -\rho D_k \frac{\partial Y_k}{\partial x_j} + \rho Y_k V_j^c, \tag{3.1.11}$$

where D_k is the mass diffusion coefficient of species k into the mixture and V_j^c is a correction velocity ensuring mass balance:

$$V_j^c = \sum_{k=1}^{N_s} D_k \frac{\partial Y_k}{\partial x_j}, \tag{3.1.12}$$

This correction is necessary because Fick's law applied independently to each species does not automatically satisfy the constraint $\sum_{k=1}^{N_s} Y_k = 1$ and $\sum_{k=1}^{N_s} J_{k,j} = 0$.

The summation of Equation (3.1.9) over all species must recover the total mass balance (Equation (3.1.1)), which requires:

$$\sum_{k=1}^{N_s} \dot{\omega}_k = 0. \tag{3.1.13}$$

This constraint reflects the fact that chemical reactions conserve total mass while redistributing it among species.

3.1.2 Equation of State

The system of equations is closed by the ideal gas equation of state:

$$p = \rho \frac{R_u}{W} T = \rho R_u T \sum_{k=1}^{N_s} \frac{Y_k}{W_k}, \tag{3.1.14}$$

where $R_u = 8.314\,\mathrm{J/(mol{\cdot}K)}$ is the universal gas constant, W_k is the molecular weight of species k, and W is the mean molecular weight of the mixture:

$$\frac{1}{W} = \sum_{k=1}^{N_s} \frac{Y_k}{W_k}. \tag{3.1.15}$$

3.1.3 Chemical Kinetics

This section presents the complete formulation for chemical source terms as implemented in MFSim. While Section 2.3.1 introduced the conceptual basis for the closure problem using

simplified expressions, the full treatment requires accounting for multiple reactions, reversibility, and proper indexing over species and reactions.

The chemical source term $\dot{\omega}_k$ for species k is computed by summing contributions from all N_r elementary reactions in the chemical mechanism:

$$\dot{\omega}_k = W_k \sum_{r=1}^{N_r} \left(\nu''_{k,r} - \nu'_{k,r} \right) \mathcal{Q}_r, \tag{3.1.16}$$

where W_k is the molecular weight of species k, $\nu'_{k,r}$ and $\nu''_{k,r}$ are the stoichiometric coefficients of species k as reactant and product in reaction r, respectively, and $\mathcal{Q}_r$ is the rate of progress of reaction r.

For a reversible reaction, the rate of progress accounts for both forward and backward directions:

$$\mathcal{Q}_r = k_{f,r} \prod_{j=1}^{N_s} [X_j]^{\nu'_{j,r}} - k_{b,r} \prod_{j=1}^{N_s} [X_j]^{\nu''_{j,r}}, \tag{3.1.17}$$

where $[X_j] = \rho Y_j / W_j$ is the molar concentration of species j, and $k_{f,r}$ and $k_{b,r}$ are the forward and backward rate constants.

The forward rate constant follows the modified Arrhenius law:

$$k_{f,r} = A_r T^{n_r} \exp\left(-\frac{E_{a,r}}{R_u T} \right), \tag{3.1.18}$$

where A_r is the pre-exponential factor, n_r is the temperature exponent, and $E_{a,r}$ is the activation energy for reaction r. The universal gas constant is denoted $R_u = 8.314$ J/(mol·K). The backward rate constant is related to the forward rate through the equilibrium constant:

$$k_{b,r} = \frac{k_{f,r}}{K_{c,r}}, \tag{3.1.19}$$

where $K_{c,r}$ is the equilibrium constant in concentration units, computed from thermodynamic data using standard-state Gibbs free energies. This relation follows from the principle of detailed balance and is valid provided the forward and reverse rate parameters are thermodynamically consistent. In practice, however, there are situations in which Eq. (3.1.19) does not hold exactly. First, reactions designated as irreversible set $k_{b,r} = 0$ regardless of $K_{c,r}$, as the reverse pathway is assumed negligible under the conditions of interest. Second, for pressure-dependent (fall-off) reactions described by Troe formulations (TROE, 1974), the effective rate

constant depends on both pressure and bath-gas composition; while the detailed balance relation remains valid at the high- and low-pressure limits individually, inconsistencies can arise if the fall-off parameters for the forward and reverse channels are fitted independently. Third, certain kinetic mechanisms supply explicit Arrhenius expressions for both $k_{f,r}$ and $k_{b,r}$ fitted directly to experimental data (SMITH et al., 1999); in such cases the ratio $k_{f,r}/k_{b,r}$ need not coincide with the thermodynamically derived $K_{c,r}$, introducing a deliberate inconsistency that is accepted in exchange for improved agreement with measurements over a specific temperature range.

The parameters A_r, n_r, and $E_{a,r}$ for each reaction are obtained from validated chemical mechanisms. In this work, chemistry calculations are performed through the Cantera library (GOODWIN; MOFFAT; SPETH, 2009), which provides efficient evaluation of reaction rates, thermodynamic properties, and transport coefficients from standard mechanism files in Chemkin format.

3.1.4 Transport Properties

The transport properties are computed using the mixture-averaged model implemented in Cantera (GOODWIN; MOFFAT; SPETH, 2009), based on kinetic theory as described by Kee et al. (KEE; COLTRIN; GLARBORG, 2003). This model provides the dynamic viscosity μ, thermal conductivity λ, and species diffusion coefficients D_k as functions of temperature and composition.

The mixture viscosity is computed using the Wilke mixture rule (WILKE, 1950):

$$\mu = \sum_{k=1}^{N_s} \frac{X_k \mu_k}{\sum_{j=1}^{N_s} X_j \Phi_{k,j}}, \tag{3.1.20}$$

where X_k is the mole fraction of species k, μ_k is the pure species viscosity, and $\Phi_{k,j}$ is the interaction parameter given by:

$$\Phi_{k,j} = \frac{1}{\sqrt{8}} \left(1 + \frac{W_k}{W_j}\right)^{-1/2} \left[1 + \left(\frac{\mu_k}{\mu_j}\right)^{1/2} \left(\frac{W_j}{W_k}\right)^{1/4}\right]^2, \tag{3.1.21}$$

where W_k and W_j are the molecular weights of species k and j, respectively.

The mixture thermal conductivity is computed from the following averaging rule:

$$\lambda = \frac{1}{2}\left(\sum_{k=1}^{N_s} X_k \lambda_k + \frac{1}{\sum_{k=1}^{N_s} X_k/\lambda_k}\right), \tag{3.1.22}$$

where λ_k is the thermal conductivity of pure species k.

The mixture-averaged diffusion coefficient for species k is defined as stated in Equation (3.1.10).

3.1.5 Filtered Balance Equations

The Favre-filtered balance equations for continuity (Equation 2.2.3), momentum (Equation 2.2.4), energy (Equation 2.2.6), and species transport (2.2.7), presented in Section 2.2.2, form the basis of the LES framework employed in this work. The subgrid-scale stress tensor τ_{ij}^{sgs} is closed through an eddy viscosity model as described in Section 2.2.3, while subgrid scalar fluxes are modelled using gradient-diffusion assumptions.

The simulations presented in this work employ the Dynamic Smagorinsky model with explicit LES filtering, as implemented in MFSim. The explicit filtering approach applies the test filter $\widehat{\Delta}$ directly to the resolved field, rather than relying on implicit grid filtering, providing improved scale separation and more consistent evaluation of the dynamic coefficient (LUND, 2003). The model coefficient is computed according to Equation 2.2.12 with local averaging for numerical stability.

3.1.6 TFM Modified Balance Equations

Finally, the TFM modifies the filtered species and energy balance equations through the thickening factor F and efficiency function E. The complete forms, incorporating both molecular and turbulent transport, are:

$$\frac{\partial(\bar{\rho}\tilde{Y}_k)}{\partial t} + \frac{\partial(\bar{\rho}\tilde{u}_j\tilde{Y}_k)}{\partial x_j} = \frac{\partial}{\partial x_j}\left[\left(EF\bar{\rho}D_k + \frac{\mu_t}{\mathrm{Sc}_t}\right)\frac{\partial \tilde{Y}_k}{\partial x_j}\right] + \frac{E}{F}\dot{\omega}_k \tag{3.1.23}$$

$$\frac{\partial(\bar{\rho}\tilde{T})}{\partial t} + \frac{\partial(\bar{\rho}\tilde{u}_j\tilde{T})}{\partial x_j} = \frac{\partial}{\partial x_j}\left[\left(EF\frac{\lambda}{c_p} + \frac{\mu_t}{\mathrm{Pr}_t}\right)\frac{\partial \tilde{T}}{\partial x_j}\right] - \frac{E}{F}\frac{1}{c_p}\sum_{k=1}^{N_s} h_k\dot{\omega}_k \tag{3.1.24}$$

The turbulent transport terms (μ_t/Sc_t and μ_t/Pr_t) remain unmodified, as they represent physical subgrid-scale mixing that should not be altered by the artificial thickening procedure.

3.2 Numerical Methods in MFSim

MFSim is a computational fluid dynamics framework for multi-physics simulations, including combustion, multiphase flows, and fluid-structure interaction. This section describes the numerical methods implemented in MFSim that are relevant to turbulent combustion simulations with the TFM.

3.2.1 MFSim: History and Development

MFSim is a multi-physics simulation software that has been continuously developed since 2007 by the Fluid Mechanics Laboratory (MFLab) of the Graduate Program in Mechanical Engineering at the Federal University of Uberlândia (UFU), in collaboration with Petrobras (VILLAR, 2007). Since its inception, the platform has evolved through successive contributions from the research group, expanding its capabilities to address a diverse range of multi-physics phenomena, summarised in Table 3.1 . Its architecture is based on a modular philosophy, allowing different physical phenomena to be represented independently through specialised modules, each containing dedicated computational numerical methods that ensure flexibility in modelling complex systems. Within this broad context, the development of reactive flow simulation capabilities has followed a systematic progression through four doctoral theses, each building upon its predecessors while introducing new methodologies and extending the range of applicable combustion regimes.

The foundational development of MFSim's reactive flow capabilities was established in the doctoral thesis of (VEDOVOTO, 2011). This work introduced a low Mach number variable-density solver employing a fully implicit predictor-corrector scheme, specifically designed for turbulent premixed combustion. The methodology adopted a hybrid Large Eddy Simulation/Probability Density Function (LES/PDF) framework, where the filtered transport equations were solved using LES while the subgrid-scale turbulence-chemistry interactions were captured through a transported PDF approach for the progress variable. Classical and dynamic Smagorinsky models were implemented for subgrid-scale stress closure, alongside three distinct turbulent inflow boundary condition methodologies to enable realistic turbulent inlet specifications. The stochastic differential equations governing the PDF evolution were solved using Monte Carlo methods. Extensive verification was performed using the Method of Man-

Table 3.1: MFSim code applications and references (adapted from (OLIVEIRA, 2025)).

Phenomenon/Application	**Reference(s)**
Gas-solid flows	(PIVELLO et al., 2014)
Turbulent flows	(DAMASCENO; VEDOVOTO; SILVEIRA-NETO, 2015)
Hybrid turbulence methods	(MELO, 2017)
Gas-liquid flows	(BARBI et al., 2018)
Reactive flows	(DAMASCENO; SANTOS; VEDOVOTO, 2018)
Turbulence modelling approaches	(ELIAS, 2018)
Gas-solid flows (extended)	(SANTOS, 2019)
Gas-liquid flows (extended)	(PINHEIRO et al., 2021)
Reactive flows (compressible)	(CASTRO et al., 2021)
Multiphase flows	(SOUZA et al., 2022)
Wind turbine aerodynamics	(MARTINI, 2021; STIVAL et al., 2022)
Flow-induced corrosion	(MOTA, 2023)
Forensic fluid mechanics	(VASCONCELLOS, 2024)
Fluid-structure interaction	(OLIVEIRA, 2025)
Gas-liquid flows (extended)	(NONAKA, 2025)

ufactured Solutions (MMS), with validation conducted on two-dimensional premixed flames in channel flows and turbulent jet configurations.

Building upon this foundation, the work of (DAMASCENO, 2018) significantly extended MFSim's reactive flow capabilities by introducing block-structured Adaptive Mesh Refinement (AMR) specifically tailored for reactive flow simulations. This contribution addressed a critical limitation of the earlier implementation by enabling dynamic concentration of computational resources in regions of chemical activity, flame fronts, and steep gradients. The numerical framework incorporated high-resolution Total Variation Diminishing (TVD) schemes, including CUBISTA and WENO formulations, for accurate advection treatment with minimal numerical diffusion. The subgrid-scale turbulence model employed a dynamic Smagorinsky formulation with Random Flow Generation (RFG) for synthetic turbulent inlet conditions. A significant advance was the integration of the Cantera library for thermodynamic properties, transport coefficients, and chemical kinetics calculations, enabling non-unity Lewis number formulations essential for accurate species diffusivity modelling. Validation was performed on the backward-facing step configuration and the well-documented Sandia Flame D turbulent jet flame, demonstrating the code's capability for both canonical and practically-relevant combustion configurations.

Major contribution to MFSim's reactive flow development came from (ELIAS, 2023), who addressed the computational challenges associated with detailed chemical kinetics in industrial combustion applications. This work developed a virtual/optimised kinetic mechanism methodology specifically designed for complex gaseous fuel mixtures encountered in industrial settings, such as CO boiler fuel compositions. The approach employed kinetic reduction techniques to identify the minimum set of species and reactions required to accurately represent the combustion chemistry, followed by differential evolution optimisation to determine the parameters of simplified virtual mechanisms that reproduce the essential behaviour of detailed schemes at significantly reduced computational cost. Validation through one-dimensional premixed laminar flame calculations demonstrated the methodology's ability to transfer the complexity of detailed mechanisms into computationally tractable formulations while preserving flame speed, temperature profiles, and major species concentrations.

Most recently, (CHIUMENTO, 2024) extended MFSim's reactive flow capabilities to compressible flow regimes, addressing applications where acoustic effects, shock waves, and significant density variations cannot be neglected. This work implemented a compressible PISO (Pressure-Implicit with Splitting of Operators) algorithm designed to handle all Mach number regimes within a unified framework, from nearly incompressible to supersonic conditions. The methodology was coupled with the existing Immersed Boundary Method (IBM) and Adaptive Mesh Refinement (AMR) infrastructure, enabling simulations of reactive flows in complex geometries with moving boundaries. Both LES and Unsteady Reynolds-Averaged Navier-Stokes (URANS) turbulence models were made available, with the Eddy Dissipation Concept (EDC) employed for turbulence-chemistry interaction closure. Validation encompassed a comprehensive set of test cases including shock tube problems, natural convection, bluff body stabilised flames, and supersonic step flows, demonstrating the solver's accuracy across diverse flow regimes.

The progressive development of reactive flow simulation capabilities in MFSim, summarised in Table 3.2, reflects a systematic effort to address the diverse requirements of turbulent combustion modelling—from foundational LES/PDF frameworks for premixed flames, through AMR-enabled simulations with detailed chemistry, to virtual mechanism approaches for industrial applications and compressible formulations for high-speed reactive flows. The present work continues this trajectory by implementing the TFM, complementing the existing methodologies with an algebraic combustion closure that offers computational efficiency

Table 3.2: Development of reactive flow simulation capabilities in MFSim.

Reference	Main Contribution	Combustion Model	Key Features
(VEDOVOTO, 2011)	Foundational reactive flow solver	LES/PDF hybrid framework	Low Mach number, variable density, Monte Carlo PDF
(DAMASCENO, 2018)	AMR for reactive flows	LES with detailed chemistry	Cantera integration, TVD schemes, non-unity Lewis
(ELIAS, 2023)	Virtual kinetic mechanisms	Optimised reduced chemistry	Differential evolution, industrial fuels
(CHIUMENTO, 2024)	Compressible reactive flows	EDC turbulence-chemistry	All Mach regimes, PISO algorithm, IBM coupling
Present work	Thickened Flame Model	TFM with dynamic thickening	Algebraic closure, efficiency functions, flame sensor

while maintaining flame propagation physics through explicit treatment of the flame front thickening and subgrid wrinkling effects.

3.3 TFM Implementation in MFSim

This section describes the implementation of the TFM in MFSim, including the numerical algorithm and its integration with the main solver, and practical considerations regarding computational cost. The mathematical formulation of the TFM was presented in Section 3.1.6; here, the focus is on the specific choices made for the numerical treatment and the interaction with MFSim's existing infrastructure.

The TFM implementation is written in Fortran 90/95, consistent with the MFSim codebase. C++ interfaces are employed for Cantera integration, enabling access to thermodynamic properties, transport coefficients, and chemical kinetics. The modular design follows modern Fortran practices with explicit interfaces and encapsulated data structures.

3.3.1 Numerical Algorithm and Solver Integration

3.3.1.1 Time Integration Framework

MFSim employs a flexible multi-physics time integration strategy. The primary method uses operator splitting with Implicit-Explicit (IMEX) schemes (ASCHER; RUUTH; SPITERI, 1997), where advective terms are treated explicitly (Adams-Bashforth) and diffusive terms are treated implicitly (Crank-Nicolson). Several IMEX schemes are available: Semi-implicit Backward Differencing Formula (SBDF), Adams-Bashforth Crank-Nicolson (ABCN), Modified Crank-Nicolson Adams-Bashforth (MCNAB), and Crank-Nicolson Leap-Frog (CNLF).

For chemistry integration, MFSim supports both fully coupled and operator-split approaches. In the coupled mode, chemistry and transport are solved together within the scalar equation loop. In the operator-split mode, Strang splitting (STRANG, 1968) is available:

$$\text{Chemistry}\left(\frac{\Delta t}{2}\right) \rightarrow \text{Transport}(\Delta t) \rightarrow \text{Chemistry}\left(\frac{\Delta t}{2}\right), \tag{3.3.1}$$

which provides second-order temporal accuracy. The chemistry sub-steps are integrated using Cantera's interface (GOODWIN; MOFFAT; SPETH, 2009) to the CVODE solver from the SUNDIALS suite (HINDMARSH et al., 2005), which employs adaptive time-stepping for stiff ordinary differential equations.

For the validation cases presented in Chapter 5, the SBDF scheme was employed for all balance equations, with second-order Strang splitting for chemistry integration.

3.3.1.2 TFM Computational Algorithm

The TFM computation is performed once per global time step, prior to the transport equation sub-stages. Two flame sensor formulations are available, selected via user input parameter (`tfm_sensor_type`): the Durand and Polifke sensor (type 1) based on progress variable, and a modified Han sensor (type 2) based on fuel reaction rate. Algorithm 1 summarises the computational workflow.

The Durand and Polifke sensor (DURAND; POLIFKE, 2007) employs a temperature-based progress variable:

$$c = \frac{T - T_u}{T_{ad} - T_u}, \tag{3.3.2}$$

Algorithm 1 TFM computational workflow per time step

Require: Field variables $T(\vec{x})$, $\dot{\omega}_F(\vec{x})$, $\tilde{\vec{u}}(\vec{x})$; TFM parameters (T_u, T_{ad}, S_L^0, $F_{\max}$, Ω_0, β); sensor type

Ensure: TFM fields: sensor $\Omega(\vec{x})$, thickening factor $F(\vec{x})$, efficiency $E(\vec{x})$

Step 1: Compute flame sensor

if sensor type = Durand and Polifke **then**
  for each cell i **do**
    $c_i \leftarrow \max(0, \min(1, (T_i - T_u)/(T_{ad} - T_u)))$ ▷ Eq. (3.3.2)
    $\Omega_i \leftarrow 16\, c_i^2 (1 - c_i)^2$ ▷ Eq. (3.3.3)
  end for
else if sensor type = Han **then**
  $|\dot{\omega}_F|_{\max} \leftarrow \max_{\text{domain}}(|\dot{\omega}_F|)$ ▷ MPI reduction, excluding ghost cells
  for each cell i **do**
    $\Omega_i \leftarrow \max\left\{ \left(\tanh\left(100 \frac{|\dot{\omega}_{F,i}|}{|\dot{\omega}_F|_{\max}} \right) - 0.25 \right) / 0.75,\ 0 \right\}$ ▷ Eq. (3.3.4)
  end for
end if
for each cell i **do**
  if $\Omega_i < \Omega_0$ **then**
    $\Omega_i \leftarrow 0$ ▷ Threshold to avoid thickening in non-reacting regions
  end if
end for

Step 2: Compute dynamic thickening factor

for each cell i **do**
  $F_i \leftarrow 1 + (F_{\max} - 1) \cdot \Omega_i$ ▷ Eq. (3.3.5)
end for

Step 3: Compute subgrid velocity and efficiency function

for each cell i **do**
  $u'_{\Delta,i} \leftarrow$ subgrid velocity from dynamic Smagorinsky model
  $\Xi_i \leftarrow \left(1 + \min\left[F_i - 1, \frac{u'_{\Delta,i}}{S_L^0} \right] \right)^{\beta}$ ▷ Eq. (3.3.6)
  $E_i \leftarrow \max(1, \Xi_i)$ ▷ Ensure $E \geq 1$
end for

Step 4: Update ghost cells

Apply zero-gradient (Neumann) boundary conditions to Ω, F, and E fields

Step 5: Modify source terms and diffusion fluxes

for each cell i and species k **do**
  $\dot{\omega}_{k,i}^{\text{eff}} \leftarrow (E_i / F_i) \cdot \dot{\omega}_{k,i}$ ▷ Eq. (3.1.23)
end for
for each cell face **do**
  $D_k^{\text{eff}} \leftarrow E \cdot F \cdot D_k$ ▷ Enhanced molecular diffusivity
end for

where T_u is the unburnt gas temperature and T_{ad} is the adiabatic flame temperature, obtained from a one-dimensional freely propagating flame calculation prior to simulation. The sensor takes the parabolic form:

$$\Omega = 16\, c^2(1-c)^2, \tag{3.3.3}$$

which equals unity at $c = 0.5$ and vanishes in fresh and burnt gases.

The modified Han sensor (HAN et al., 2019) uses fuel reaction rate directly:

$$\Omega = \max\left\{\left(\tanh\left(100\frac{|\dot{\omega}_F|}{|\dot{\omega}_F|_{\max}}\right) - 0.25\right)/0.75,\ 0\right\}, \tag{3.3.4}$$

where $|\dot{\omega}_F|_{\max}$ is the maximum fuel reaction rate in the domain, computed at each time step via MPI reduction excluding ghost cells. This sensor is chemistry-aware and does not require pre-specified temperature bounds.

The dynamic thickening factor follows the standard DTF formulation:

$$F = 1 + (F_{\max} - 1)\cdot\Omega, \tag{3.3.5}$$

where $F_{\max}$ is user-specified based on grid resolution requirements.

The efficiency function employs the Wang-modified Charlette formulation (WANG; BOILEAU; VEYNANTE, 2011) to account for sub-grid scale flame wrinkling. To ensure the efficiency approaches unity when the flame is fully resolved ($F \to 1$), the saturation term is defined as $(F-1)$:

$$\Xi = \left(1 + \min\left[F-1, \frac{u'_\Delta}{S_L^0}\right]\right)^\beta, \tag{3.3.6}$$

where $\beta = 0.5$ is the power-law exponent, S_L^0 is the unstretched laminar flame speed, and u'_Δ is the sub-grid velocity fluctuation obtained from the dynamic Smagorinsky model. In the present implementation, the spectral efficiency function is simplified to $\Gamma_\Delta = 1$, assuming unit efficiency for flame straining by sub-grid eddies. The minimum operator ensures that the model respects the geometric saturation limit determined by the thickening factor $(F-1)$ in regions of high turbulence intensity. The sensor threshold is set to $\Omega_0 = 0.01$ to prevent spurious thickening in regions with negligible reaction activity.

3.3.1.3 Coupling with Chemistry Solver

A key aspect of the implementation is the point at which TFM modifications are applied relative to the chemistry integration. The TFM fields are computed from the current state at the beginning of each time step, and the modifications to reaction rates and diffusion fluxes are applied after the base reaction rates have been evaluated by Cantera.

In coupled mode, the sequence within each time step is:

A. Compute TFM fields (Ω, F, E) from current temperature and reaction rates;

B. Evaluate reaction rates via Cantera: $\dot{\omega}_k(T, Y_1, \ldots, Y_{N_s})$;

C. Apply TFM modification: $\dot{\omega}_k^{\text{eff}} = (E/F)\dot{\omega}_k$;

D. Solve transport equations with modified source terms and enhanced diffusion.

In operator-split mode with Strang splitting:

A. Chemistry half-step via CVODE (unmodified kinetics);

B. Compute TFM fields from updated temperature and reaction rates;

C. Transport step with TFM-modified diffusion;

D. Chemistry half-step via CVODE (unmodified kinetics).

Importantly, the stiff ODE integrator (CVODE) always operates on unmodified chemical kinetics. The TFM modification is applied only to the source terms that enter the transport equations, not to the internal chemistry integration. This approach ensures that the detailed balance and thermodynamic consistency of the chemical mechanism are preserved.

3.3.1.4 Interaction with Adaptive Mesh Refinement

MFSim's block-structured AMR capability introduces specific considerations for TFM field management. TFM fields are updated every time step, while mesh adaptation occurs less frequently (typically every 50–200 time steps). Thus, TFM fields are recomputed many times between successive mesh modifications.

TFM fields (Ω, F, E) are treated as purely diagnostic quantities derived algebraically from the primary state variables. During mesh adaptation, these fields are not interpolated; instead,

they are deallocated, reallocated to the new mesh topology, initialised to default values ($F = 1$, $E = 1$, $\Omega = 0$), and recomputed from the (interpolated) state fields on the next time step. This approach avoids interpolation artefacts and ensures consistency with the underlying thermodynamic state.

On AMR grids the cell dimensions $(\Delta x, \Delta y, \Delta z)$ vary across refinement levels. The implementation traverses the AMR patch hierarchy to obtain cell-specific spacing when computing the thickening factor. For the current implementation with user-specified $F_{\max}$, the local grid spacing is used primarily for diagnostic purposes; future extensions incorporating automatic F selection based on $\Delta x/\delta_L^0$ will make direct use of this information.

3.3.1.5 Boundary Conditions

The TFM fields employ zero-gradient (Neumann) boundary conditions at all domain boundaries:

$$\frac{\partial \Omega}{\partial n} = 0, \quad \frac{\partial F}{\partial n} = 0, \quad \frac{\partial E}{\partial n} = 0, \tag{3.3.7}$$

where n denotes the outward normal direction. This treatment is applied uniformly at inflow, outflow, and wall boundaries. At inter-patch boundaries within the AMR hierarchy, ghost cell values are populated through the standard communication routines used for other scalar fields.

3.3.1.6 Limitations and Future Work

The current implementation has two aspects that merit consideration for future development. The time step calculation in MFSim accounts for advective and diffusive stability limits, but does not explicitly incorporate the TFM-enhanced diffusivity $D_{\text{eff}} = EF \cdot D$. For the implicit treatment of diffusive terms employed in the IMEX schemes, unconditional stability is maintained regardless of the enhancement factor. However, applications using explicit diffusion treatment with large thickening factors ($F > 10$) may require additional stability considerations.

Secondly, the uniform zero-gradient boundary conditions provide a simple and robust treatment, but do not distinguish between inflow and outflow boundaries. For configurations where the flame interacts strongly with domain boundaries, specialised treatments (e.g., resetting $F = 1$ and $E = 1$ at inflow) may be beneficial. The current approach is adequate for

the validation cases considered in this work, where flames remain sufficiently distant from domain boundaries.

3.3.2 Computational Complexity and Practical Considerations

The TFM introduces additional operations at each time step, but the associated computational overhead is modest compared to the baseline reacting flow solver. The dominant costs in turbulent combustion simulations are typically the chemistry integration (evaluation of reaction rates and, for operator splitting, the stiff ODE solution) and the pressure Poisson solve. The TFM adds only algebraic operations—progress variable evaluation, sensor computation, and scalar multiplications—that scale linearly with the number of cells. The Han sensor incurs an additional MPI reduction operation per time step to determine $|\dot{\omega}_F|_{\max}$ across the domain.

In practice, the TFM overhead is typically less than 5% of the total wall-clock time per time step. This estimate is consistent with the simple structure of Algorithm 1, which involves no iterative procedures, no additional linear system solutions, and minimal communication beyond the standard ghost cell updates.

The primary benefit of the TFM lies not in computational efficiency of the model itself, but in the enabling of significantly coarser computational grids. By artificially thickening the flame front to span a specified number of grid points ($n_c \approx 5$–10), the TFM allows grid spacings that would otherwise be insufficient to resolve the flame structure. For typical hydrocarbon flames with $\delta_L^0 \sim 0.1$–1 mm, direct resolution would require $\Delta x \sim 10$–100 μm, while TFM-enabled simulations can employ $\Delta x \sim 0.5$–2 mm. This reduction in resolution requirements can decrease the total cell count by one to two orders of magnitude in three-dimensional simulations, with corresponding reductions in computational cost and memory requirements.

Quantitative performance analysis for specific configurations is presented alongside the validation results in Chapter 5. Table 3.3 summarises the key aspects of the TFM implementation in MFSim.

Table 3.3: Summary of TFM implementation in MFSim.

Aspect	**Implementation**
Flame sensor (type 1)	Durand and Polifke: $\Omega = 16c^2(1-c)^2$ with $c = (T - T_u)/(T_{ad} - T_u)$
Flame sensor (type 2)	Modified Han: $\Omega = \max\{(\tanh(100\lvert\dot{\omega}_F\rvert/\lvert\dot{\omega}_F\rvert_{\max}) - 0.25)/0.75, 0\}$
Thickening factor	Dynamic: $F = 1 + (F_{\max} - 1)\Omega$
Efficiency function	Wang-modified Charlette: $E = (1 + \min[F - 1, u'_\Delta/S_L^0])^\beta$
Subgrid velocity	From MFSim's dynamic Smagorinsky model
Default constants	$\beta = 0.5$, $\Omega_0 = 0.01$
Pre-computed quantities	T_{ad}, S_L^0 from 1D freely propagating flame (Cantera)
Time integration	IMEX schemes (SBDF default); Strang splitting for chemistry
Chemistry coupling	Post-evaluation modification; CVODE sees unmodified kinetics
AMR support	Fields recomputed after remesh (not interpolated)
Boundary conditions	Zero-gradient (Neumann) at all boundaries
Parallelisation	MPI-compatible; global reduction for Han sensor

VERIFICATION AND VALIDATION METHODOLOGY

This chapter describes the verification and validation strategies employed to assess the TFM implementation in MFSim and demonstrate its applicability across different configurations. The validation investigates turbulent premixed Bunsen flames.

4.1 Turbulent Bunsen Flame F3

The turbulent Bunsen flame configuration studied by Chen et al. (CHEN, Y.-C. et al., 1996) provides a well-documented validation case for turbulent premixed combustion.

Three flames (F1, F2, F3) at different exit velocities were characterised in the original study. For validation of the TFM implementation, Flame F3 is selected as the target case. Operating at the lowest Reynolds number, Flame F3 exhibits flamelet behaviour where the laminar-like flame structure is preserved despite turbulent wrinkling. This regime is particularly appropriate for TFM validation, as the model assumptions regarding thin flame fronts wrinkled by turbulence are most applicable.

4.1.1 Operating Conditions

Table 4.1 summarises the operating conditions for Flame F3.

The characteristic turbulence and flame scales at the nozzle exit ($U_{\text{bulk}} = 30.7$ m/s) are:

- Integral length scale $l_0 = 3.60$ mm;
- Taylor microscale $\lambda = 0.17$ mm;
- Laminar flame thickness $\delta_L^0 = 0.42$ mm.

Table 4.1: Operating conditions for Chen turbulent Bunsen Flame F3 (CHEN, Y.-C. et al., 1996).

Parameter	**Value**
Fuel	Methane-air (stoichiometric, $\phi = 1.0$)
Nozzle diameter D	12 mm
Mean nozzle exit velocity U_0	30.7 m/s
Reynolds number Re_D	$\approx$ 24,000
Pilot stream	Stoichiometric CH_4-air at equilibrium
Chemical mechanism	Yang & Pope (16 species) (YANG, B.; POPE, 1998)
Transport model	Mixture-averaged

4.1.2 Computational Domain and Boundary Conditions

The computational domain extends $L_x \times L_y \times L_z = 0.36 \times 0.36 \times 0.018$ m, corresponding to $30D \times 30D \times 1.5D$. Periodicity is applied in the z-direction, which for both tested meshes holds a single cell on its direction, to approximate an axisymmetric configuration with reduced computational cost. Table 4.2 summarises the boundary conditions.

Table 4.2: Boundary conditions for Flame F3 simulations.

Boundary	**Location**	**Condition**
South (inlet)	$y = 0$	Dirichlet: velocity, T and Y_k profiles from experiment
North (outlet)	$y = L_y$	Advective outflow for velocity; Neumann: T and Y_k
East	$x = 0$	Dirichlet
West	$x = L_x$	Dirichlet
Bottom/Top	$z = 0, L_z$	Periodic

Turbulent inflow conditions are generated using synthetic turbulence with target statistics matching the measured profiles at $x/D = 0.5$ from Chen et al. (CHEN, Y.-C. et al., 1996).

4.1.3 Grid Resolution Strategy

Two grid configurations are employed to investigate the TFM behaviour across different resolution regimes, as summarised in Table 4.3.

Table 4.3: Mesh configurations for Flame F3 simulations.

Mesh	Δx [mm]	$\Delta x/\lambda$	$F_{\max}$	δ_{TF} [mm]
Production (standard LES)	0.34	≈ 2	6.5	2.7
Coarse (model limit)	0.68	≈ 4	13.0	5.5

The production mesh ($\Delta x = 0.34$ mm) represents the optimal balance between computational cost and physical fidelity. The mesh acts as a spatial filter within the inertial subrange. With $F_{\max} = 6.5$, the thickened flame thickness $\delta_{TF} \approx 2.7$ mm remains smaller than the integral length scale ($\delta_{TF} < l_0$), ensuring that the flame macro-structure is transported and deformed by resolved eddies while subgrid wrinkling is recovered by the efficiency function.

Meanwhile, the coarse mesh ($\Delta x = 0.68$ mm) explores the TFM applicability limit. To maintain minimum numerical resolution (8 points across the flame), $F_{\max} \approx 13.0$ is required, yielding $\delta_{TF} \approx 5.5$ mm. Since $\delta_{TF} > l_0$, the thickened flame exceeds the integral scale, and the artificial viscosity damps vortices that should wrinkle the flame. This configuration demonstrates the breakdown of turbulence-flame interaction when excessive thickening is applied.

The base grid consists of $128 \times 128 \times 1$ cells with 4 levels and refinement ratio of 2 in the x and y directions. The finest cells at the flame region achieve the target resolutions specified in Table 4.3. Refinement criteria are based on temperature and CO mass fraction gradients.

Both flame sensor formulations are evaluated for production mesh configuration only, this yields three simulations in total.

4.1.4 Simulation Parameters and Validation

The time integration employs the SBDF scheme with a fixed time step $\Delta t = 2.5 \times 10^{-7}$ s. Statistics are collected after the flow reaches a statistically stationary state over a time-averaging period of approximately 10 flow-through times. The TFM model parameters include the Wang-modified Charlette efficiency function (Eq. 3.3.6) with $\beta = 0.5$, a subgrid velocity derived from MFSim's dynamic Smagorinsky model, a sensor threshold of $\Omega_0 = 0.01$, and a laminar flame speed S_L^0 obtained from 1D Cantera calculations. Additionally, the modified Han sensor formulation (Eq. 3.3.4) is employed for both mesh configurations. This chemistry-aware sensor, based on fuel reaction rate, provides robust flame detection across the different turbulence intensities and local equivalence ratio variations present in the turbulent flame brush. Finally, experimental data from Chen et al. (CHEN, Y.-C. et al., 1996) provide validation metrics, including mean and RMS velocity profiles at multiple axial stations, mean and RMS temperature profiles, and mean species mass fractions for major species (CH_4, O_2, CO_2, H_2O) and intermediates (CO,OH,H_2).

RESULTS AND DISCUSSION

This chapter presents the validation results for the TFM implementation in MFSim. The validation is conducted using two-dimensional turbulent Bunsen flames, exploring the model's accuracy across grid resolutions and flame sensor formulations.

5.1 Turbulent Bunsen Flame F3

The turbulent Bunsen flame F3 provides validation of the TFM implementation under turbulent conditions, where the model's ability to capture flame-turbulence interaction through the efficiency function becomes critical. Three configurations are investigated, as summarized in Table 5.1. Case 1 employs the production mesh ($\Delta x = 0.34$ mm, $F_{\max} = 6.5$) with the modified Han sensor, representing the baseline configuration with reaction-rate-based flame detection. Case 2 uses the coarse mesh ($\Delta x = 0.68$ mm, $F_{\max} = 13.0$) with the same Han sensor, exploring the model's applicability limits under excessive thickening. Case 3 shares the identical mesh and thickening factor of Case 1 but employs the Durand & Polifke temperature-based (progress variable) sensor, thereby isolating the effect of flame sensor selection from grid resolution and thickening factor influences. Results are compared against experimental measurements from Chen et al. (CHEN, Y.-C. et al., 1996), including radial profiles of velocity, temperature, and species mass fractions at multiple axial stations downstream of the nozzle exit.

Table 5.1: Summary of computational configurations for the turbulent Bunsen flame F3 simulations.

Parameter	**Case 1**	**Case 2**	**Case 3**
Finest cell size [mm]	0.34	0.68	0.34
$F_{\max}$	6.5	13.0	6.5
δ_{TF} [mm]	≈ 2.7	≈ 5.5	≈ 2.7
Flame sensor	Modified Han	Modified Han	Durand & Polifke
Sensor basis	Reaction rate	Reaction rate	Progress variable

The comparison between Cases 1 and 2 quantifies the effect of grid resolution and thickening factor magnitude, while the comparison between Cases 1 and 3 isolates the influence of flame sensor formulation at identical mesh resolution and thickening parameters. This factorial approach enables independent assessment of the two principal modelling choices in the TFM framework: the thickening factor magnitude and the spatial extent over which thickening is applied.

5.1.1 Mean and Fluctuating Velocity Profiles

The velocity field characterization provides fundamental validation of the TFM's ability to capture the flow dynamics in turbulent reacting flows. The interaction between combustion and turbulence manifests through thermal expansion, which modifies the velocity field, and through turbulence generation mechanisms associated with density gradients across the flame brush. Understanding these coupled phenomena is essential for assessing the model's predictive capability.

Figure 5.1 shows the axial evolution of mean normalized velocity along the centerline. The centerline velocity provides a one-dimensional representation of the jet development, capturing the initial potential core region near the nozzle exit followed by the transition to a fully developed turbulent jet.

All three cases reproduce the overall trend of centerline velocity evolution. In the near-field region ($y/D < 4$), the simulations match the experimental data closely, indicating that the inlet boundary conditions and initial flame establishment are well-captured regardless of the sensor formulation. The slight velocity increase beginning around $y/D \approx 6$ reflects flow acceleration as the turbulent flame brush develops. Downstream of $y/D \approx 9$, Case 2 shows a tendency to over-predict the mean velocity by approximately 5–8%, while Case 1 presents a lower deviation from the experimental profile. Case 3 exhibits intermediate behaviour between Cases 1 and 2, with a more pronounced over-prediction of centerline velocity compared to Case 1 despite sharing the same mesh and $F_{\max}$.

The over-prediction observed in Case 3 is attributed to the broader spatial extent over which the Durand & Polifke sensor activates the thickening procedure. Unlike the Han sensor, which confines thickening to regions of active chemical reaction, the temperature-based sensor activates across the entire thermal transition zone, including preheat and post-flame regions. This broader application of artificial diffusion modifies the pressure field and flow ac-

celeration over a larger volume, leading to enhanced centerline velocities despite the identical thickening factor magnitude.

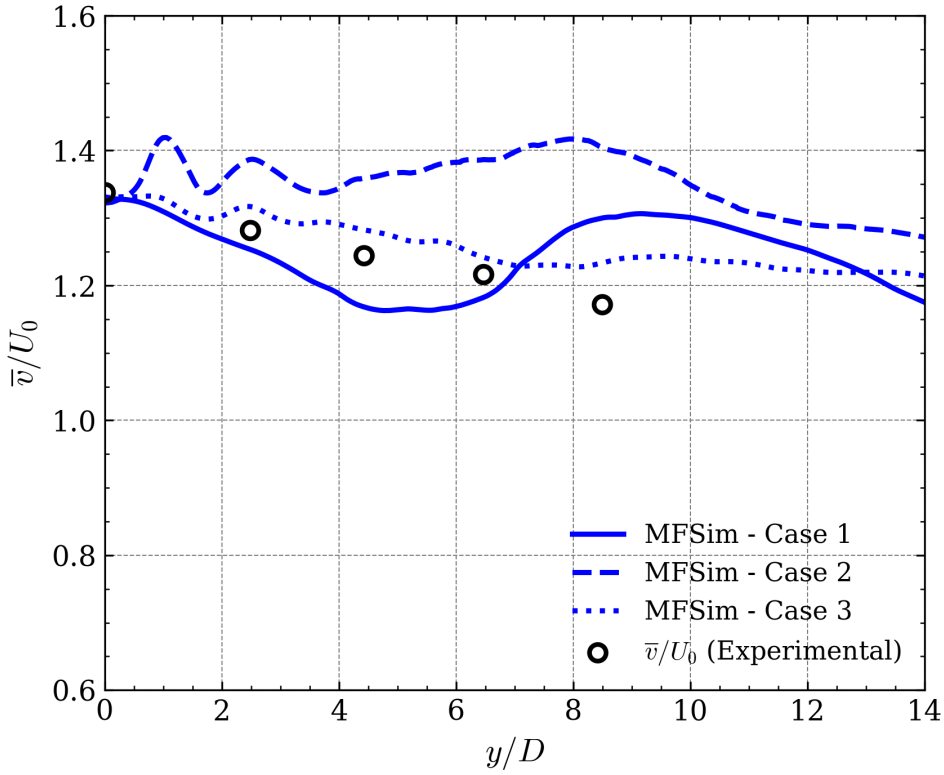

Figure 5.1: Centerline profiles of mean axial normalized velocity as functions of axial distance y/D. Experimental data from Chen et al. (CHEN, Y.-C. et al., 1996) compared against three cases.

The good agreement in mean velocity for all three cases demonstrates that the TFM correctly preserves the mean flow acceleration induced by combustion despite the different thickening factors and sensor formulations employed. This behaviour confirms that the TFM transformation maintains the integral effect of heat release on the flow field, even when the detailed flame structure is artificially modified. The (E/F) scaling of reaction source terms ensures that the total heat release rate integrated over the flame brush remains consistent with the unthickened flame, thereby preserving global flow acceleration.

Figure 5.2 shows the axial evolution of mean normalized kinetic energy along the centerline. The turbulent kinetic energy quantifies the intensity of velocity fluctuations and provides insight into the turbulence-flame interaction.

The profiles reveal significantly greater sensitivity to both grid resolution and sensor formulation compared to mean velocity. All three cases capture the initial potential core ($y/D < 3$) and the subsequent rise as the shear layer develops. However, the downstream

evolution diverges substantially among the cases, with a non-physical accumulation of kinetic energy that varies in magnitude. Several compounding factors contribute to these discrepancies.

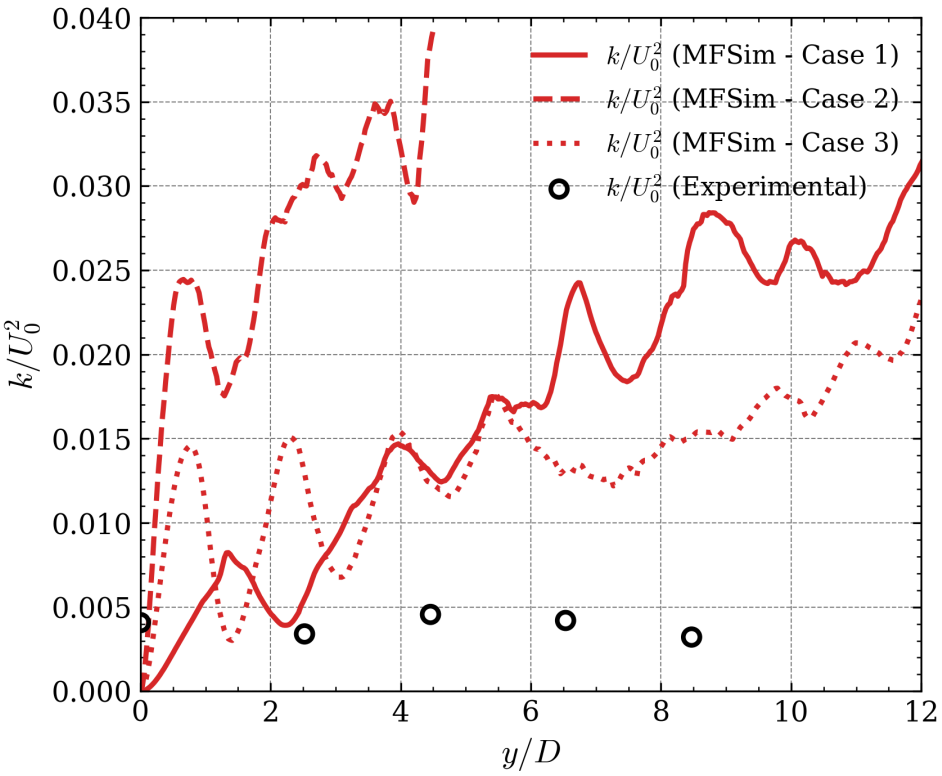

Figure 5.2: Centerline profile of mean axial normalized kinetic energy as functions of axial distance y/D. Experimental data from Chen et al. (CHEN, Y.-C. et al., 1996) compared against three cases.

First, the two-dimensional domain assumption fundamentally suppresses three-dimensional turbulent fluctuations that would be present in the fully axisymmetric experimental configuration. This geometric simplification affects all cases equally and accounts for a baseline deviation from experimental data. The spanwise periodicity enforces coherent structures across the limited domain width, preventing the full development of three-dimensional instabilities and the energy cascade that characterize true turbulent flows. Since fully developed three-dimensional structures are not present, the turbulent viscosity that would be produced by the lacking third dimension is absent, reducing the dissipation of turbulent kinetic energy through the energy cascade.

Second, the thickening factor directly impacts turbulence-flame interaction through the enhanced diffusion coefficients. In Case 2, with $F_{\max} = 13.0$, the thickened flame thickness $\delta_{\text{TF}} \approx 5.5$ mm exceeds the integral turbulent length scale. This violation of the recommended

criterion $\delta_{TF} < l_0$ has profound implications: the high kinetic energy observed represents large-scale "flapping" structures that no longer interact properly with the flame. By thickening these large 2D structures ($F > 1$), the model prevents numerical dissipation, allowing high-energy oscillations to persist and grow unchecked throughout the domain. The higher the thickening, the lower the numerical dissipation, which explains the severe over-prediction of Case 2.

Third, and most relevant for differentiating Cases 1 and 3, the flame sensor formulation determines the spatial extent of enhanced diffusion. Case 3 presents kinetic energy values higher than Case 1 but substantially lower than the non-physical accumulation observed in Case 2. The broader activation region of the Durand & Polifke sensor applies artificial diffusion over a more extensive zone, which partially damps small-scale instabilities while simultaneously preserving larger coherent structures that contribute to the kinetic energy. Since Cases 1 and 3 share identical mesh and F_{max}, the difference between their kinetic energy profiles directly quantifies the isolated effect of sensor choice on turbulence-flame coupling. The progressive improvement from Case 2 to Case 3 to Case 1 demonstrates that both the thickening factor magnitude and the spatial selectivity of the sensor are essential parameters for preserving turbulence-flame coupling in the TFM framework.

Case 1, with $\delta_{TF} \approx 2.7$ mm $< l_0$ and localized sensor activation, allows resolved eddies at the integral scale to deform the flame surface while relying on the efficiency function to recover only the subgrid wrinkling from scales smaller than the thickened flame thickness. This scale separation aligns with the fundamental LES philosophy and explains Case 1's superior performance in capturing kinetic energy evolution.

Figure 5.3 presents radial profiles of mean normalized axial velocity and mean normalized axial kinetic energy at four axial stations ($y/D = 2.5, 4.5, 6.5, 8.5$). The mean velocity profiles characterize the jet spreading and deceleration downstream of the nozzle, while the kinetic energy profiles capture the turbulence intensity evolution through the flame brush.

The radial velocity profiles show that all three cases struggle to capture the jet spreading rate and the velocity decay from the centerline to ambient conditions. From $y/D = 2.5$ through 8.5, the simulations over-predict the velocity half-width and centerline magnitude, a result inconsistent with the rapid decay observed in the experimental data. This fundamental discrepancy originates from the two-dimensional assumption, which prevents the formation

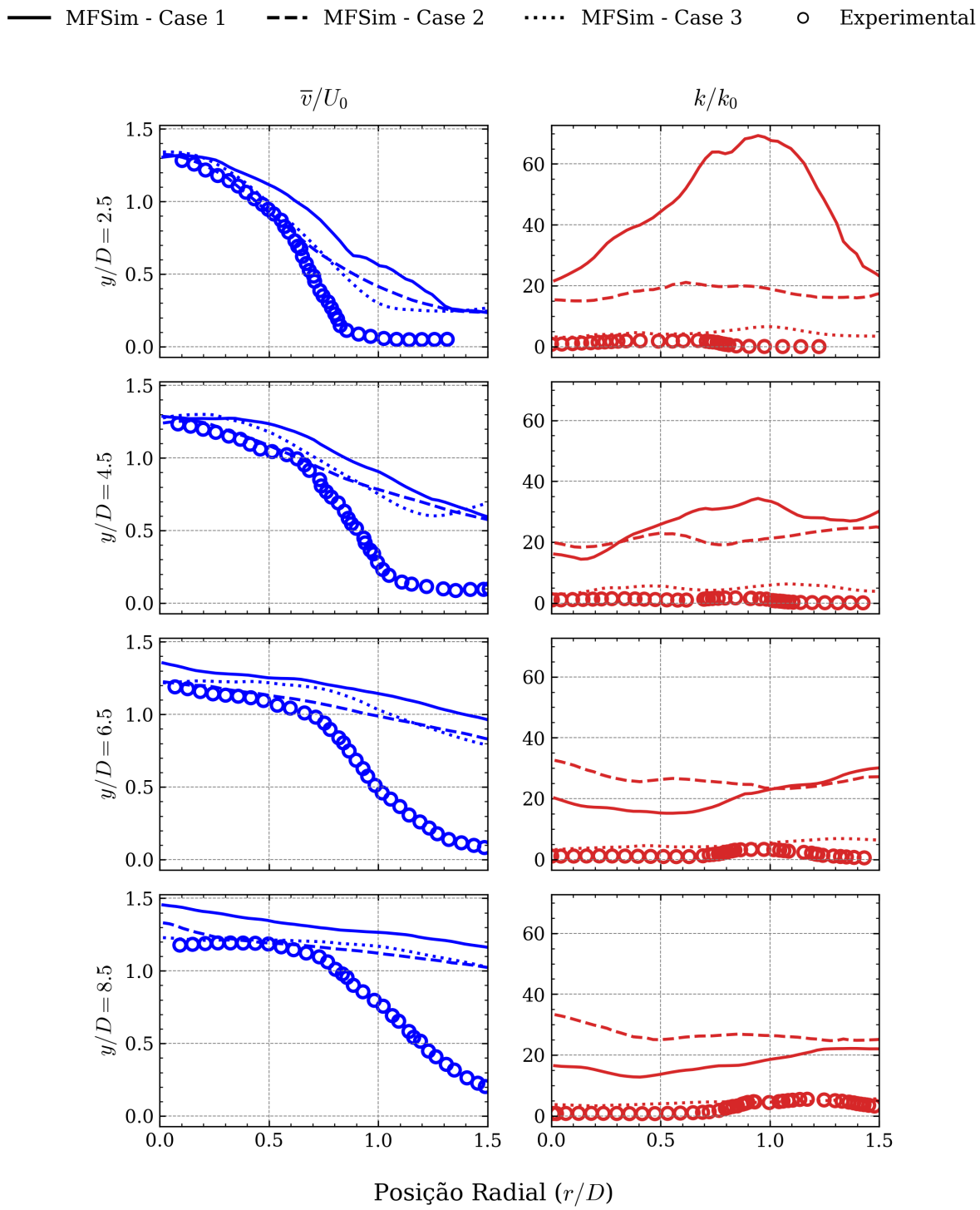

Figure 5.3: Radial profiles of mean axial velocity (left column) and axial kinetic energy (right column) at axial stations $y/D = 2.5, 4.5, 6.5, 8.5$. Experimental data from Chen et al. (CHEN, Y.-C. et al., 1996) compared against three simulations.

of the streamwise vorticity required to break down the potential core and drive radial momentum exchange.

At the first station ($y/D = 2.5$), Case 3 shows improved agreement with the experimental data in the shear layer region ($r/D \approx 0.5$) compared to Case 1. At downstream stations, Case 3 tends to under-predict the velocity in the central region compared to Case 1, approaching the experimental values more closely at some locations. By $y/D = 8.5$, the velocity profiles exhibit a persistent "top-hat" structure in all cases rather than the developed Gaussian distribution seen in experiments. Neither case correctly predicts the self-similar spreading of the turbulent jet in the far field, indicating a fundamental limitation in representing large-scale mixing mechanisms within the 2D domain.

The radial kinetic energy profiles (right column) exhibit strong sensitivity to both resolution and sensor choice. At $y/D = 2.5$, the three cases begin to diverge from experimental values, and by $y/D = 8.5$, Case 2 over-predicts the peak magnitude by a factor of 20–30. Case 3 produces values significantly lower than Case 1 and closer to the experimental measurements at all stations. This reduced kinetic energy in Case 3 likely results from the broader thickening zone introduced by the temperature-based sensor, which provides more uniform artificial dissipation across the flame brush region. However, this improved agreement may arise for physically incorrect reasons: the additional dissipation masks the inherent 2D energy accumulation rather than capturing the correct three-dimensional energy cascade. This distinction is important because the apparent improvement does not reflect better turbulence modelling but rather a fortuitous cancellation of errors between the 2D domain limitation and the sensor-induced dissipation.

The persistent accumulation of kinetic energy across all downstream stations in Cases 1 and 2 indicates an inverse energy cascade, a characteristic artefact of 2D turbulence where energy is trapped in large scales rather than dissipating through the Kolmogorov cascade. This effect underscores the inability of the 2D domain to sustain a physical energy spectrum, regardless of the resolution, thickening factor, or sensor formulation applied in the flame zone.

In summary, the velocity field validation demonstrates that the 2D LES implementation introduces fundamental limitations in capturing mean flow features and jet spreading rates. The turbulent fluctuations show significant sensitivity to both the thickening factor and the sensor formulation, with the sensor choice proving comparably influential to grid resolution. Case 3's improved kinetic energy prediction, while numerically closer to experimental data,

must be interpreted cautiously as it may result from error cancellation rather than improved physical modelling.

5.1.2 Mean and Fluctuating Temperature Profiles

Figure 5.4 presents radial profiles of normalized mean temperature (left column) and normalized temperature RMS fluctuations (right column) at four downstream stations. Temperature provides a direct indicator of chemical heat release and serves as perhaps the most stringent test of the TFM's ability to maintain proper flame propagation characteristics while capturing the intermittency associated with turbulent flame brush passage.

The normalized mean temperature profiles (left column) reveal fundamental differences in flame brush structure among the three computational cases and the experimental measurements. The normalization is defined as $\overline{c} = (T - T_u)/(T_{ad} - T_u)$, where T_u is the unburnt gas temperature and T_{ad} is the adiabatic flame temperature, such that $\overline{c} = 0$ in fresh reactants and $\overline{c} = 1$ in fully burnt products.

The temperature profiles constitute the most critical comparison among the three sensor-resolution configurations. At the first measurement station ($y/D = 2.5$), Case 1 reaches $\overline{c}_{\max} \approx 0.95$, while experimental data shows $\overline{c}_{\max} \approx 0.70$. Case 2 exhibits even more pronounced incongruence with a linear profile from $\overline{c} \approx 0.2$ to $\overline{c} \approx 0.6$, skipping the S-shaped profile observed in both Case 1 and the experimental data, indicating premature and excessive heat release near the nozzle exit. Case 3, in contrast, significantly under-predicts the mean temperature across all radial positions, with $\overline{c}$ values substantially below both the experimental data and Case 1.

The discrepancy between Cases 1 and 3 persists and amplifies downstream. At $y/D = 4.5$, Case 1 maintains better agreement with experimental temperature ($\overline{c}_{\max} \approx 0.90$ vs. experimental 0.81), while Case 2 in the inner region $r/D \leq 0.5$ depicts $\overline{c}$ values approximately four times higher than experimental data. Case 3 shows temperatures up to 50% lower than the experimental measurements in the inner region ($r/D < 0.5$). By $y/D = 6.5$, Case 1 begins to diverge from experimental behaviour in the inner region, indicating excessive heat accumulation, while Case 3 continues to under-predict temperature throughout the radial extent.

At the furthest downstream station ($y/D = 8.5$), Case 2 shows a nearly uniform temperature field across $r/D < 0.8$, consistent with complete mixing and equilibration of combustion products. Case 1 approaches this behaviour with approximately narrower extent and higher

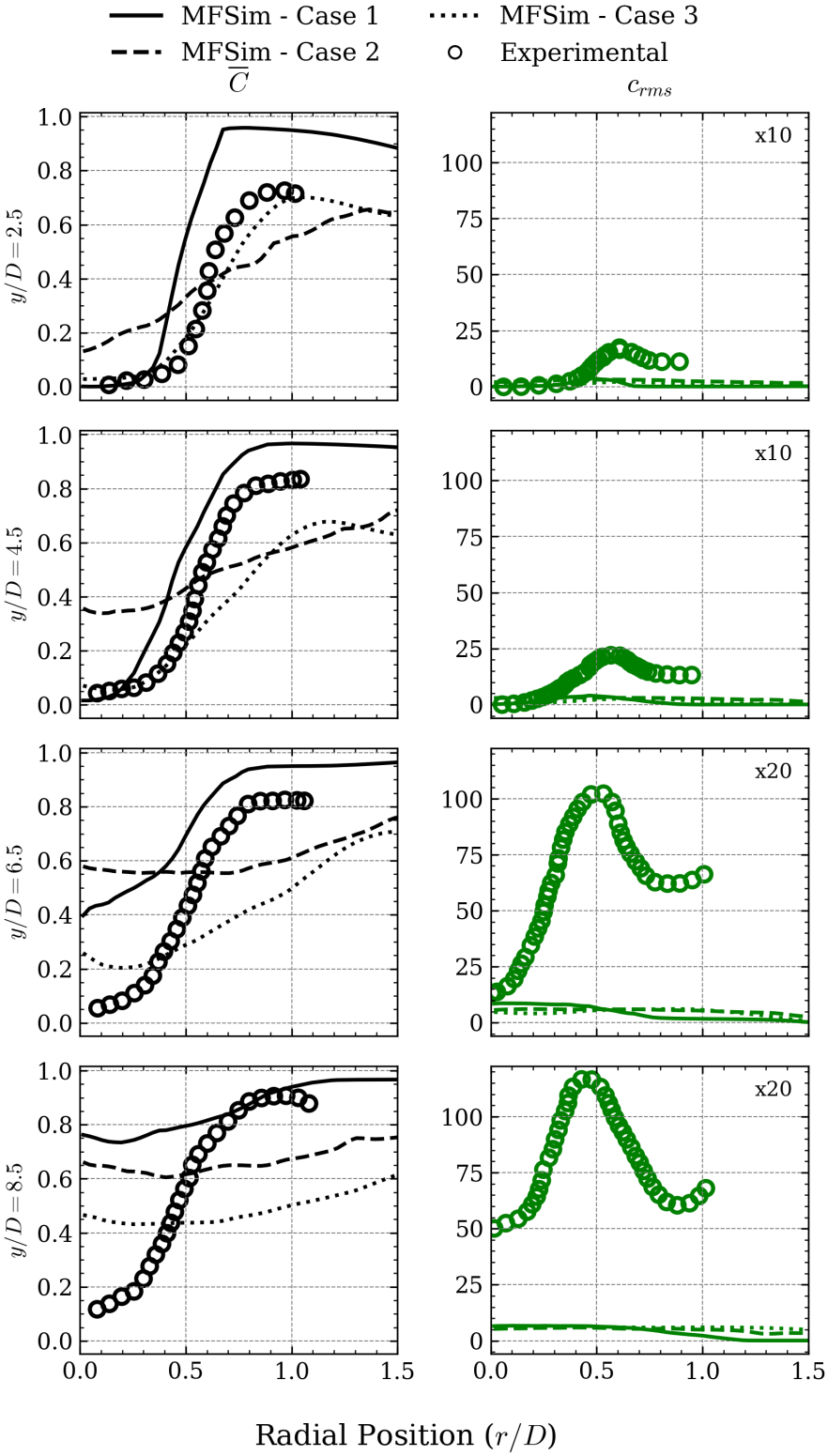

Figure 5.4: Radial profiles of mean temperature (left column) and temperature fluctuations (right column) at axial stations $x/D = 2.5, 4.5, 6.5, 8.5$. Experimental data from Chen et al. (CHEN, Y.-C. et al., 1996) compared against three simulations.

$\overline{c}_{\max}$ value, which is reasonably congruent with experimental data. Case 3, however, remains systematically below the experimental profile.

The under-prediction of temperature in Case 3 is directly attributable to the broader activation region of the Durand & Polifke sensor. By activating thickening across the entire thermal transition zone—including preheat and post-flame regions where no active chemistry occurs—the sensor distributes the effect of the TFM over an excessively large volume. Although the (E/F) scaling formally preserves the integrated heat release rate, the spatially diluted application of enhanced diffusivity effectively spreads the released thermal energy over a wider region than the physical flame occupies. This dilution reduces the local temperature within the reaction zone and retards the heating of the jet core, producing the systematic under-prediction observed at all stations.

This mechanism contrasts fundamentally with the behaviour of Cases 1 and 2. In Case 1, the Han sensor confines thickening to the narrow band of active chemical reaction, preserving the local intensity of heat release and yielding temperature profiles that, while over-predicted in the near-field, remain qualitatively consistent with the experimental S-shaped structure. In Case 2, the excessive thickening factor broadens the reaction zone through a different mechanism—increasing δ_{TF} beyond l_0—but the sensor still localizes the effect to reaction-rate regions. Case 3 demonstrates that even a moderate thickening factor ($F_{\max} = 6.5$), when applied over an inappropriately broad spatial extent, can produce temperature deficits comparable to or exceeding the errors introduced by an excessive thickening factor on a coarser grid.

In three-dimensional turbulent flames, azimuthal instabilities and streamwise vorticity generate radial momentum transport that broadens the jet and distributes thermal energy across a wider region. The 2D simulations suppress these mechanisms, confining heat release to a narrower radial extent than physically occurs. Additionally, the enhanced molecular diffusivity introduced by thickening does not adequately substitute for the missing three-dimensional turbulent transport, as molecular diffusion acts on different length scales and does not reproduce the large-scale mixing and advecting patterns generated by coherent turbulent structures.

The normalized temperature RMS fluctuations (right column) provide insight into the unsteady dynamics of the flame brush and the degree of intermittency as burnt and unburnt gases alternate passage through any given spatial location. The normalization c_{rms} represents

temperature fluctuations scaled by the temperature difference ($T_{ad} - T_u$), with peak values typically occurring at the flame brush centreline where the probability of observing either fresh reactants or burnt products is approximately equal.

At $y/D = 2.5$, the experimental data shows minimal temperature fluctuations ($c_{rms} < 10$, noting the ×10 scale factor), indicating that the flame has not yet fully developed turbulent characteristics at this near-field location. All three cases correctly predict near-zero fluctuations on the centreline, consistent with the stabilized, relatively steady flame base region. However, the radial distribution of fluctuations differs: experiments show a gradual increase toward $r/D \approx 0.5$, whereas Case 1 shows peak values 3–4 times lower, and Cases 2 and 3 produce negligible fluctuations across the entire radial extent.

By $y/D = 4.5$, experimental measurements reveal the emergence of significant temperature fluctuations with peak values $c_{rms} \approx 25$ (plotted as 2.5 on the ×10 scale) located near $r/D \approx 0.6$, marking the radial position where the flame brush passes intermittently. All three cases severely under-predict these fluctuations, indicating that neither the grid resolution nor the sensor formulation can overcome the fundamental inability of the 2D domain to capture the turbulent oscillations of the flame surface responsible for thermal intermittency.

The downstream stations ($y/D = 6.5$ and 8.5) exhibit dramatic differences between simulations and experimental data. All cases produce nearly negligible fluctuations ($c_{rms} < 10$), while experimental fluctuations reach $c_{rms} \approx 100$ with peaks at similar radial locations, indicating sustained intermittency as the flame brush continues to interact with ambient air entrainment. The uniformly poor performance of all three cases in capturing temperature fluctuations confirms that the 2D domain limitation dominates the fluctuation prediction, overwhelming any differences introduced by the sensor formulation or thickening factor.

5.1.3 Major Species Mass Fraction Profiles

The species mass fraction profiles provide direct validation of the TFM's chemical kinetics treatment and offer insight into the accuracy of different reaction pathways under turbulent conditions. Unlike velocity and temperature, which represent aggregate flow properties, individual species concentrations depend on the detailed balance of production and consumption through multiple elementary reactions. The ability of the TFM to accurately predict major species (reactants and primary products) and intermediate species (formed and consumed within the flame) thus constitutes a stringent test of the (E/F) modification applied to chemical

source terms. The comparison among the three cases further reveals how the spatial distribution of the thickening—controlled by the sensor—affects these delicate kinetic balances.

Figure 5.5 shows radial profiles of methane and oxygen mass fractions at four axial stations. The CH_4 distribution characterizes fuel consumption through the flame brush and mixing with the pilot stream, while O_2 depletion indicates the extent of combustion and the flame brush location.

The methane profiles (left column) reveal systematic differences in fuel consumption patterns among the three computational cases. At the first measurement station ($y/D = 2.5$), experimental data shows fresh fuel ($Y_{CH_4} \approx 5\%$) confined to a narrow core ($r/D < 0.5$) with rapid depletion by $r/D \approx 0.7$. Case 1 captures the core structure reasonably well, though fuel penetrates slightly further radially, with complete depletion occurring by $r/D \approx 0.8$. This moderate radial spreading reflects the enhanced molecular diffusivity introduced by the thickening transformation ($D_{\text{eff}} = EF \cdot D$), which operates throughout the computational domain despite the flame sensor's localization of the efficiency function.

Case 2 exhibits significantly broader fuel distribution, with $Y_{CH_4} \approx 4\%$ extending to $r/D \approx 0.9$. This excessive radial spreading is consistent with the higher thickening factor ($F_{\text{max}} = 13.0$) producing artificial diffusion that prevents proper fuel-oxidizer stratification. Case 3 shows greater persistence of methane in the jet core compared to both Case 1 and the experimental data. The fuel depletion rate is notably slower, particularly at downstream stations $y/D = 4.5$ and 6.5.

The effect compounds downstream: at $y/D = 4.5$ and 6.5, all cases progressively overpredict radial fuel spreading compared to experiments. Case 1 maintains qualitatively correct decay profiles but with flame brush widths approximately 20–30% larger than measured. Case 2 shows fuel consumption occurring over nearly twice the experimental radial extent, reflecting the fundamental breakdown of mixing physics when the thickened flame thickness exceeds the integral turbulent length scale ($\delta_{\text{TF}} \approx 5.5$ mm $> l_0$). Case 3's slower fuel consumption is consistent with its under-predicted temperature: the broader application of thickening by the temperature-based sensor reduces the effective reaction rate $(E/F)\dot{\omega}$ in regions where the sensor is only partially active, resulting in retarded combustion.

By the furthest downstream station ($y/D = 8.5$), experimental data shows nearly complete fuel consumption ($Y_{CH_4} < 0.5\%$) across the measurement domain. Case 1 approaches this behaviour with residual methane confined to $r/D < 0.4$, while Case 2 maintains elevated

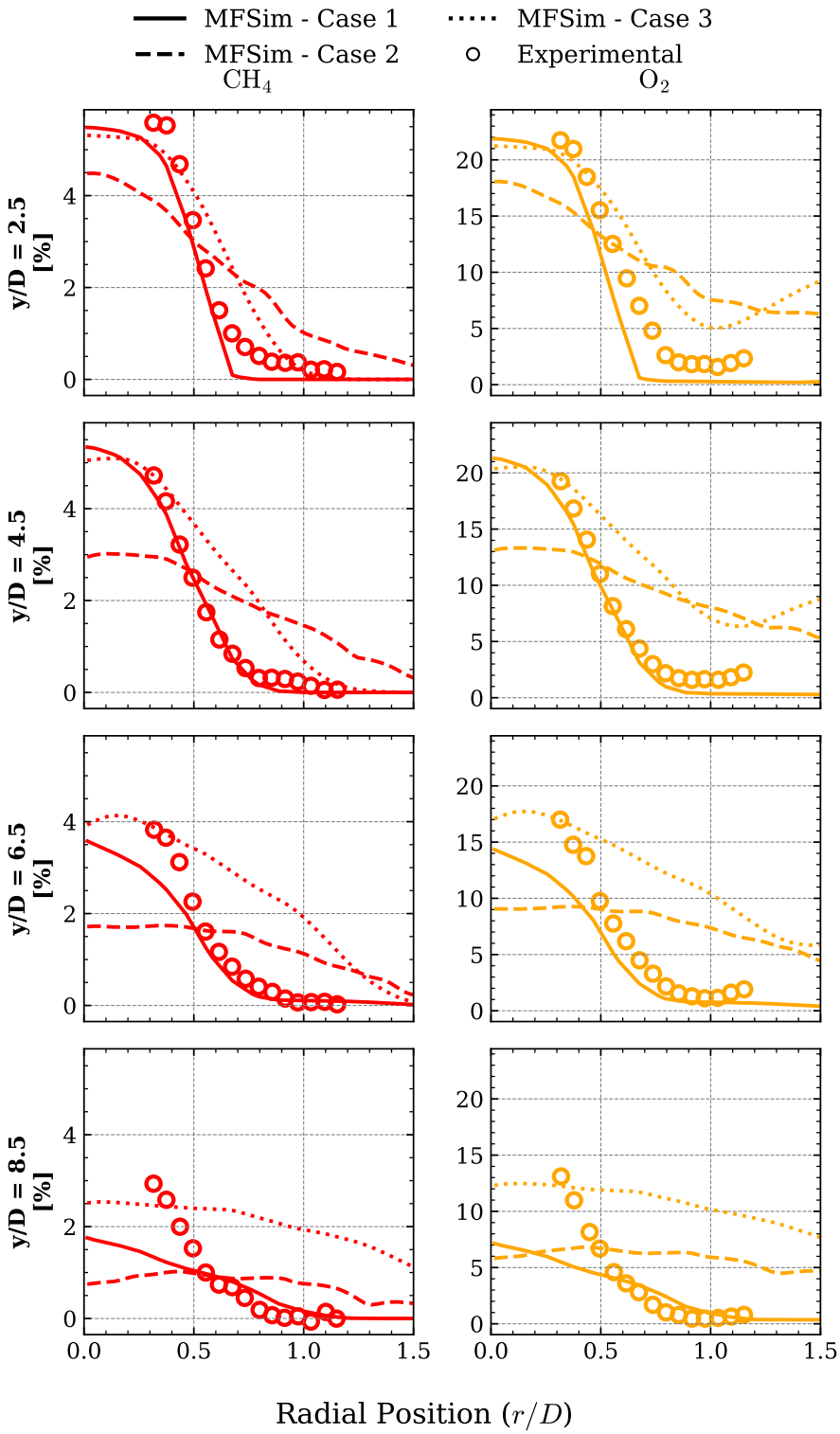

Figure 5.5: Radial profiles of mean methane (CH_4, left column) and oxygen (O_2, right column) mass fractions at axial stations $x/D = 2.5, 4.5, 6.5, 8.5$. Experimental data from Chen et al. (CHEN, Y.-C. et al., 1996) compared against three simulations.

fuel concentrations ($Y_{CH_4} \approx 1$–2%) across $r/D < 0.8$, indicating incomplete combustion from the artificially broadened and weakened reaction zone. Case 3 also retains more fuel than Case 1 at this station, further confirming the reduced combustion intensity associated with the temperature-based sensor.

The oxygen profiles (right column) track the inverse of methane consumption patterns. At $y/D = 2.5$, experimental data shows O_2 depletion beginning at $r/D \approx 0.4$, with minimum concentrations ($Y_{O_2} \approx 2\%$) marking the reaction zone location. Case 1 predicts the depletion onset location accurately but under-predicts the minimum oxygen concentration ($Y_{O_2} \approx 1\%$), suggesting locally stronger heat release or incomplete mixing. Case 2 shows a broader depletion zone with the minimum shifted to $r/D \approx 0.6$ and higher residual oxygen ($Y_{O_2} \approx 6\%$), consistent with the diluted reaction zone from excessive thickening. Case 3 exhibits slower O_2 depletion than Case 1, particularly at $y/D = 4.5$ and 6.5, consistent with the weaker combustion inferred from the temperature profiles.

The comparison between Cases 1 and 3 for reactant species isolates the sensor effect on fuel consumption. The Han sensor, by concentrating thickening only where the reaction is intense, preserves the local fuel consumption rate and maintains sharper gradients at the flame front. The Durand & Polifke sensor, by extending the thickening into preheat and post-flame zones, effectively weakens the reaction intensity in partially activated regions, producing a diffuse combustion front with retarded reactant depletion.

Figure 5.6 shows radial profiles of carbon dioxide and water vapour mass fractions. CO_2 formation indicates complete combustion of fuel carbon and marks the burnt gas region, while H_2O is the other major product species, with its distribution complementing the CO_2 profiles in characterizing combustion completion.

The carbon dioxide profiles (left column) reveal contrasting errors between the cases. Experimental data shows CO_2 production initiating in the flame brush region ($r/D \approx 0.5$) and reaching peak values ($Y_{CO_2} \approx 13$–14%) in the burnt gas region by $y/D = 4.5$. Case 1 anticipates CO_2 formation across all stations, with peak values similar to experimental data. This premature product formation corroborates the excessive heat release observed in the temperature profiles and suggests that the efficiency function parametrization ($\beta = 0.5$ in the saturated power-law model) may be over-compensating for lost flame surface area in this particular flow configuration.

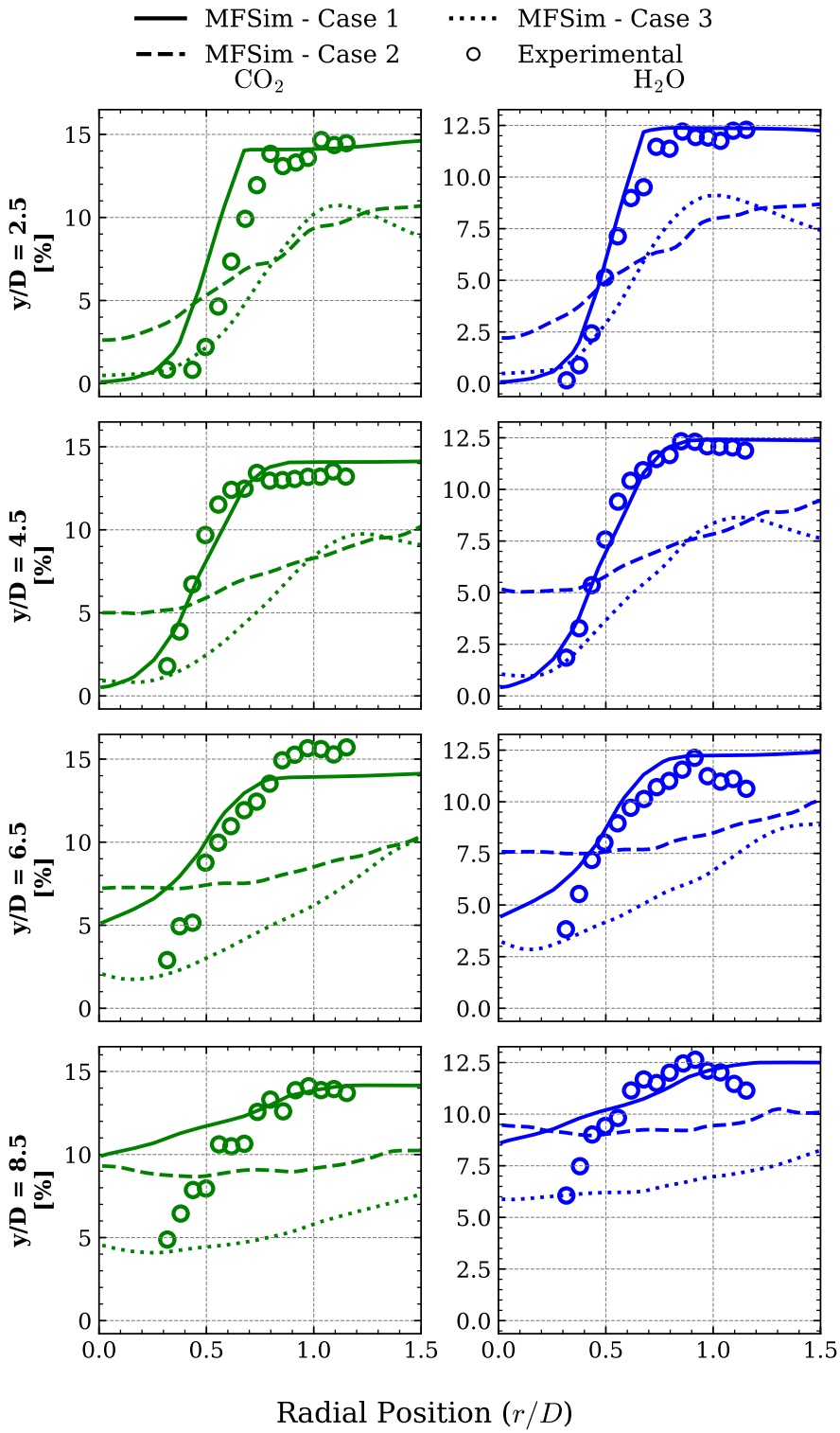

Figure 5.6: Radial profiles of mean carbon dioxide (CO_2, left column) and water vapour (H_2O, right column) mass fractions at axial stations $x/D = 2.5, 4.5, 6.5, 8.5$. Experimental data from Chen et al. (CHEN, Y.-C. et al., 1996) compared against three simulations.

Case 2 exhibits even stronger over-prediction at the near-field station ($Y_{CO_2} \approx 15\%$ at $y/D = 2.5$), and the broader spatial distribution brings the radial profile shape farther from experimental measurements at intermediate stations ($y/D = 4.5, 6.5$).

Case 3 under-predicts CO_2 formation systematically at all stations, with profiles lying below experimental values. The under-prediction is most pronounced in the inner region ($r/D < 0.5$), where Case 3 predicts product formation 40–50% below experimental measurements. This result directly confirms that the temperature-based sensor distributes the TFM effect in an excessively diffuse manner, compromising the local combustion intensity and retarding the conversion of reactants to products.

The water vapour profiles (right column) exhibit remarkably similar behaviour to CO_2. Case 1 accurately captures the overall profile at all stations, with premature appearance in the unburnt zone $r/D \leq 0.3$ at $y/D = 8.5$. Case 2 shows comparable under-prediction magnitudes in the burnt zone with over-prediction in the unburnt region. Case 3 consistently under-predicts H_2O formation, mirroring the CO_2 deficit and reinforcing the conclusion of globally weakened combustion.

A stoichiometric consistency check provides insight into the nature of these errors. For the global reaction $CH_4 + 2O_2 \rightarrow CO_2 + 2H_2O$, the mass ratio of products should be approximately $Y_{H_2O}/Y_{CO_2} \approx 0.82$. Examining the data at $y/D = 8.5$: experimental measurements yield $Y_{CO_2} \approx 14\%$ and $Y_{H_2O} \approx 12\%$, giving a ratio of approximately 0.86; Case 1 produces $Y_{CO_2} \approx 15\%$ and $Y_{H_2O} \approx 12.5\%$, yielding ratio ≈ 0.83; while Case 2 gives $Y_{CO_2} \approx 11\%$ but $Y_{H_2O} \approx 10\%$, producing ratio ≈ 0.71. The Case 2 ratio reveals that its combustion remains fundamentally incomplete despite elevated CO_2 levels, with deficit water production indicating either preferential hydrogen formation through chain-branching reactions or carbon monoxide accumulation, as discussed in the following paragraphs.

Figure 5.7 shows radial profiles of hydroxyl radical, carbon monoxide, and hydrogen mass fractions. The OH radical, with peak concentration typically located within the reaction zone, serves as a flame marker in experimental diagnostics and indicates the instantaneous position of the flame front. CO is an intermediate species whose distribution indicates incomplete combustion regions and provides insight into reaction zone structure, while H_2 appears as a product of fuel decomposition and participates in chain-branching reactions that sustain combustion.

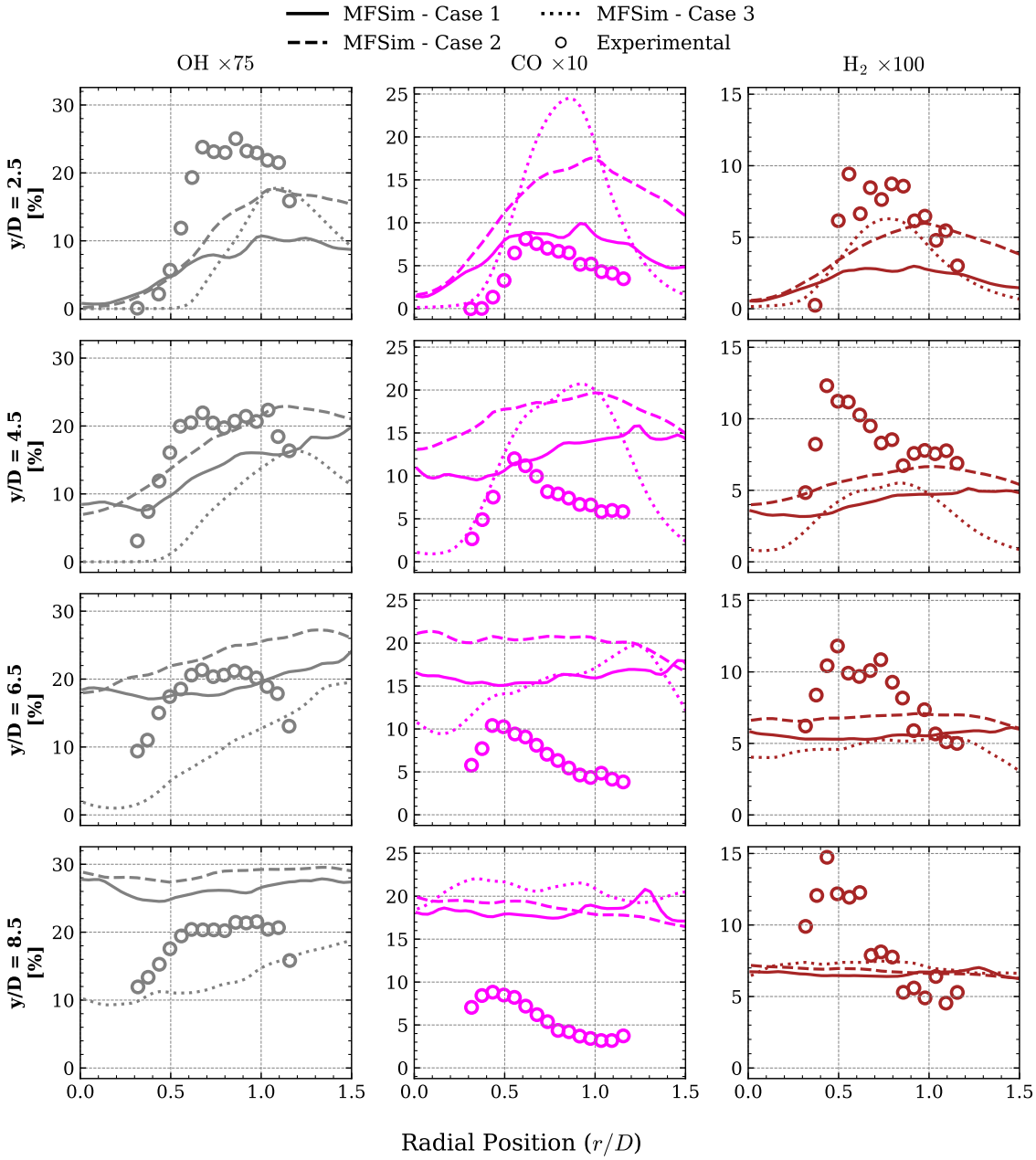

Figure 5.7: Radial profiles of mean hydroxyl radical (OH), carbon monoxide (CO) and hydrogen (H_2) mass fraction at axial stations $x/D = 2.5, 4.5, 6.5, 8.5$. Experimental data from Chen et al. (CHEN, Y.-C. et al., 1996) compared against three simulations.

The hydroxyl radical distribution (left column, note ×75 scaling) provides perhaps the most stringent test of the TFM's ability to preserve detailed chemical structure, as this radical exists only within the thin reaction layer where fast chain-branching occurs. At $y/D = 2.5$, experimental data shows a broad OH distribution with peak mass fraction $Y_{OH} \approx 0.003$ at $r/D \approx 0.7$, spanning the radial range $r/D = 0.4$–1.0. Case 1 under-predicts peak OH concentration by approximately 50% ($Y_{OH} \approx 0.0015$), with a narrower radial extent ($r/D = 0.5$–0.9). Case 2 shows good agreement of OH concentrations distributed across a broader region ($r/D = 0.4$–1.1), consistent with the diluted reaction zone from excessive thickening. Case 3 significantly under-predicts OH at all stations, consistent with the globally weaker combustion observed in the temperature and product species profiles.

At $y/D = 4.5$ and 6.5, Case 1 captures the radial profile qualitatively with under-predicted magnitudes approaching experimental data, while Case 2 correctly predicts the inner region $r/D < 0.8$ but slightly over-predicts OH concentration at the outer region. Case 3 remains systematically below both Cases 1 and 2 and the experimental measurements.

By $y/D = 8.5$, experiments show sustained OH production ($Y_{OH} \approx 0.002$) across $r/D = 0.6$–1.2, indicating continued reaction as the flame brush interacts with entrained air. Both Cases 1 and 2 over-predict this far-field OH concentration, particularly Case 2, which along with the temperature profile at this station suggests that reaction has spread into the far-field region. Case 3's continued under-prediction at this station is consistent with its generally weaker combustion.

The carbon monoxide profiles (middle column, note ×10 scaling) reveal complementary information about incomplete combustion and intermediate species formation. CO is produced during fuel pyrolysis and subsequently oxidized to CO_2 through the reaction CO + OH → CO_2 + H. At $y/D = 2.5$, experimental data shows moderate CO production ($Y_{CO} \approx 0.0007$) confined to the flame brush region ($r/D = 0.5$–0.9). Case 1 predicts comparable peak concentrations but with a broader distribution extending to $r/D \approx 1.0$, while Case 2 dramatically over-predicts CO by nearly 300% ($Y_{CO} \approx 0.002$), with a much broader spatial extent ($r/D = 0.3$–1.2). Case 3 produces lower CO values than Case 1 and below experimental values at the first two stations.

The downstream evolution of CO reveals fundamental differences among the cases. Experimental concentrations remain relatively constant or decrease slightly from $y/D = 4.5$ to 8.5, indicating gradual CO → CO_2 conversion as the burnt gases mix and equilibrate. Case 2 shows persistent CO accumulation, with concentrations approximately four times higher than

experimental values at $y/D = 6.5$, directly confirming incomplete combustion in the coarse-mesh case. Case 3 presents an interesting behaviour: while producing lower CO than Case 1 at the first two stations, it exhibits over-prediction at downstream stations ($y/D = 6.5$–8.5), suggesting incomplete combustion with delayed accumulation of intermediaries. This pattern—initial under-production followed by downstream accumulation—is consistent with the retarded combustion inferred from the temperature and major species profiles: the weakened reaction zone fails to fully oxidize CO to CO_2 within the flame brush, allowing CO to accumulate as it is transported downstream.

Case 1 maintains closer agreement at the first two stations but still over-predicts CO across the last two stations, indicating that even moderate thickening factors ($F_{\max} = 6.5$) introduce detectable perturbations to oxidation pathways.

The hydrogen profiles (right column, note ×100 scaling) complete the picture of intermediate species formation and radical pool dynamics. H_2 forms through fuel pyrolysis and participates in critical chain-branching reactions ($H_2 + O \rightarrow OH + H$) that sustain combustion. At $y/D = 2.5$, experimental measurements show H_2 production peaking near $r/D \approx 0.7$, co-located with the flame brush. Case 1 under-predicts peak hydrogen concentration, while Case 2 shows a similar profile to the experimental data. Case 3 exhibits general under-prediction consistent with its weaker combustion.

Downstream stations ($y/D = 4.5$–8.5) reveal that experimental hydrogen concentrations remain elevated throughout the measured domain, indicating sustained chain chemistry as the flame brush continues to propagate and interact with fresh oxidizer. All three computational cases under-predict these values at specific radial spans $r/D \approx 0.4$–0.7 by factors of 2–3, but show acceptable agreement at the outer radial span $r/D > 0.75$ beyond the experimental peak.

The comparison among the three cases for intermediate and radical species reveals the distinct signatures of each modelling configuration. Case 1 (Han sensor, moderate $F_{\max}$) preserves the local combustion intensity, producing reasonable major species but with systematic over-prediction of CO_2 and H_2O (10–15% at inner regions) and under-prediction of H_2 peaks, confirming partial depletion of the chain-branching radical pool. Case 2 (Han sensor, excessive $F_{\max}$) shows breakdown of turbulent mixing when $\delta_{\text{TF}} > l_0$, with CO and OH over-prediction revealing incomplete combustion pathways consistent with the heat accumulation observed across the domain in the temperature profiles. Case 3 (Durand & Polifke sensor, moderate $F_{\max}$) systematically under-predicts OH, CO_2, and H_2O while exhibiting delayed CO accumulation,

all consistent with a globally weakened combustion intensity that arises from the overly broad spatial distribution of the thickening.

Despite these limitations, the species profiles demonstrate that the TFM with the Han sensor and moderate thickening factors (Case 1: $F_{\max} = 6.5$, $\delta_{\mathrm{TF}} \approx 2.7$ mm $< l_0$) achieves acceptable engineering accuracy for major species predictions, with errors in reactant consumption and primary product formation remaining within acceptable thresholds of experimental values. This level of accuracy may be sufficient for applications focused on global combustion characteristics such as flame stabilization, heat release distribution, and combustor efficiency. However, the systematic over-prediction of minor species concentrations (OH, CO) indicates that the current TFM implementation should not be relied upon for emissions predictions or radical-dependent phenomena such as ignition, extinction, or pollutant formation without significant model refinement or coupling with tabulated chemistry approaches that can preserve detailed kinetic pathways independently of the flame thickening procedure.

The Case 3 results further demonstrate that the choice of flame sensor is as impactful as the choice of $F_{\max}$. For temperature and species predictions, Case 3 with $F_{\max} = 6.5$ produces results comparable to or worse than Case 2 with $F_{\max} = 13.0$ in several aspects, despite operating on a much finer grid. This finding has direct practical implications: for premixed combustion with detailed chemistry, reaction-rate-based sensors (such as the modified Han sensor) are preferable because they restrict the thickening to the chemically active zone, preserving the local intensity of heat release and species transformation.

5.1.4 Mean Species Field Distributions

The two-dimensional field distributions of time-averaged species mass fractions provide complementary information to the radial profiles, revealing the global flame structure and spatial organization of chemical reactions throughout the computational domain. While radial profiles extracted at discrete axial stations enable quantitative validation against experimental measurements, field visualizations offer qualitative insight into flame shape, symmetry, and the spatial extent of different chemical zones. The comparison among the three cases directly illustrates the impact of grid resolution, thickening factor, and sensor formulation on the resolved flame structure.

Figure 5.8 presents the time-averaged methane mass fraction field for both mesh configurations. The CH_4 distribution illustrates the fuel jet structure, its spreading downstream of the nozzle, and consumption through the flame brush.

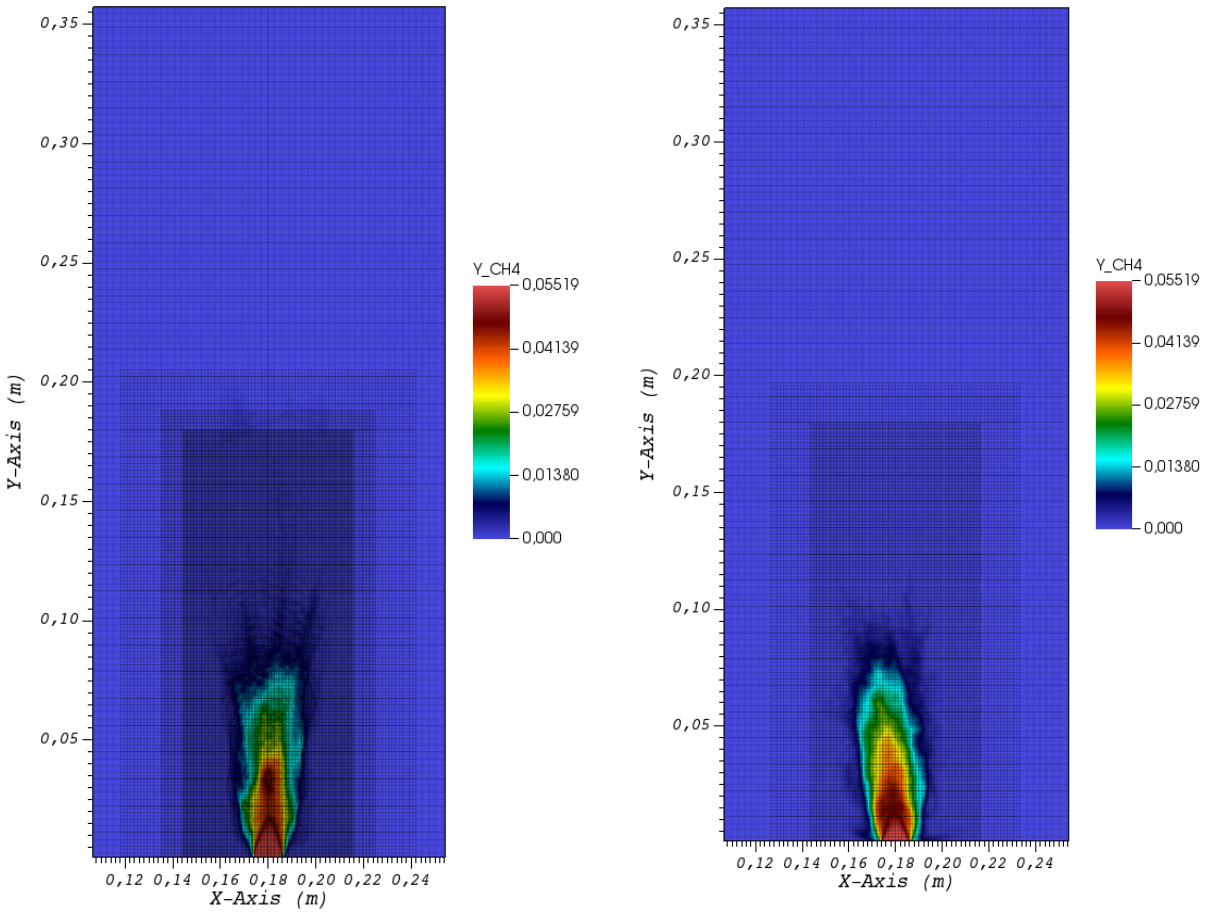

Figure 5.8: Time-averaged methane (CH_4) mass fraction field for Case 1 (production mesh, left) and Case 2 (coarse mesh, right). The field shows fuel jet structure and consumption through the flame brush.

Case 1 exhibits a well-defined, narrow fuel jet emerging from the nozzle with clear demarcation between the fuel-rich core and the surrounding oxidizer. The CH_4 consumption pattern develops gradually downstream, with the fuel jet penetrating to approximately $y/D \approx 15$ before complete consumption. The jet spreading is relatively symmetric with clear shear layer development at the jet boundaries.

In contrast, Case 2 shows a broader, more diffuse fuel jet structure, particularly evident in the near-field region ($y/D < 5$). The higher thickening factor artificially enhances the effective diffusion coefficients, leading to premature radial spreading of the methane before it reaches the reaction zone. Despite this, the fuel penetration depth is similar to that observed in Case 1. Additionally, the flame is visibly angled toward the left domain boundary in Case 2.

The comparison reveals a fundamental limitation of applying excessive thickening factors: the enhanced diffusion coefficients affect not only the flame zone but also upstream mixing regions where no chemical reactions occur. This non-local effect cannot be fully mitigated by the flame sensor, as the sensor activates thickening based on reaction progress but does not prevent the enhanced diffusivity from influencing adjacent non-reacting cells through the diffusion operator.

Figure 5.9 shows the time-averaged hydroxyl radical mass fraction field for Cases 1 and 2. The OH distribution serves as an excellent marker of the reaction zone, as hydroxyl radicals are produced and consumed primarily within the thin layer where active chemistry occurs.

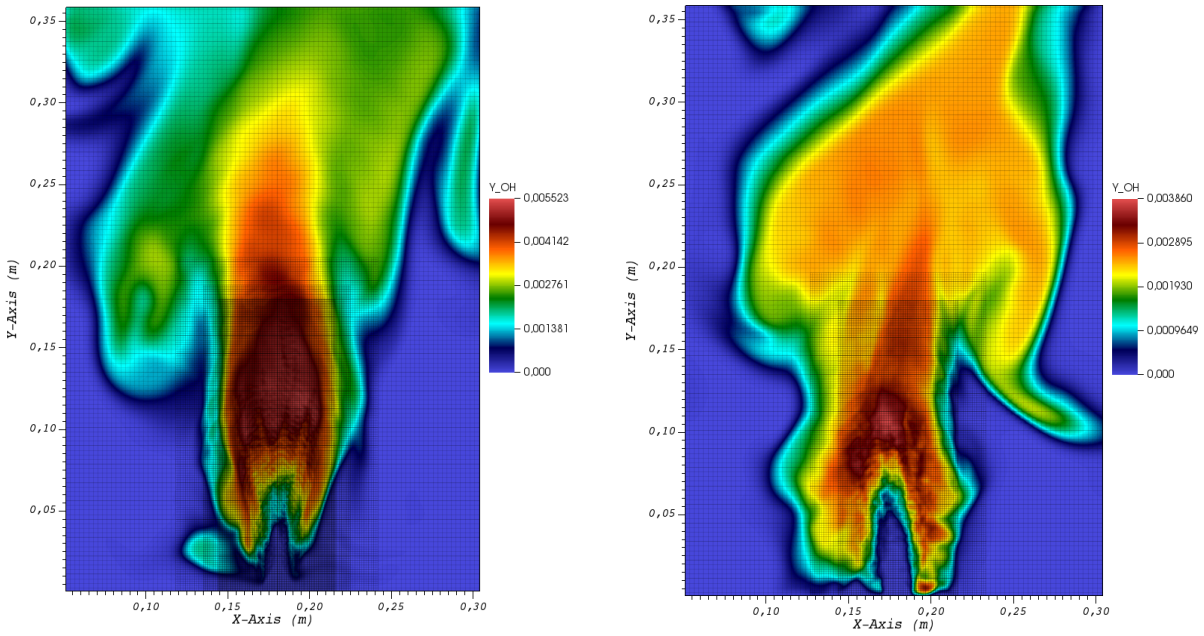

Figure 5.9: Time-averaged hydroxyl radical (OH) mass fraction field for Case 1 (production mesh, left) and Case 2 (coarse mesh, right). The OH distribution marks the flame front location and reaction zone structure.

Case 1 demonstrates a thin, well-defined OH layer that closely follows the stoichiometric surface where fuel and oxidizer meet in appropriate proportions. The flame front exhibits a visibly wrinkled structure, particularly in the region $5 < y/D < 15$, indicating that the grid resolution is sufficient to capture at least partially the large-scale turbulent distortions of the flame surface. Peak OH mass fractions reach approximately $Y_{\mathrm{OH}} \approx 0.005$, localized within a narrow band whose thickness is consistent with the expected reaction zone width for the applied thickening factor ($\delta_{\mathrm{TF}} \approx 2.7$ mm).

Case 2, in contrast, exhibits a markedly broader and more diffuse OH distribution. The reaction zone thickness is approximately twice that of Case 1, consistent with the ratio of

thickening factors. Peak OH concentrations are lower ($Y_{OH} \approx 0.004$) and distributed over a larger spatial volume. The flame contours appear smoother with reduced wrinkling, indicating that the coarser grid fails to resolve the turbulent eddies responsible for flame surface distortion.

The spatial extent of the OH field provides insight into global heat release distribution. In Case 1, OH is concentrated in a relatively narrow annular region, suggesting that combustion occurs in a well-defined flame brush separating reactants from products. In Case 2, the broader OH distribution indicates a more volumetrically distributed reaction zone, which, while preserving total heat release through the efficiency function correction, fundamentally alters the local thermochemical state and its coupling with the flow field. This broadening correlates with the over-prediction of mean temperature half-width observed in the radial profiles, as the artificially thickened reaction zone spreads thermal energy over a wider region than the physical flame would occupy.

All cases exhibit relatively symmetric flame structures, a direct consequence of the 2D computational domain assumption. The actual F3 flame is fully three-dimensional, with azimuthal instabilities and vortical structures that cannot be represented in the present 2D configuration. The flame fields shown here capture the streamwise-radial plane structure but miss the three-dimensional turbulent cascade and energy redistribution mechanisms that characterize real turbulent flames.

Despite these limitations, Case 1 demonstrates that the TFM can produce physically reasonable flame structures when applied with appropriate thickening factors respecting the criterion $\delta_{TF} < l_0$ and employing a reaction-rate-based sensor that confines the thickening to the chemically active zone. The field distributions confirm that the model preserves essential flame characteristics—localized reaction zones marked by OH, fuel consumption patterns consistent with turbulent mixing, and flame brush structures qualitatively similar to experimental observations—while enabling simulation on computationally affordable grids. Cases 2 and 3 serve as complementary cautionary examples: Case 2 demonstrates model breakdown under excessive thickening factor magnitude, while Case 3 illustrates the degradation that results from excessively broad sensor activation, even when the thickening factor and grid resolution are adequate. Together, they provide practical guidance for selecting appropriate grid resolutions, maximum thickening factors, and flame sensor formulations in industrial applications.

For completeness, instantaneous fields from the final simulated time step are presented in Appendix A to provide additional qualitative comparison of the instantaneous flame dynamics across the two first configurations.

5.1.5 Computational Performance

An essential consideration for practical application of the TFM to industrial combustion simulations is the computational cost relative to alternative modelling approaches and the trade-offs between accuracy and efficiency. This section quantifies the computational requirements of the present simulations and discusses the cost savings achieved through artificial thickening compared to hypothetical direct flame resolution.

Table 5.2 summarizes the computational resources and wall-clock times for the Bunsen flame simulations.

Table 5.2: Computational cost summary for turbulent Bunsen flame F3 simulations.

Parameter	**Case 1**	**Case 2**	**Case 3**
Base grid	128×128×1	128×128×1	128×128×1
AMR levels	5	4	5
Refinement ratio	2	2	2
Finest cell size [mm]	0.34	0.68	0.34
Total cells (time-averaged)	2.1×10^5	1.1×10^5	2.1×10^5
Time step [μs]	0.25	0.25	0.25
Physical time simulated [s]	0.05	0.1	—
MPI processes	64	32	64
Wall-clock time [hours]	180	120	—
Time per step [s]	5	2.3	—

Cases 1 and 3 share identical computational costs, as the sensor formulation does not introduce additional equations to solve or modify the AMR structure. The computational overhead of evaluating the Durand & Polifke sensor versus the modified Han sensor is negligible relative to the cost of the chemical source term evaluation and the linear solver. This observation is practically significant: the choice of sensor affects solution accuracy substantially (as demonstrated throughout this chapter) without measurable impact on computational cost, making sensor selection a zero-cost modelling decision that warrants careful consideration in any TFM application.

CONCLUSIONS AND FUTURE WORKS

This work presented the implementation, verification, and validation of the TFM framework within the MFSim computational platform for LES of turbulent premixed reactive flows. The work addressed the fundamental flame resolution problem in LES, where the laminar flame thickness is far smaller than affordable grid spacing, by artificially thickening the flame through simultaneous enhancement of diffusivities and reduction of reaction rates, preserving the laminar flame speed while rendering the flame structure resolvable on practical meshes.

The TFM module was implemented following a modular software architecture consistent with MFSim's Fortran 90/95 codebase, with C++ interfaces for Cantera integration providing access to detailed thermodynamic properties, transport coefficients, and chemical kinetics. The implementation encompasses the core TFM formulation, comprising the dynamic thickening transformation, the Wang-modified Charlette efficiency function with power-law exponent $\beta = 0.5$, and two flame sensor options: the Durand and Polifke parabolic sensor based on progress variable and the modified Han sensor based on fuel reaction rate. The module integrates with MFSim's existing infrastructure for IMEX time integration, Strang operator splitting for chemistry, the dynamic Smagorinsky subgrid-scale model, and block-structured adaptive mesh refinement. A key design choice ensures that the stiff ODE integrator (CVODE) always operates on unmodified chemical kinetics, with TFM modifications applied only to the source terms entering the transport equations, thereby preserving detailed balance and thermodynamic consistency.

Validation was conducted on the turbulent Bunsen Flame F3 from the experimental campaign of Chen et al. (CHEN, Y.-C. et al., 1996), a well-documented configuration operating in the flamelet regime at $\mathrm{Re}_D \approx 24{,}000$ with stoichiometric methane-air. Three configurations were investigated in a factorial design that enables independent assessment of the two principal modelling choices in the TFM framework: the thickening factor magnitude and the flame sensor formulation. Case 1 (production mesh, $\Delta x = 0.34$ mm, $F_{\max} = 6.5$, modified Han sensor) and Case 2 (coarse mesh, $\Delta x = 0.68$ mm, $F_{\max} = 13.0$, modified Han sensor) quantify

the effect of grid resolution and thickening factor, while Case 3 ($\Delta x = 0.34$ mm, $F_{\max} = 6.5$, Durand & Polifke sensor) isolates the influence of sensor formulation at identical mesh and thickening parameters. All simulations employed the Yang and Pope 16-species mechanism with mixture-averaged transport on a two-dimensional domain with spanwise periodicity, a simplification that proved to be a dominant source of discrepancy with respect to experimental measurements.

The mean velocity field was captured with reasonable accuracy by all three cases, confirming that the TFM transformation correctly preserves the integral effect of heat release on flow acceleration through the E/F scaling of reaction source terms. Case 1 reproduced the centreline velocity evolution within approximately 5–8% of experimental values, Case 2 exhibited slightly larger deviations in the far field, and Case 3 showed intermediate behaviour with over-prediction attributable to the broader spatial extent over which the temperature-based sensor applies the thickening. However, the turbulent kinetic energy profiles revealed significant sensitivity to both the thickening factor and the sensor formulation. Case 2 produced severe non-physical energy accumulation characteristic of two-dimensional turbulence, where the absence of vortex stretching prevents the forward energy cascade. Case 3 yielded kinetic energy values higher than Case 1 but substantially below the non-physical levels of Case 2, with the difference between Cases 1 and 3 directly quantifying the isolated effect of sensor choice on turbulence-flame coupling. Notably, Case 3's improved kinetic energy agreement with experimental data must be interpreted cautiously, as it likely results from error cancellation between the inherent 2D energy accumulation and the additional artificial dissipation introduced by the broader sensor activation, rather than from improved physical modelling.

The mean temperature profiles constituted the most critical differentiation among the three configurations. Case 1 captures the flame brush structure qualitatively, reaching normalised temperatures consistent with experimental trends at most axial stations, although with premature heat release in the near-nozzle region and excessive thermal accumulation at the centreline in the far field. Case 2 exhibited fundamentally different behaviour, producing nearly linear temperature profiles that lack the characteristic S-shaped structure of a turbulent flame brush. Case 3 revealed the most significant finding of the sensor comparison: it systematically under-predicted mean temperature at all stations, with values up to 50% below experimental measurements in the inner region at intermediate downstream stations. This under-prediction is directly attributable to the Durand & Polifke sensor's broader activation region, which

encompasses the entire thermal transition zone—including preheat and post-flame regions—rather than only the chemically active layer targeted by the Han sensor. The resulting dilution of heat release over an excessively large volume weakens the local combustion intensity and retards heating of the jet core. Temperature fluctuations were systematically under-predicted by all three cases, reflecting the inability of the quasi-two-dimensional domain to sustain the azimuthal instabilities and three-dimensional turbulent transport responsible for flame brush intermittency. This uniformly poor fluctuation prediction, independent of sensor or thickening factor, confirms the 2D domain limitation as the dominant factor for unsteady thermal quantities.

Major species predictions provided further differentiation among the three configurations. Case 1 reproduced methane consumption and oxygen depletion patterns with radial profile shapes broadly consistent with experiments. Carbon dioxide and water vapour profiles showed good agreement in magnitude, with stoichiometric consistency maintained ($Y_{H_2O}/Y_{CO_2} \approx 0.83$ versus the experimental value of 0.86). Case 2 exhibited significantly broader species distributions, incomplete combustion evidenced by persistent CO accumulation at concentrations approximately four times higher than experimental values, and a breakdown of stoichiometric consistency ($Y_{H_2O}/Y_{CO_2} \approx 0.71$). Case 3 exhibited a distinct error pattern: systematic under-prediction of CO_2 and H_2O formation (40–50% below experimental values in the inner region), greater persistence of fuel in the jet core, and slower oxygen depletion—all consistent with globally weakened combustion. The CO profiles of Case 3 revealed an instructive pattern of initial under-production at upstream stations followed by over-prediction downstream, indicating that the weakened reaction zone fails to fully oxidize CO to CO_2 within the flame brush, allowing intermediates to accumulate as they are transported downstream.

Intermediate species (OH, CO, H_2) proved more sensitive to model parameters across all configurations. Case 1 under-predicted peak OH concentrations by approximately 50% at the first measurement station while approaching experimental values further downstream. Case 3 systematically under-predicted OH, CO_2, and H_2O while exhibiting delayed CO accumulation, all signatures of diluted radical concentrations resulting from the overly broad spatial distribution of the thickening. Case 2 showed CO and OH over-prediction revealing incomplete combustion pathways consistent with the heat accumulation observed across the domain. These results demonstrate that the single-parameter efficiency function approach introduces distinct

perturbation signatures depending on whether the dominant error source is excessive thickening magnitude (Case 2) or excessive thickening spatial extent (Case 3).

The two-dimensional field distributions of time-averaged species mass fractions corroborated the quantitative findings. Case 1 produced a thin, well-defined OH layer closely following the stoichiometric surface with visible flame wrinkling, while Case 2 exhibited a broader, smoother reaction zone with reduced wrinkling, consistent with the thickened flame thickness exceeding the integral turbulent length scale ($\delta_{\mathrm{TF}} \approx 5.5$ mm $> l_0 \approx 3.6$ mm). Case 3's instantaneous fields showed a flame front less sharply defined than Case 1 despite sharing the same mesh, with broader fuel jet structure and more gradual transitions between reactants and products. This comparison established the practical criterion $\delta_{\mathrm{TF}} < l_0$ as necessary but not sufficient for maintaining physically meaningful turbulence-flame coupling: sensor selectivity must also confine the thickening to the chemically active zone.

A central conclusion of this work is that the choice of flame sensor is as impactful on solution accuracy as the choice of maximum thickening factor. For temperature and species predictions, Case 3 with $F_{\max} = 6.5$ on the production mesh produced results comparable to or worse than Case 2 with $F_{\max} = 13.0$ on the coarse mesh in several respects, despite operating at twice the grid resolution. Since the sensor formulation introduces no additional computational cost—the evaluation overhead is negligible relative to chemistry and linear solver operations—sensor selection constitutes a zero-cost modelling decision with first-order effects on predictive accuracy. For premixed combustion with detailed chemistry, reaction-rate-based sensors such as the modified Han sensor are recommended, as they restrict the thickening to the chemically active zone, preserving the local intensity of heat release and species transformation.

The computational performance analysis confirmed the practical viability of the TFM approach. The algebraic nature of the TFM operations introduces negligible overhead (less than 5% of total wall-clock time), with the primary benefit residing in the enabling of significantly coarser grids compared to direct flame resolution. The production mesh simulation (Case 1) required 180 hours on 64 MPI processes for 0.05 s of physical time, while the coarse mesh (Case 2) required 120 hours on 32 processes for 0.1 s, demonstrating the substantial cost reduction achievable through coarser discretisation, albeit at the expense of predictive accuracy when the thickening factor becomes excessive.

The results collectively demonstrate that the TFM implementation in MFSim achieves acceptable engineering accuracy for mean flow and major species predictions when operated with moderate thickening factors that respect the scale separation criterion $\delta_{\mathrm{TF}} < l_0$ and when combined with a reaction-rate-based flame sensor that confines the thickening to chemically active regions. The dominant source of discrepancy in the present validation campaign is attributed to the two-dimensional domain assumption rather than to deficiencies in the TFM formulation itself. This conclusion is supported by the observation that all three cases exhibit similar qualitative limitations—suppressed radial spreading, under-predicted temperature fluctuations, and non-physical kinetic energy accumulation—that are characteristic of two-dimensional turbulence regardless of the combustion model configuration employed. The sensor comparison, by demonstrating that a physically sound formulation can be degraded by an inappropriate activation criterion at identical resolution and thickening parameters, provides an additional dimension of model assessment that goes beyond the traditional resolution-convergence approach.

This work contributes to the broader development of MFSim's reactive flow capabilities by complementing the existing LES/PDF hybrid framework, the AMR infrastructure with detailed chemistry, the virtual kinetic mechanism methodology, and the compressible reactive flow solver with an algebraic combustion closure that offers a favourable balance between computational efficiency and physical fidelity for premixed turbulent combustion in the flamelet and thin reaction zones regimes.

Recommendations for Future Work

The findings and limitations identified in this dissertation suggest several directions for continued development, organised by estimated time frame and complexity.

In the short term, the most impactful improvement would be the extension to fully three-dimensional simulations of the Flame F3 configuration, which would eliminate the dominant source of discrepancy identified in this work and enable a more rigorous assessment of the TFM formulation independent of geometric simplifications. The existing AMR infrastructure in MFSim is well-suited for this extension, as refinement can concentrate computational resources near the flame while maintaining coarser resolution in the bulk flow. Additionally, a systematic parametric study of the efficiency function exponent β and the sensor threshold Ω_0

for the F3 configuration would establish sensitivity bounds and potentially improve agreement with experimental intermediate species profiles. The implementation of the Colin efficiency function as an alternative to the Wang-modified Charlette formulation would provide a complementary modelling option and enable direct comparison of wrinkling factor predictions. Furthermore, given the significant impact of sensor selection demonstrated in this work, a more comprehensive evaluation of flame sensor formulations—including hybrid sensors that combine reaction-rate and progress-variable criteria—would be valuable for establishing best-practice guidelines across different combustion regimes.

In the medium term, the extension to non-premixed and partially premixed combustion represents a natural progression. The theoretical framework for mixture-fraction-based flame sensors has been presented in this dissertation, and the modular implementation architecture facilitates the addition of new sensor formulations. Validation against canonical non-premixed flames (such as the Sandia Flame D, for which MFSim already has established simulation experience) and partially premixed configurations (such as the Sydney piloted flames) would broaden the range of applicability. The coupling of TFM with tabulated chemistry approaches (FGM or FPV) is another medium-term objective that would reduce computational cost while preserving access to detailed thermochemical state information, enabling application to larger-scale configurations with complex fuel compositions relevant to industrial settings.

In the longer term, application to industrially relevant geometries—including gas turbine combustors, industrial flares, and process heaters—would fulfil the original motivation of this research programme. Such applications would require the combined use of TFM with AMR, multi-regime flame sensors, and potentially the compressible solver developed by Chiumento (CHIUMENTO, 2024) for configurations where acoustic coupling is significant. The prediction of thermoacoustic instabilities, which require accurate unsteady heat release coupled with acoustic modes, represents a particularly challenging and high-value application of the TFM-LES framework. Finally, the integration of emissions sub-models for NO_x and CO prediction, building upon the virtual kinetic mechanism methodology developed by Elias (ELIAS, 2023), would extend the practical utility of the tool for environmental compliance assessment in industrial combustion systems.

BIBLIOGRAPHY

ASCHER, U. M.; RUUTH, S. J.; SPITERI, R. J. Implicit-explicit Runge-Kutta methods for time-dependent partial differential equations. **Applied Numerical Mathematics**, v. 25, n. 2–3, p. 151–167, 1997. DOI: 10.1016/S0168-9274(97)00056-1.

AUZILLON, P. et al. Numerical investigation of thickened flame and filtered tabulated chemistry modeling approaches in LES of premixed combustion. In: PROCEEDINGS of the Combustion Institute. [S.l.: s.n.], 2011. v. 33, p. 1331–1338. DOI: 10.1016/j.proci.2010.05.018.

BARBI, F. et al. Numerical experiments of ascending bubbles for fluid dynamic force calculations. **Journal of the Brazilian Society of Mechanical Sciences and Engineering**, v. 40, n. 11, p. 519, 2018. DOI: 10.1007/s40430-018-1435-7.

BIRD, R. B.; STEWART, W. E.; LIGHTFOOT, E. N. **Transport Phenomena**. 2nd. New York: John Wiley & Sons, 2002.

BOGER, M.; VEYNANTE, D.; BOUGHANEM, H.; TROUVÉ, A. Direct numerical simulation analysis of flame surface density concept for large eddy simulation of turbulent premixed combustion. **Symposium (International) on Combustion**, v. 27, n. 1, p. 917–925, 1998. DOI: 10.1016/S0082-0784(98)80489-X.

BORGHI, R. On the structure and morphology of turbulent premixed flames. In: RECENT Advances in the Aerospace Sciences. [S.l.]: Springer, 1985. P. 117–138. DOI: 10.1007/978-1-4684-4298-4_7.

BURKE, S. P.; SCHUMANN, T. E. W. Diffusion flames. **Industrial & Engineering Chemistry**, v. 20, n. 10, p. 998–1004, 1928. DOI: 10.1021/ie50226a005.

BUTLER, T. D.; O'ROURKE, P. J. A numerical method for two dimensional unsteady reacting flows. In: 1. SYMPOSIUM (International) on Combustion. [S.l.: s.n.], 1977. v. 16, p. 1503–1515. DOI: 10.1016/S0082-0784(77)80432-3.

CASTRO, L. P. d.; SANTOS, J. G. d. F.; VEDOVOTO, J. M.; SILVEIRA-NETO, A. Implementation of a hybrid Lagrangian filtered density function-large eddy simulation methodology in a dynamic adaptive mesh refinement environment. **Physics of Fluids**, v. 33, n. 4, p. 045126, 2021. DOI: 10.1063/5.0045873.

CERFACS. **Activity report of the Parallel Algorithms project at CERFACS**. [S.l.: s.n.], 2026.

CHARLETTE, F.; MENEVEAU, C.; VEYNANTE, D. A power-law flame wrinkling model for LES of premixed turbulent combustion Part I: non-dynamic formulation and initial tests. **Combustion and Flame**, v. 131, n. 1–2, p. 159–180, 2002. DOI: 10.1016/S0010-2180(02)00400-5.

CHARLETTE, F.; MENEVEAU, C.; VEYNANTE, D. A power-law flame wrinkling model for LES of premixed turbulent combustion Part II: dynamic formulation. **Combustion and Flame**, v. 131, n. 1–2, p. 181–197, 2002. DOI: 10.1016/S0010-2180(02)00401-7.

CHEN, J. H. et al. Terascale direct numerical simulations of turbulent combustion using S3D. **Computational Science & Discovery**, v. 2, n. 1, p. 015001, 2009. DOI: 10.1088/1749-4699/2/1/015001.

CHEN, Y.-C. et al. The detailed flame structure of highly stretched turbulent premixed methane-air flames. **Combustion and Flame**, v. 107, n. 3, p. 223–244, 1996. DOI: 10.1016/S0010-2180(96)00070-3.

CHIUMENTO, V. H. **Modelagem Computacional de Escoamentos Reativos Compressíveis**. 2024. Ph.D. Thesis – Universidade Federal de Uberlândia, Uberlândia, Brazil.

COFFEE, T. P.; HEIMERL, J. M. Transport algorithms for premixed, laminar steady-state flames. **Combustion and Flame**, v. 43, p. 273–289, 1981. DOI: 10.1016/0010-2180(81)90027-4.

COLIN, O.; DUCROS, F.; VEYNANTE, D.; POINSOT, T. A thickened flame model for large eddy simulations of turbulent premixed combustion. **Physics of Fluids**, v. 12, n. 7, p. 1843–1863, 2000. DOI: 10.1063/1.870436.

COLUCCI, P. J.; JABERI, F. A.; GIVI, P.; POPE, S. B. Filtered density function for large eddy simulation of turbulent reacting flows. **Physics of Fluids**, v. 10, n. 2, p. 499–515, 1998. DOI: 10.1063/1.869537.

CUENOT, B.; SHUM-KIVAN, F.; BLANCHARD, S. On the thickening of diffusion flames. **Combustion and Flame**, v. 239, p. 111702, 2022. DOI: 10.1016/j.combustflame.2022.111702.

DAI, T. et al. Development of a new dynamic Smagorinsky model by an artificial neural network for prediction of outdoor airflow and pollutant dispersion. **Building and Environment**, v. 238, p. 110343, 2023. DOI: 10.1016/j.buildenv.2023.110343.

DAMASCENO, M. M. R. **Desenvolvimento de uma modelagem para escoamentos reativos em malhas adaptativas do tipo bloco-estruturada**. 2018. Ph.D. Thesis – Universidade Federal de Uberlândia, Uberlândia, Brazil.

DAMASCENO, M. M. R.; SANTOS, J. G. d. F.; VEDOVOTO, J. M. Simulation of turbulent reactive flows using a FDF methodology – advances in particle density control for normalized variables. **Computers & Fluids**, v. 170, p. 128–140, 2018. DOI: 10.1016/j.compfluid.2018.05.004.

DAMASCENO, M. M. R.; VEDOVOTO, J. M.; SILVEIRA-NETO, A. Turbulent inlet conditions modeling using large-eddy simulations. **CMES – Computer Modeling in Engineering and Sciences**, v. 104, p. 105–132, 2015. DOI: 10.3970/cmes.2015.104.105.

DE, A.; ACHARYA, S. Large Eddy Simulation of a Premixed Bunsen Flame Using a Modified Thickened-Flame Model at Two Reynolds Numbers. **Combustion Science and Technology**, v. 181, n. 10, p. 1231–1272, 2009. DOI: 10.1080/00102200903076266.

DE, A.; ACHARYA, S. Large Eddy Simulation of Premixed Combustion With a Thickened-Flame Approach. **Journal of Engineering for Gas Turbines and Power**, v. 131, n. 6, p. 061501, 2009. DOI: 10.1115/1.3094021.

DE TOMASO, L.; RIBER, E.; CUENOT, B. The Stretched-Thickened Flame model for turbulent premixed combustion. **Combustion and Flame**, v. 257, p. 112952, 2023. DOI: 10.1016/j.combustflame.2023.112952.

DRESSLER, L.; SACOMANO FILHO, F. L.; SADIKI, A.; JANICKA, J. Large eddy simulation of turbulent spray combustion using the ATF-FGM approach. **Flow, Turbulence and Combustion**, v. 106, p. 419–451, 2021. DOI: 10.1007/s10494-020-00178-2.

DURAND, L.; POLIFKE, W. Implementation of the thickened flame model for large eddy simulation of turbulent premixed combustion in a commercial solver. In: PROCEEDINGS of ASME Turbo Expo 2007. Montreal, Canada: [s.n.], 2007. ASME Paper GT2007-28188. DOI: 10.1115/GT2007-28188.

ELIAS, A. J. **Mecanismos Virtuais de Cinética Química aplicados à Modelagem de Misturas Complexas de Combustíveis Gasosos**. 2023. Ph.D. Thesis – Universidade Federal de Uberlândia, Uberlândia, Brazil.

ELIAS, A. J. **Modelagem híbrida URANS-LES para escoamentos turbulentos**. 2018. Master's Dissertation – Universidade Federal de Uberlândia, Uberlândia, Brazil. DOI: 10.14393/ufu.di.2018.1219.

GERMANO, M.; PIOMELLI, U.; MOIN, P.; CABOT, W. H. A dynamic subgrid-scale eddy viscosity model. **Physics of Fluids A: Fluid Dynamics**, v. 3, n. 7, p. 1760–1765, 1991. DOI: 10.1063/1.857955.

GHOBRIAL, N. et al. Evaluation of six subgrid-scale models for LES of wind farms in stable and conventionally-neutral atmospheric stratification. **Boundary-Layer Meteorology**, 2025.

GOODWIN, D. G.; MOFFAT, H. K.; SPETH, R. L. **Cantera: An object-oriented software toolkit for chemical kinetics, thermodynamics, and transport processes**. [S.l.: s.n.], 2009. https://www.cantera.org. Version 2.5.0.

GOULDIN, F. C. An application of fractals to modeling premixed turbulent flames. **Combustion and Flame**, v. 68, n. 3, p. 249–266, 1987. DOI: 10.1016/0010-2180(87)90003-4.

HAN, W. et al. Large eddy simulation/dynamic thickened flame modeling of a high Karlovitz number turbulent premixed jet flame. **Proceedings of the Combustion Institute**, v. 37, n. 2, p. 2555–2563, 2019. DOI: 10.1016/j.proci.2018.06.228.

HASTI, V. R.; KUMAR, G.; DRENNAN, S. A.; GORE, J. P. Modeling and Simulation of Bluff Body Stabilized Turbulent Premixed Flames. In: 54TH AIAA Aerospace Sciences Meeting. [S.l.: s.n.], 2016. DOI: 10.2514/6.2016-1383.

HAWKES, E. R.; CANT, R. S. A flame surface density approach to large-eddy simulation of premixed turbulent combustion. **Proceedings of the Combustion Institute**, v. 28, n. 1, p. 51–58, 2000. DOI: 10.1016/S0082-0784(00)80194-0.

HAWORTH, D. C. Progress in probability density function methods for turbulent reacting flows. **Progress in Energy and Combustion Science**, v. 36, n. 2, p. 168–259, 2010. DOI: 10.1016/j.pecs.2009.09.003.

HINDMARSH, A. C. et al. SUNDIALS: Suite of nonlinear and differential/algebraic equation solvers. **ACM Transactions on Mathematical Software**, v. 31, n. 3, p. 363–396, 2005. DOI: 10.1145/1089014.1089020.

HIRSCHFELDER, J. O.; CURTISS, C. F.; BIRD, R. B. **Molecular Theory of Gases and Liquids**. 2nd. New York: John Wiley & Sons, 1964.

KEE, R. J.; COLTRIN, M. E.; GLARBORG, P. **Chemically Reacting Flow: Theory and Practice**. 1st. Hoboken, NJ: John Wiley & Sons, 2003. ISBN 978-0471261797.

LAPEYRE, C. J. et al. Training convolutional neural networks to estimate turbulent sub-grid scale reaction rates. **Combustion and Flame**, v. 203, p. 73–82, 2019. DOI: 10.1016/j.combustflame.2019.02.019.

LAW, C. K. **Combustion Physics**. Cambridge, UK: Cambridge University Press, 2010. ISBN 978-0521154215.

LEGIER, J.-P.; POINSOT, T.; VEYNANTE, D. Dynamically thickened flame LES model for premixed and non-premixed turbulent combustion. In: CENTER FOR TURBULENCE RESEARCH, STANFORD UNIVERSITY. PROCEEDINGS of the Summer Program. Stanford, CA: [s.n.], 2000. P. 157–168.

LIEUWEN, T. C.; YANG, V. **Combustion Instabilities in Gas Turbine Engines: Operational Experience, Fundamental Mechanisms, and Modeling**. Reston, VA: American Institute of Aeronautics and Astronautics, 2005. v. 210. (Progress in Astronautics and Aeronautics). ISBN 978-1563476693.

LILLY, D. K. A proposed modification of the Germano subgrid-scale closure method. **Physics of Fluids A: Fluid Dynamics**, v. 4, n. 3, p. 633–635, 1992. DOI: 10.1063/1.858280.

LOMADA, S.; PFITZNER, M.; KLEIN, M. Comparison of Flame Surface Density and Artificially Thickened Flame Models for Large Eddy Simulation of Turbulent Premixed Combustion. **Flow, Turbulence and Combustion**, v. 112, p. 729–750, 2024. DOI: 10.1007/s10494-023-00510-0.

LUND, T. S. The use of explicit filters in large eddy simulation. **Computers & Mathematics with Applications**, v. 46, n. 4, p. 603–616, 2003. DOI: 10.1016/S0898-1221(03)90019-8.

MARCHAL, T. **Extension of the Spectral Difference method to laminar and turbulent combustion**. 2023. Ph.D. Thesis – Université de Toulouse.

MARTINI, J. E. F. **Modelagem Computacional de Escoamentos Turbulentos em Turbinas Eólicas Utilizando Fronteira Imersa e Refinamento Adaptativo da Malha**. 2021. Master's Dissertation – Federal University of Uberlândia, Uberlândia, Brazil. DOI: 10.14393/ufu.di.2021.455.

MELO, R. R. S. **Modelagem e simulação de escoamentos turbulentos com efeitos térmicos, utilizando a metodologia de fronteira imersa e malha adaptativa**. 2017. Ph.D. Thesis – Universidade Federal de Uberlândia, Uberlândia, Brazil.

MOSER, R. D.; HAERING, S. W.; YALLA, G. R. Statistical properties of subgrid-scale turbulence models. **Annual Review of Fluid Mechanics**, v. 53, p. 255–286, 2021. DOI: 10.1146/annurev-fluid-060420-023735.

MOTA, P. H. A. **Modelagem numérico-computacional multiníveis de processos de corrosão em sistemas fluidodinâmicos**. 2023. Ph.D. Thesis – Federal University of Uberlândia, Uberlândia, Brazil.

MOUREAU, V.; DOMINGO, P.; VERVISCH, L. Design of a massively parallel CFD code for complex geometries. **Comptes Rendus Mécanique**, v. 339, n. 2–3, p. 141–148, 2011. DOI: 10.1016/j.crme.2010.12.001.

MULI, M. M. **Implementation of the Thickened Flame Model for turbulent premixed and non-premixed combustion in OpenFOAM**. 2024. Master Thesis – Politecnico di Milano.

NONAKA, I. T. **Modeling and simulation of multicomponent evaporative sprays in generic conditions**. 2025. Master's Dissertation – Universidade Federal de Uberlândia, Uberlândia, Brazil.

OIJEN, J. A. van; GOEY, L. P. H. de. Modelling of premixed laminar flames using flamelet-generated manifolds. **Combustion Science and Technology**, v. 161, n. 1, p. 113–137, 2000. DOI: 10.1080/00102200008935814.

OLIVEIRA, G. S. d. **Implementation of numerical-computational tools for fluid-structure interaction analysis in industrial cases**. 2025. Master's Dissertation – Federal University of Uberlândia, Uberlândia, MG, Brazil.

PAKZAD, A. Damping functions correct over-dissipation of the Smagorinsky model. **Mathematical Methods in the Applied Sciences**, v. 40, n. 16, p. 5933–5944, 2017. DOI: 10.1002/mma.4444.

PETERS, N. Laminar diffusion flamelet models in non-premixed turbulent combustion. **Progress in Energy and Combustion Science**, v. 10, n. 3, p. 319–339, 1984. DOI: 10.1016/0360-1285(84)90114-X.

PETERS, N. Laminar flamelet concepts in turbulent combustion. **Symposium (International) on Combustion**, v. 21, n. 1, p. 1231–1250, 1988. DOI: 10.1016/S0082-0784(88)80355-2.

PETERS, N. **Turbulent Combustion**. Cambridge, UK: Cambridge University Press, 2000. ISBN 978-0521660822.

PIERCE, C. D.; MOIN, P. Progress-variable approach for large-eddy simulation of non-premixed turbulent combustion. **Journal of Fluid Mechanics**, v. 504, p. 73–97, 2004. DOI: 10.1017/S0022112004008213.

PINHEIRO, A. P. et al. Modelling of aviation kerosene droplet heating and evaporation using complete fuel composition and surrogates. **Fuel**, v. 305, p. 121564, 2021. DOI: 10.1016/j.fuel.2021.121564.

PIOMELLI, U.; CABOT, W. H.; MOIN, P.; LEE, S. Subgrid-scale backscatter in turbulent and transitional flows. **Physics of Fluids A: Fluid Dynamics**, v. 3, n. 7, p. 1766–1771, 1991. DOI: 10.1063/1.857956.

PITSCH, H. Large-eddy simulation of turbulent combustion. **Annual Review of Fluid Mechanics**, v. 38, p. 453–482, 2006. DOI: 10.1146/annurev.fluid.38.050304.092133.

PIVELLO, M. R. et al. A fully adaptive front tracking method for the simulation of two phase flows. **International Journal of Multiphase Flow**, v. 58, p. 72–82, 2014. DOI: 10.1016/j.ijmultiphaseflow.2013.08.009.

POINSOT, T. Prediction and control of combustion instabilities in real engines. **Proceedings of the Combustion Institute**, v. 36, n. 1, p. 1–28, 2017. DOI: 10.1016/j.proci.2016.05.007.

POINSOT, T.; VEYNANTE, D. **Theoretical and Numerical Combustion**. 2nd. Philadelphia: R.T. Edwards, Inc., 2005. ISBN 978-1930217102.

POPE, S. B. Computations of turbulent combustion: Progress and challenges. In: PROCEEDINGS of the Combustion Institute. [S.l.: s.n.], 1990. v. 23, p. 591–612. DOI: 10.1016/S0082-0784(06)80307-3.

POPE, S. B. PDF methods for turbulent reactive flows. **Progress in Energy and Combustion Science**, v. 11, n. 2, p. 119–192, 1985. DOI: 10.1016/0360-1285(85)90002-4.

POPE, S. B. Ten questions concerning the large-eddy simulation of turbulent flows. **New Journal of Physics**, v. 6, n. 1, p. 35, 2004. DOI: 10.1088/1367-2630/6/1/035.

POPE, S. B. **Turbulent Flows**. Cambridge, UK: Cambridge University Press, 2000. ISBN 978-0521598866.

PROCH, F.; KEMPF, A. M. Modeling heat loss effects in the large eddy simulation of a model gas turbine combustor with premixed flamelet generated manifolds. **Combustion and Flame**, v. 161, n. 10, p. 2627–2646, 2014. DOI: 10.1016/j.combustflame.2014.04.007.

QUILLATRE, P. **Simulation aux grandes échelles de la combustion turbulente prémélangée avec modèles de flamme épaissie**. 2014. Ph.D. Thesis – INSA de Rouen.

RATHORE, O.; NAVARRO-MARTINEZ, S. Flame Dynamics Modelling Using Artificially Thickened Models. **Flow, Turbulence and Combustion**, v. 111, p. 897–927, 2023. DOI: 10.1007/s10494-023-00472-3.

ROCHETTE, B.; RIBER, E.; CUENOT, B.; VERMOREL, O. A generic and self-adapting method for flame detection and thickening in the thickened flame model. **Combustion and Flame**, v. 212, p. 448–458, 2020. DOI: 10.1016/j.combustflame.2019.11.015.

ROZEMA, W.; BAE, H. J.; VERSTAPPEN, R. W. C. P. Local dynamic gradient Smagorinsky model for large-eddy simulation. **Physical Review Fluids**, v. 7, n. 7, p. 074604, 2022. DOI: 10.1103/PhysRevFluids.7.074604.

SAGAUT, P. **Large Eddy Simulation for Incompressible Flows: An Introduction**. 3rd. Berlin: Springer-Verlag, 2006. ISBN 978-3540263449.

SANTOS, J. G. d. F. **Mathematical and computational modeling of gas-solid flows in dynamic adaptive mesh**. 2019. Master's Dissertation – Universidade Federal de Uberlândia, Uberlândia, Brazil.

SCHMITT, F. G. About Boussinesq's turbulent viscosity hypothesis: historical remarks and a direct evaluation of its validity. **Comptes Rendus Mécanique**, v. 335, n. 9–10, p. 617–627, 2007. DOI: 10.1016/j.crme.2007.08.004.

SEHOLE, H. A. H. Implementation of the Dynamically Thickened Flame LES Model for Premixed and Non-Premixed Turbulent Combustion in OpenFOAM. In: NILSSON, H. (Ed.). **Proceedings of CFD with OpenSource Software**. [S.l.: s.n.], 2024. Course at Chalmers University of Technology.

SILVEIRA-NETO, A. **Escoamentos turbulentos: análise física e modelagem teórica**. Uberlândia: Composer, 2020.

SMAGORINSKY, J. General circulation experiments with the primitive equations: I. The basic experiment. **Monthly Weather Review**, v. 91, n. 3, p. 99–164, 1963. DOI: 10.1175/1520-0493(1963)091<0099:GCEWTP>2.3.CO;2.

SMITH, G. P. et al. **GRI-Mech 3.0**. [S.l.: s.n.], 1999. http://www.me.berkeley.edu/gri_mech/.

SOUZA, P. R. C. et al. Multi-phase fluid-structure interaction using adaptive mesh refinement and immersed boundary method. **Journal of the Brazilian Society of Mechanical Sciences and Engineering**, 2022. DOI: 10.1007/s40430-022-03417-x.

STIVAL, L. J. et al. Wake modeling and simulation of an experimental wind turbine using large eddy simulation coupled with immersed boundary method alongside a dynamic adaptive mesh refinement. **Energy Conversion and Management**, v. 268, p. 115938, 2022. DOI: 10.1016/j.enconman.2022.115938.

STRANG, G. On the construction and comparison of difference schemes. **SIAM Journal on Numerical Analysis**, v. 5, n. 3, p. 506–517, 1968. DOI: 10.1137/0705041.

TENNEKES, H.; LUMLEY, J. L. **A First Course in Turbulence**. Cambridge, MA: MIT Press, 1972. ISBN 978-0262200196.

TROE, J. Fall-off curves of unimolecular reactions. **Berichte der Bunsengesellschaft für physikalische Chemie**, v. 78, n. 5, p. 478–488, 1974. DOI: 10.1002/bbpc.19740780514.

TURNS, S. R. **An Introduction to Combustion: Concepts and Applications**. 3rd. New York: McGraw-Hill Education, 2012. ISBN 978-0073380193.

VAN DRIEST, E. R. On turbulent flow near a wall. **Journal of the Aeronautical Sciences**, v. 23, n. 11, p. 1007–1011, 1956. DOI: 10.2514/8.3713.

VASCONCELLOS, L. G. S. **Advanced Computational Fluid Dynamics in Bloodstain Pattern Analysis: Investigating Non-Newtonian Properties for Forensic Applications**. 2024. Master's Dissertation – Federal University of Uberlândia, Uberlândia, MG, Brazil.

VEDOVOTO, J. M. **Mathematical and numerical modeling of turbulent reactive flows using a hybrid LES/PDF methodology**. 2011. Ph.D. Thesis – Federal University of Uberlândia and ENSMA, Uberlândia, Brazil and Poitiers, France. Joint doctorate between UFU and ENSMA (France).

VEDOVOTO, J. M. et al. Simulation of turbulent reactive flows using a hybrid LES/PDF methodology – Advances in particle density control for normalized variables. In: 55TH AIAA Aerospace Sciences Meeting. Grapevine, Texas: [s.n.], 2017. aiaa 2017–1473. DOI: 10.2514/6.2017-1473.

VEYNANTE, D.; MOUREAU, V. Comparison of turbulent flame speed estimation methods in a swirl-stabilized jet flame. **Combustion and Flame**, v. 162, n. 12, p. 4622–4642, 2015. DOI: 10.1016/j.combustflame.2015.09.023.

VEYNANTE, D.; VERVISCH, L. Turbulent combustion modeling. **Progress in Energy and Combustion Science**, v. 28, n. 3, p. 193–266, 2002. DOI: 10.1016/S0360-1285(01)00017-X.

VILLAR, M. M. **Análise numérica da interação fluido-estrutura pelo método da fronteira imersa**. 2007. Ph.D. Thesis – Universidade Federal de Uberlândia, Uberlândia, Brazil.

VISWANATHAN, S.; PATEL, H. V. Assessment of subgrid-scale models for large-eddy simulation of a planar turbulent wall-jet with heat transfer. **International Journal of Heat and Mass Transfer**, v. 148, p. 119146, 2020. DOI: 10.1016/j.ijheatmasstransfer.2019.119146.

VOLPIANI, P. S.; SCHMITT, T.; VEYNANTE, D. A posteriori tests of a dynamic thickened flame model for large eddy simulations of turbulent premixed combustion. **Combustion and Flame**, v. 174, p. 166–178, 2016. DOI: 10.1016/j.combustflame.2016.08.007.

WANG, G.; BOILEAU, M.; VEYNANTE, D. Implementation of a dynamic thickened flame model for large eddy simulations of turbulent premixed combustion. **Combustion and Flame**, v. 158, n. 11, p. 2199–2213, 2011. DOI: 10.1016/j.combustflame.2011.04.008.

WILCOX, D. C. **Turbulence Modeling for CFD**. 2nd. La Cañada, CA: DCW Industries, 1998. ISBN 978-0963605153.

WILKE, C. R. A Viscosity Equation for Gas Mixtures. **The Journal of Chemical Physics**, v. 18, n. 4, p. 517–519, 1950. DOI: 10.1063/1.1747673.

WILLIAMS, F. A. **Combustion Theory**. 2nd. Menlo Park, CA: Benjamin/Cummings Publishing Company, 1985. ISBN 978-0201407778.

XIA, Y.; HUANG, C.; ZHAO, D.; LUO, K. H. Evaluation of Thickened Flame Model Sub-Grid Efficiency Functions. **ASME Journal of Engineering for Gas Turbines and Power**, 2023. DOI: 10.1115/GT2023-100832.

YAMASHITA, H.; SHIMADA, M.; TAKENO, T. A numerical study on flame stability at the transition point of jet diffusion flames. **Symposium (International) on Combustion**, v. 26, n. 1, p. 27–34, 1996. DOI: 10.1016/S0082-0784(96)80196-2.

YANG, B.; POPE, S. B. An investigation of the accuracy of manifold methods and splitting schemes in the computational implementation of combustion chemistry. **Combustion and Flame**, v. 112, n. 1–2, p. 16–32, 1998. DOI: 10.1016/S0010-2180(97)81754-3.

ZHANG, H. et al. Large eddy simulation of turbulent premixed swirling flames using dynamic thickened flame with tabulated detailed chemistry. **Flow, Turbulence and Combustion**, v. 98, n. 3, p. 841–885, 2017. DOI: 10.1007/s10494-016-9791-9.

ZHANG, P.; PARK, J. W.; WU, B.; IHME, M. Large eddy simulation/thickened flame model simulations of a lean partially premixed gas turbine model combustor. **Combustion Theory and Modelling**, v. 25, n. 7, p. 1296–1323, 2021. DOI: 10.1080/13647830.2021.1979676.

ZHANG, X.; HUANG, Q.; MA, Y. A dynamic Smagorinsky model for horizontal turbulence parameterization in tropical cyclone simulation. **Geophysical Research Letters**, v. 51, n. 19, e2024gl110392, 2024. DOI: 10.1029/2024GL110392.

First Appendix

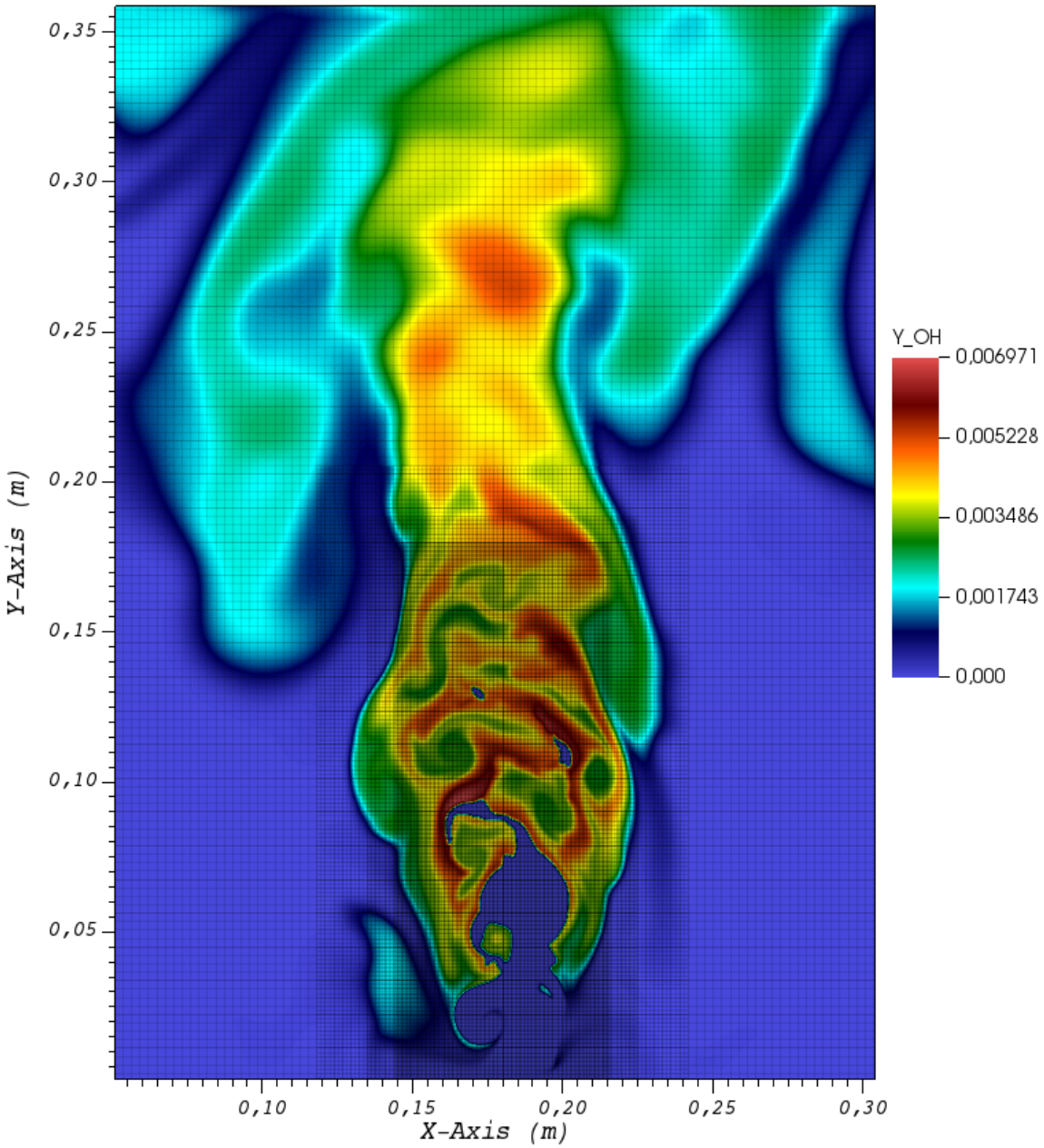

Figure A.1: Instantaneous hydroxyl radical (OH) mass fraction field for Case 1.

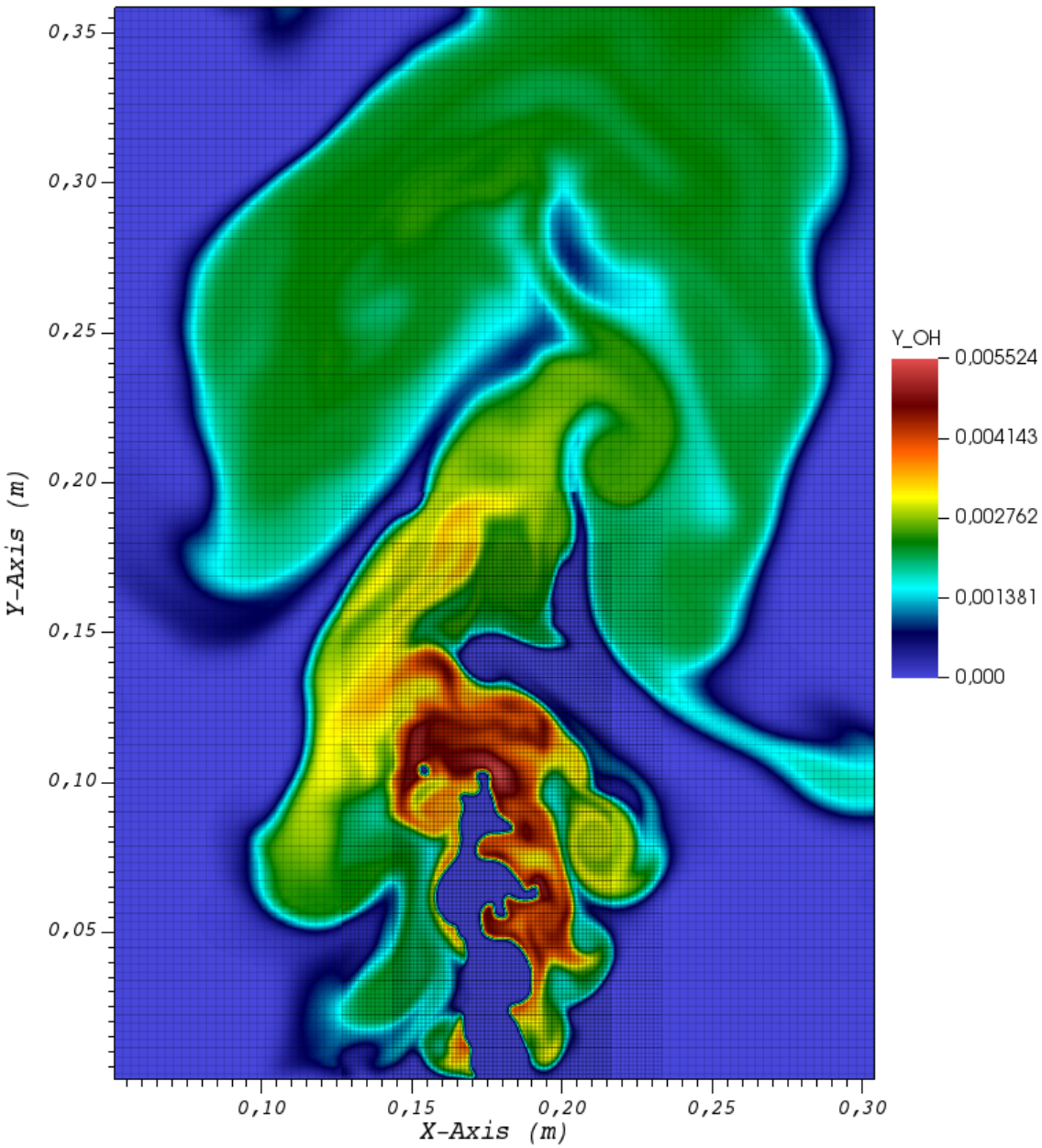

Figure A.2: Instantaneous hydroxyl radical (OH) mass fraction field for Case 2.

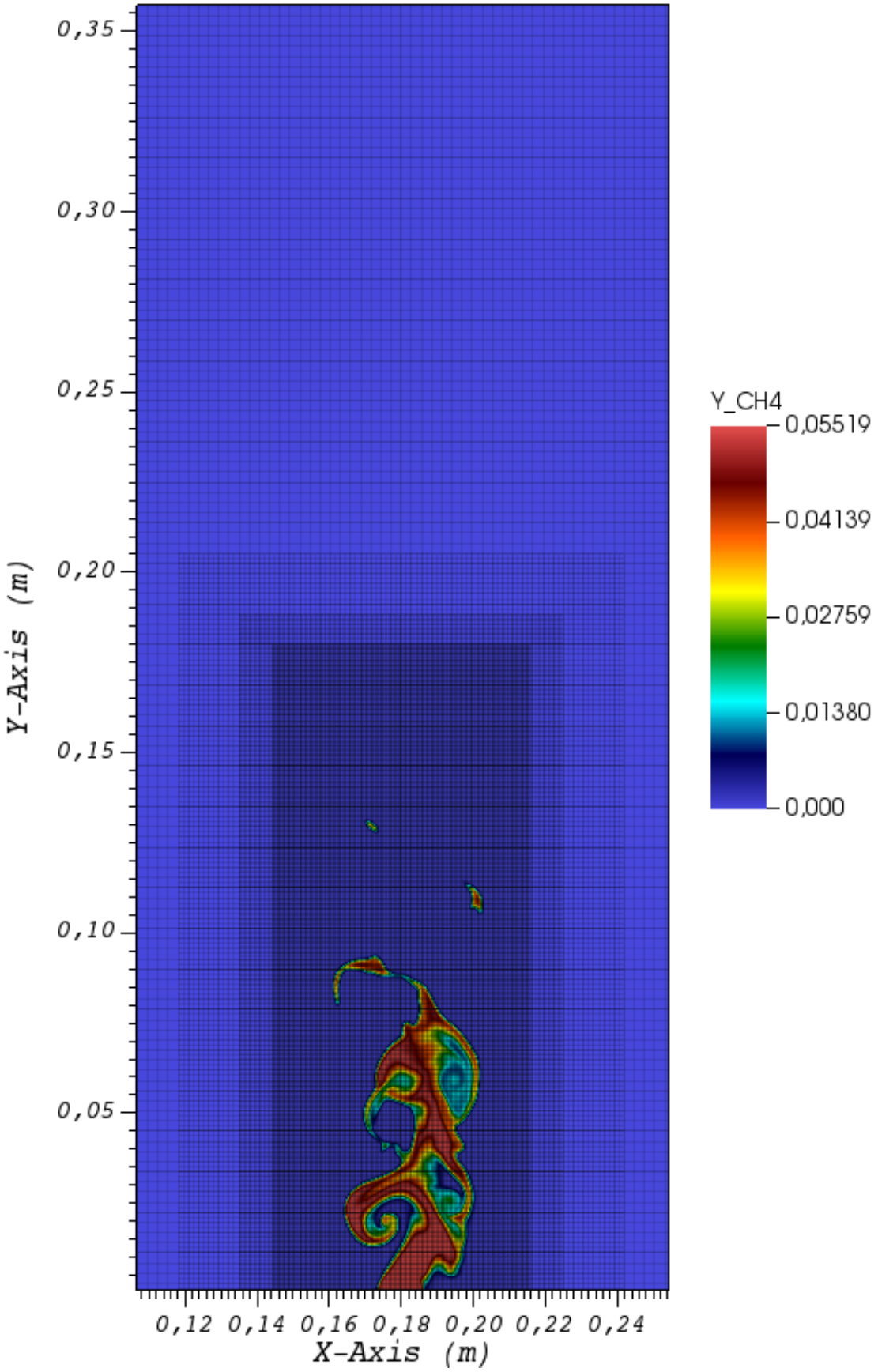

Figure A.3: Instantaneous methane (CH_4) mass fraction field for Case 1.

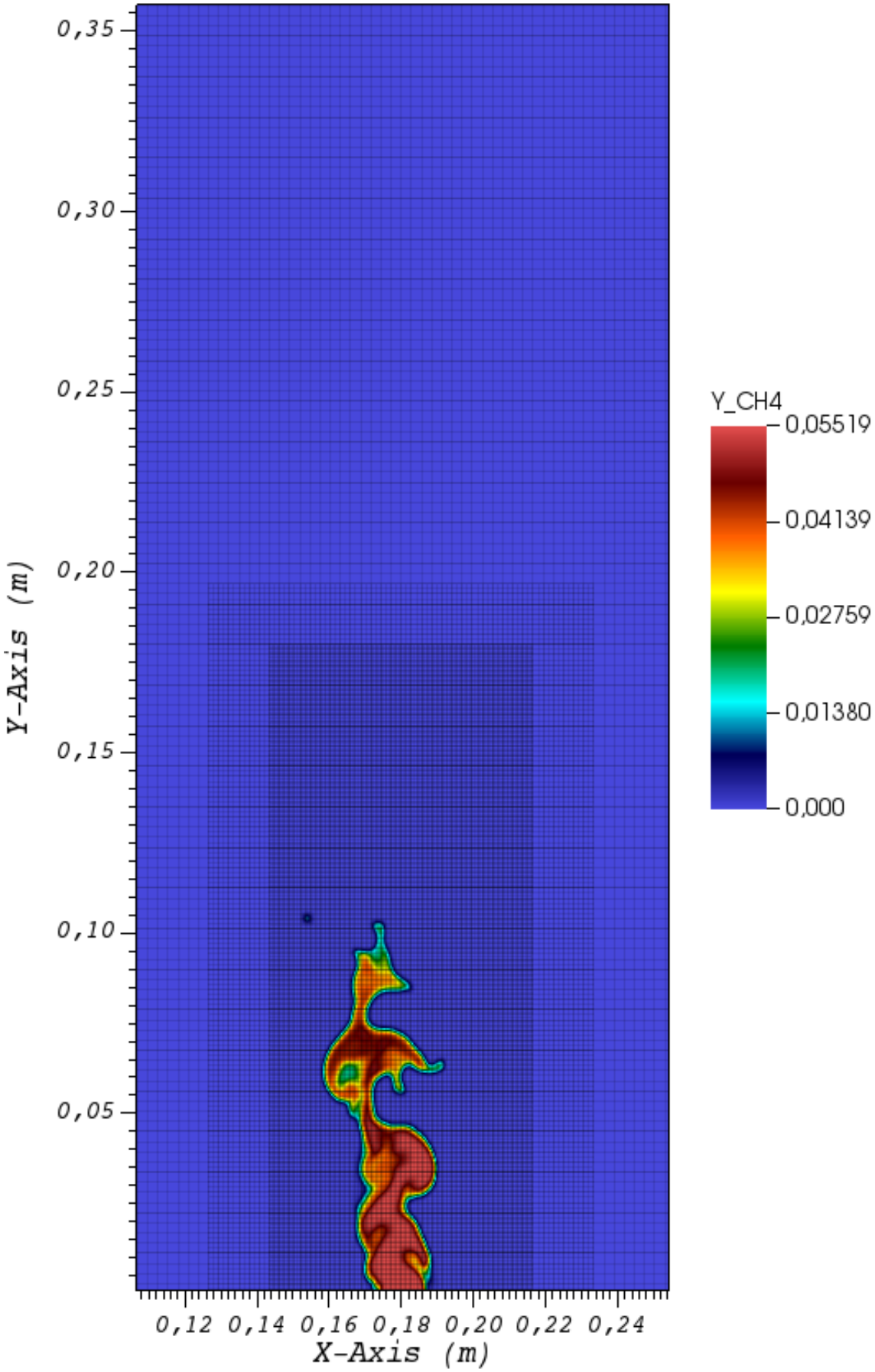

Figure A.4: Instantaneous methane (CH_4) mass fraction field for Case 2.